August 2014

Molecular Dynamics (MD) Study on the Electrochemical Properties of Electrolytes in Lithium-Ion Battery (LIB) Applications

Negin Salami
University of Wisconsin-Milwaukee

MOLECULAR DYNAMICS (MD) STUDY ON THE ELECTROCHEMICAL PROPERTIES OF ELECTROLYTES IN LITHIUM-ION BATTERY (LIB) APPLICATIONS

by

Negin Salami

A Thesis Submitted in

Partial Fulfillment of the

Requirements for the Degree of

Master of Science

in Engineering

at

The University of Wisconsin-Milwaukee

August 2014

ABSTRACT

MOLECULAR DYNAMICS (MD) STUDY ON THE ELECTROCHEMICAL PROPERTIES OF ELECTROLYTES IN LITHIUM-ION BATTERY (LIB) APPLICATIONS

by

Negin Salami

The University of Wisconsin-Milwaukee, 2014
Under the Supervision of Professor Chang-Soo Kim

While the high energy density and the power along with longer cycle life and less requirements of maintenance distinguish the rechargeable lithium-ion batteries (LIBs) from other energy storage devices, development of an electrolyte of LIBs with optimized properties still constitutes a challenge towards next-generation LIB systems with robust electrochemical performance. The electrolytes serve as the medium to provide ionic conduction path between the electrodes as their basic function. Conductivity of the solutions are mainly affected by their transport properties and the electrolyte-electrode/separator interfacial phenomena. Although many contributions on thermodynamic properties of the electrolytes consist of alkyl carbonates mixed with salts have been previously studied, relatively little information is known regarding the correlation between interfacial properties of the electrolyte-electrode/separator with electrochemical properties of the cell. In this study, therefore, we present the impacts of salt concentration and temperature-dependent properties of LIBs on wetting behavior of various electrolytes, i.e., ethyl methyl carbonate (EMC), diethyl carbonate (DEC), and propylene carbonate (PC), in contact with the graphite anode and polyethylene

(PE)/polypropylene (PP) separator using molecular dynamics (MD) computational technique. The results based on MD computations affirm the general consistent dependency of interfacial tension energies to polarity of the solvents in DEC, EMC, and PC electrolytes contained 1 M $LiPF_6$ salt. The PC systems interestingly showed inverse trend due to the special stacking motifs of PC layers that may increase the interfacial electrostatic interactions. Temperature did not show significant effect on the interfacial energies of linear solvents whereas PC exhibited more tendency to interact with the graphite anode at T = 25 °C compared to the similar solution at 0 °C. Moreover, the electrolytes that incorporated same solvents had better wettability in absence of salt ions due to their lower polarity and viscosity. Accordingly, EMC: 0.752 M $LiPF_6$ electrolyte system had the lowest interfacial energy value among the EMC solutions contained 1 M and 1.254 M salt. However, the probability of insufficient number of charge carriers in addition to the close values of interfacial energies for electrolytes with 0.752 M and 1 M $LiPF_6$ resulted in considering EMC: 1 M $LiPF_6$ electrolyte as a more efficient mixture. The impact of solution polarity on clustering behavior of the salt ions were investigated in DEC, EMC, and PC electrolytes with 1 M $LiPF_6$ based on the ions coordination and their relative closest neighbors. Due to the higher dielectric constant value, PC showed higher ability of salt dissociating, which leaded that Li^+ and PF_6^- ions were distributed more uniformly compared to the DEC and EMC electrolytes.

To my family for their love and support

TABLE OF CONTENTS

LIST OF FIGURES

LIST OF TABLES

LIST OF ABBREVIATIONS

LIB_ Lithium ion battery

MD_ Molecular Dynamics

DEC_ Diethyl carbonate

EMC_ Ethyl methyl carbonate

PC_ Propylene carbonate

$LiPF_6$_ Lithium hexafluorophosphate

LUMO_ Lowest unoccupied molecular orbital

HOMO_ Highest occupied molecular orbital

EC_ Ethylene carbonate

SEI_ Solid electrolyte interphase

PE_ Polyethylene

PP_ Polypropylene

IC_ Initial condition

BC_ Boundary condition

IBC_ Isolated boundary condition

PBC_ Periodic boundary condition

ACKNOWLEDGEMENTS

I would like to express my sincere gratitude to my advisor Dr. Changsoo Kim for the illuminating advice, patient guidance, and encouragement he has provided to support me develop this project.

Furthermore, I am particularly grateful for the comments and advice given by my committee members Dr. Church and Dr. Chang.

Lastly, I would like to thank my family and dearest friends for their great support.

1. Introduction

In the first chapter, we introduce lithium ion batteries (LIB) and focus on the undisputed roles of electrolytes in monitoring the power and the cycle ability of these energy storage devices. Accordingly, the factors influence the electrochemical properties of carbonate-based electrolytes will be briefly explained where the deficiencies of previous studies in depicting a lucid relationship between the fundamental electrochemical properties and interface phenomena of electrolytes are introduced as the motivations of this study. To establish a theoretical understanding, we introduce an atomistic computational model developed by employing the molecular dynamics (MD) technique to predict the estimation of electrolyte-anode/separator interfacial energies.

1.1. Lithium-ion batteries and the electrolytes

Lithium-ion batteries (LIBs) are the remarkable energy storage devices widely used in small grid storage systems, telecommunication apparatuses, and hybrid-electric automotive industries. Sony Corporation introduced LIB cells in the early 1990s as the batteries which are indebted their high energy density to lithium as the most electronegative as well as the lightest metal while do not have the dendrite- based safety problems of lithium primary cells [1,2]. Electrodes, separator, and electrolyte are the main components

of LIB where the electrolyte plays an indispensable role in governing the performance of these devices. The key to construct a safe and high-performance LIB lies in identification of a suitable electrolyte. The electrolyte establishes high ionic conductivity between the two electrodes. Moreover, the coordination between the electrolyte electrochemical window and the electrodes electrochemical potentials provides the thermodynamic stability of the cell. Additionally, employing non-flammable and non-explosive components with higher ignition points or flash points ensure the safety of LIB cells.

The four common types of electrolytes that are employed in LIBs are solid polymer electrolytes, gel electrolytes, ionic liquids, and organic liquid electrolytes. Organic electrolytes are the most prevalent electrolytes employed for these cells due to their higher ionic conductivities and practical operating temperature range. These systems consist of a mixture of different alkyl carbonates with a lithium salt. In this study, propylene carbonate (PC) is considered as the cyclic carbonate solvent where its high polarity results in relatively high viscosity due to its strong intermolecular interactions. Also, the linear carbonates employed are ethyl methyl carbonate (EMC) and diethyl carbonate (DEC) which have relatively lower viscosity and permittivity due to the considerable dynamic degree of freedom provided by their linear molecular structures. Additionally, lithium hexafluorophosphate ($LiPF_6$) is the lithium salt which has been industrialized successfully since it has a high ionic conductivity and a wide electrochemical stability window.

1.2. Motivations of research

Since electrolytes serve as the medium to provide ionic conduction path between the electrodes as their basic function, optimizing the transport and wetting properties as the

factors that influence the electrochemical properties of electrolytes is the prime concern to achieve an efficient balance among cycle ability, capacity, power, and fast charging of the cell. Solvent type, salt concentration, and temperature are the three fundamental keys that affect the electrochemical behavior of the solutions. Viscosity of an electrolyte inversely changes with temperature while there is a consistent relationship between salt concentration and viscosity of the solution. Temperature and salt concentration variables may affect interfacial tension and wetting properties with respect to the viscosity and dielectric constant of the solvents. Moreover, there is an undisputed relationship between salt concentration and dielectric constant of the solvents as their ability to dissociate salt ions. Thus, this solvent property directly impacts ion conductivity and subsequently, electrolyte-electrode/separator wettability by the same procedure that mobility and diffusivity of ions act. Although many contributions on thermodynamic properties of alkyl carbonates mixed with salts have been described in the literature, little information has been provided regarding the correlation between interfacial properties of electrolyte-anode/separator with electrochemical and transport properties of the cell. Therefore, we will focus on the fundamental electrochemical properties and the interfacial phenomena of electrolytes including interfacial energies, wettability, and interactions of electrolytes with anode/separator to establish a theoretical understanding.

1.3. Objectives of research

In the current thesis, we aim to understand the electrochemical effects of the cyclic and linear carbonate solvents that are commonly applied to the LIB cell and subsequently, their impacts on the conductivity and the wettability of LIB applications by studying the interfacial phenomena of one-component electrolytes incorporate various salt

concentrations at different temperatures. Toward this goal, we developed an atomistic computational model using the molecular dynamics (MD) technique to predict the interface energies, wettability, and interface phenomena from various carbonate-based electrolyte systems including the effects of temperature and salt concentration. As will be introduced in Chapter 3, there have been some previous MD techniques to quantify the interfacial energies of liquid on solid substrates. In this work, we combined the previous efforts to develop a more rigorous MD methodology to predict the interfacial energies of solvent materials and solid electrodes/separators. Although multi-component solvent systems are routinely used in commercialized products, one-component solvent systems were focused on in this study. Both mechanical and thermodynamic definitions of interfacial energy were considered in developing our model where this procedure can be regarded as one of the first attempts to our knowledge.

2. Background

In this chapter, we will provide the comprehensive background on the structure and cell reactions of lithium ion batteries (LIBs) with respect to the four main components as cathode, anode, electrolyte, and separator. The main focus will be on the electrochemical properties of non-aqueous electrolytes, and the relationships between the transport properties and interfacial phenomena will be explained in detail. Moreover, we address the factors that affect the electrolyte-electrode/separator wettability and the role of interfacial tension energy.

2.1. Structure of lithium-ion secondary batteries

During past centuries, fossil fuels were the primary energy sources to promote the technology for human life. However, non-renewable resource waste and global climate change caused the urgency of employing batteries as the economically and environmentally friendly energy conversion and storage devices using controlled electrochemical reactions to provide energy efficiently. Among all the diverse types of the current technologies, lithium-based batteries are the most favorable energy storage devices since they are indebted their high energy density to Lithium as the most electronegative as well as the lightest metal. Comparison of the different battery technologies in terms of volumetric and gravimetric energy density values is shown in Fig. 2.1 where the category of lithium batteries possesses the highest energy density beside their smaller size and lighter weight.

Nevertheless, using lithium metal directly as a negative electrode generates unsolvable lithium dendrite problem which makes Li batteries unpractical. The advent of lithium-ion secondary batteries in the early 1990s ensured the safety of Li-based batteries established on the principle of reversible transfer of Li^+ by intercalating between the electrodes through the electrolyte solution. Exploiting "intercalation" or "insertion"-type electrodes such as carbonaceous anodes makes lithium to exist in its ionic rather than metallic state which results in eliminating any possibility of dendrite lithium. Increasing demands for the performance necessary to support the sophisticated functions of modern equipment in addition to reduced size and weight for mobile applications have led to introduce Li-ion rechargeable batteries to the present information-rich society as the most popular power source which offer excellent low-temperature performance, load characteristics, and cycle life [3-8].The performance of LIBs directly depends on the charge-discharge processes and the type of materials used for the cell components shown in Fig. 2.2.

Reversible redox reactions maintain charge and discharge cycles as foundation of lithium ion rechargeable batteries. Discharge process is considered as a spontaneous electrochemical reaction due to the presence of electromotive forces. As the first step, the oxidation ($Li \rightarrow Li^+ + e^-$) of the electrode proceeds at the negative terminal which is termed as anode.

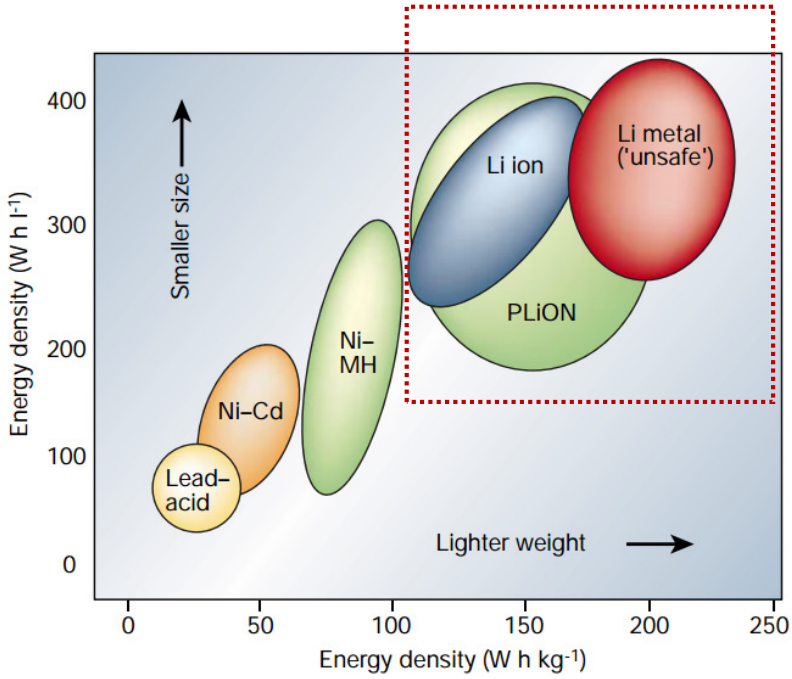

Fig. 2.1 Volumetric and gravimetric energy density for different types of batteries [3].

At the second step, the electrons conducted by anode to the electron collector Cu flow from the anode to the cathode through the external wire connecting the two electrodes, thus forming a closed circuit. The generated ions are shuttled from the anode to the cathode via electrolyte as an ionic conductor. Electrons transferred from the negative terminal through the external circuit engage in reduction ($Li^+ + e^- \rightarrow Li$) at the positive terminal, which is known as a cathode. During charging, an external electrical power source (the charging circuit) applies an over-voltage (a higher voltage but of the same polarity) than that produced by the battery, forcing the current to pass in the reverse direction. The lithium ions then migrate from the positive to the negative electrode, where they become embedded in the porous electrode material in a process known as intercalation [9-11]. In other words, non-spontaneous oxidation and reduction reactions occur in the cathode and the anode, respectively, during the charging process and spontaneous reactions of discharging take

place in the anode and the cathode. During non-spontaneous charge an external electrical power is applied to the device to oxidize the cathode materials. Thus lithium ions are deintercalated from the cathode and transported along with generated electrons through the electrolyte and external circuit, respectively. These electrons engage in reduction reactions with anode materials non-spontaneously and the lithium ions intercalate in them.

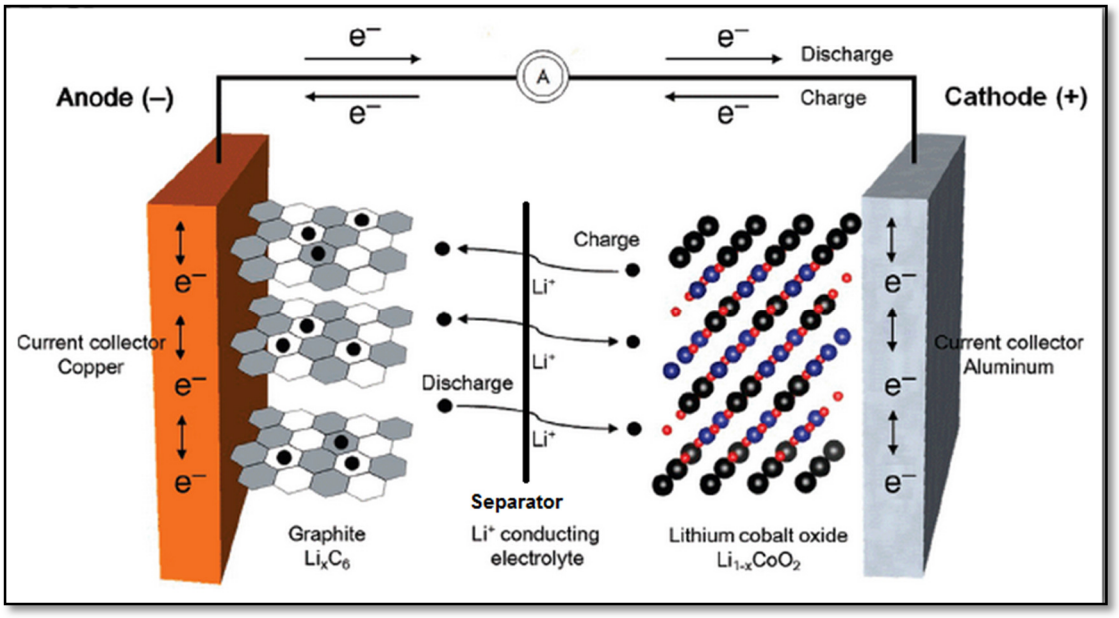

Fig. 2.2 Charge-Discharge mechanisms. Movement of Li^+ in an electrolyte and insertion/extraction of Li^+ with in electrodes in LIBs [11].

Simultaneously spontaneous reactions occur in the anode as the primary step of discharge and the generated lithium ions and electrons are transported through the electrolyte and the external circuit to complete the discharging process in the cathode by engaging in spontaneous reduction reactions. At the anode the lithium ions are stored and released during charge and discharge, respectively. Reversible redox reactions create concept of rechargeable batteries in which the redox reactions can be repeated within the

same electrode. Accordingly an electrode plays the both anode and cathode roles during charge and discharge, respectively.

There are three main components participate in electrochemical reactions to maintain charge-discharge mechanisms in the Li-ion battery cell: the cathode (positive electrode, the anode (negative electrode), and the electrolyte. The electrochemical reactions for charge and discharge processes are shown as below. Since lithium transition metal oxides are considered as the source of supplying lithium ions, lithium cobalt oxide ($LiCoO_2$) takes place as the cathode material which has superior cycling properties at high voltages. Additionally, graphite has been introduced as a promising material for anode applications.

Positive Electrode $LiCoO_2 \underset{\text{Discharge}}{\overset{\text{Charge}}{\rightleftharpoons}} Li_{1-x}\ CoO_2 + xLi^+ + xe^-$ (2-1)

Negative Electrode $xC_6 + xLi^+ + xe^- \rightleftharpoons xLiC_6$ (2-2)

Battery as a whole $LiCoO_2 + xC_6 \rightleftharpoons Li_{1-x}CoO_2 + xLiC_6$ (2-3)

2.2. Materials for lithium-ion secondary batteries

The LIB cell is constructed from the cathode, the anode, the electrolyte solution, and the separator as the main components. The descriptions for the roles and the appropriate materials used in these components of LIBs are provided by the following sections.

2.2.1. Cathode Materials

2.2.1.1. Demand characteristics of Cathode Materials – Roles

Since cathode is the main source of providing lithium ions in LIBs, it should meet certain characteristics and roles to fulfill its vital mission [12,13]:

1) Being light and densely packed is necessary for the cathode materials to allow high volumetric and gravimetric energy density for the cell.

2) Cathode materials should have high electrical and ionic conductivities to generate high power.

3) There should be a narrow grain size distribution for the particles of cathode materials to improve the particle contacts and electrical conductivity.

4) The structure of cathode materials plays an important role to maintain high cycle efficiency for the cell by eliminating the side reactions unrelated to lithium ion circulation at the cathode or anode.

5) The charge-discharge process imposes the irreversible phase transitions of crystal structure in cathode materials. This phenomenon has detrimental effects on the battery capacity life and should be prevented.

6) Displaying reversible behavior and a flat potential is mandatory for the cathode materials with the intercalation-deintercalation of large amount of lithium ions to enhance energy efficiency during charge-discharge.

7) Cathode materials should have electrochemical and thermal stability to prevent reactions with the electrolyte.

To summarize the properties of cathode materials, there are following criterions that should be considered: energy density, cycling performance, rate capability, safety, and

cost. Energy density is affected by the material's reversible capacity and operating voltage determined by the material intrinsic chemistry such as the effective redox couples and maximum lithium concentration in active materials. Electronic and ionic mobility are the main factors to determine cycling performance and rate capability. Additionally, since the crystal structures may have anisotropic nature, particle morphologies are important in some cases. As the result, two main important aspects must be considered for the cathode materials: material intrinsic chemistry and morphology [14].

2.2.1.2. Structure and Electrochemical Properties of Cathode Materials

The cathode materials used for lithium-ion batteries can be categorized into three groups according to their structures where we briefly introduce the first group as the most common cathode in following:

a) Layered compounds $LiMO_2$ (M = Co, Ni, Mn, etc.)

b) Spinel compounds LiM_2O_4 (M = Mn, etc.)

c) Olivine compounds $LiMPO_4$ (M = Fe, Mn, Ni, Co, etc.)

A close-packed face-centered cubic (FCC) lattice of an ideal layered compound $LiMO_2$ is shown in Fig. 2.3. The crystal structure is formed from the MO_2 slabs with oxygen anions and the cations located in the 6-coordinated octahedral crystal sites and the lithium layers placed alternatively. $LiCoO_2$ is the first layered compound considered as a cathode material in 1980 which is the origin of catching major research interests towards the transition metal intercalation oxides [15,16].

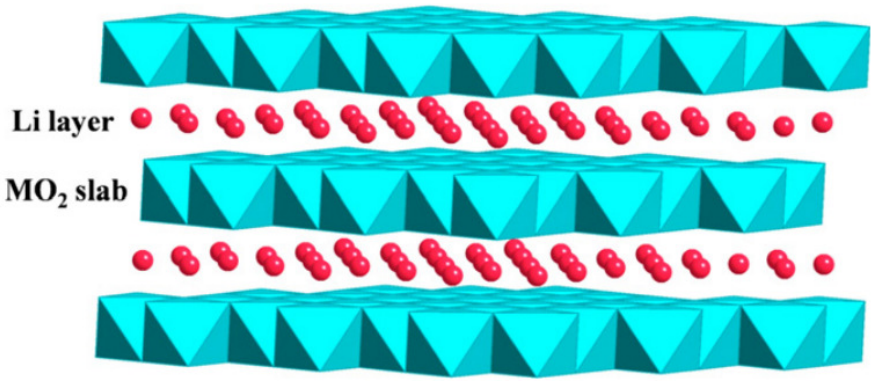

Fig. 2.3 Crystal structure of an ideal layered compound $LiMO_2$ [14].

Although the conventional layered oxide $LiCoO_2$ has been commercialized as the LIB cathode for a significant period, it can only deliver about 140 mAh/g capacity which is half of its theoretical capacity. This limitation results in intrinsic structural instability of the material when more than half of the lithium ions are extracted. Furthermore, toxicity and high costs needed for supplying Co ions in $LiCoO_2$ have made LIBs not affordable as well as caused environmental pollutions. These problems have led to substitute cobalt ions partially or fully by other transition metal ions such as Ni and Mn which are less expensive and more environmental friendly by mixing the $LiNiO_2$ and $LiMnO_2$ with different ratios, forming various compositions of layered $LiCo_xNi_yMn_{1-x-y}O_2$, and the formation of Li–Co–Ni–Mn–O layered compound (NMC type materials) if Co ions partially have been substituted [17]. Since the Li–Ni disorder is the main factor affecting the material rate capability, good electrochemical performance of $LiCo_{1/3}Ni_{1/3}Mn_{1/3}O_2$ was reported by Ohzuku et al. [18]. Additionally, the importance of the series of Li–Co–Ni–Mn–O material is distinguished due to the significant effect of cobalt ions in decreasing the amount of Ni in lithium layer.

Table 2.1 provides an overview of the properties of different cathode materials belonged to the all three categories [12].

Table 2.1 Battery cell characteristics with various cathode materials. [a] Commercially available capacity.

Cathodes	Theoretical capacity (mAh/g)	Practical capacity[a] (mAh/g)	Avg. potential (V versus Li/Li^+)	True density (g/cc)
$LiCoO_2$	274	~150	3.9	5.1
$LiNiO_2$	275	215	3.7	4.7
$LiNi_{1-x}Co_xO_2$ $(0.2 \leq x \leq 0.5)$	~280	~180	3.8	4.8
$LiNi_{1/3}Mn_{1/3}Co_{1/3}O_2$	278	~154	3.7	4.8
$LiNi_{0.5}Mn_{0.5}O_2$	280	130-140	3.8	4.6
$LiMn_2O_4$	148	~130	4.0	4.2
$LiMn_{2-x}M_xO_4$	148	~100	4.0	4.2
$LiFePO_4$	170	~160	3.4	3.6

2.2.2. Anode Materials

2.2.2.1. Required Conditions for Anode Materials

As the performance of LIB including power density, energy density, and cycle life is drastically influenced by anode materials, they should meet the following certain characteristics to maximize the battery performance [19]:

1) Active anode materials should provide fast diffusivity of lithium ion as this is one of the major factors to determine the cell performance.

2) Critical changes in crystal structure of anode material should be prohibited during electrochemical reactions by intercalation-deintercalation of Li ions. Otherwise, the cumulative crystal strain prevents the reversibility of reactions which leads to poor cycling life characteristics.

3) Required low potential of anode materials should be in compliance with a standard electrode and supply a high cell voltage with the cathode. The potential relating to the electrochemical reactions must be a close approximation of the electrochemical potential of the anode material.

4) Ease of electron movements during electrochemical reactions will be assured by high electronic conductivity of anode materials.

5) Capability of storing a significant amount of charge (coulomb) per unit mass is necessary. Accordingly, designing an appropriate anode material is critical since it has a larger specific capacity per unit mass in comparison with the cathode which impedes the fast intercalation-deintercalation of lithium ions and directly affects the battery performance.

6) Enhancing battery energy entails designating sufficiently dense active anode materials to obtain a high electrode density. Table 2.3 shows the main characteristics of common anode materials.

7) Energy density and power of lithium ion battery is also determined by the tapped density (which refers to the bulk density of the powder after a specified compaction process, usually involving vibration of the container), specific surface area, distribution, and particle size of anode material.

2.2.2.2. Types and Electrochemical Properties of Anode Materials

The main anode materials designated for lithium ion secondary batteries can be categorized as following:

- Li-Based Materials
- Carbon-Based Materials
- Lithium Alloys
- Silicon

Since graphitic anode has been employed in this study, we briefly introduce carbon-based anode materials. Carbon is the undisputed candidate of anode material due to its cost, availability, higher specific charges, and more negative redox potentials compared with most metal oxides and polymers, and also better cycling performance than lithium alloys. However, its extensive applications are restricted according to the limitation of the theoretical gravimetric capacities of carbon-based materials (372 Ah kg^{-1}, LiC_6), malfunction under high charge/discharge rates as lithium can deposit on the surface of graphite, and cointercalation of Li ions and electrolyte solvents into the graphene layers [20,21].

The carbonaceous materials employed in LIBs are classified into graphite and non-graphite classes depending on their structural discrepancies. Graphite usually has a hexagonal structure arranged in ABAB stacking along the c-axis and also takes the form of a rhombohedral structure in ABCABC. It consists of graphene layers which are conductive with carbon atoms of the sp^{-2} hybrid orbital layer along a hexagonal plane. Additionally, the delocalized mobile π electrons that have Van der Waals bondings between graphene layers result in good electronic conductivity of the graphite. Li ions are intercalated and deintercalated between these graphene layers. The graphite crystal is

anisotropic due to the parallel edge plane and perpendicular basal plane with respect to the c-axis which affects the electrochemical reactions at the negative electrode of lithium ion batteries. Electrochemical characteristics are determined by the ratio of the edge plane and basal plane as highly active and non-active sites, respectively.

As the other type of carbon-based materials, non-graphitic carbon comprises small hexagonal networks and displays a disorderly structure that is purely developed in the c-axis. Amorphous phases exist together with crystallites which establish cross linking.

Carbon materials can be categorized into graphitizable and non-graphitizable carbon depending on their graphitizability according to the capability of crystallites rearrangement during the carbonization process of carbon precursors. Fig. 2.4 illustrates the structure of graphitizable and non-graphitizable carbon. In graphitizable or soft carbons, the graphene layers arranged in a parallel manner facilitate graphitization at high temperatures. On the other side, the carbonization process suppresses the stacking of graphene layers in non-graphitizable or hard carbons which results in cross linking between crystallites. The small crystallites and a disordered structure impede rearrangement of the crystals for graphitization even at high temperatures above 2500 °C.

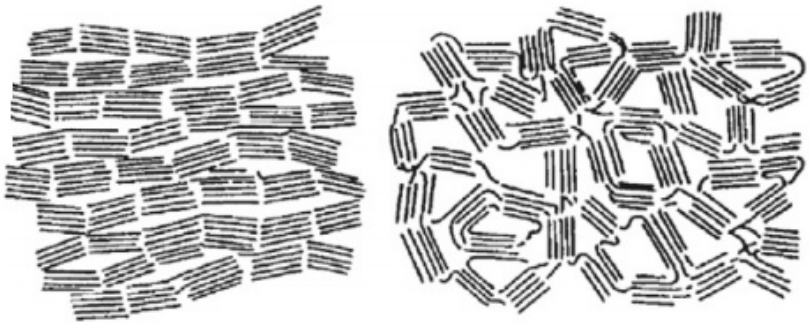

Fig. 2.4 Franklin's model for left: graphitizable and right: non-graphitizable carbon [22].

Table 2.2 provides an overview of the properties of some commonly used anode materials [11].

Table 2.2 Characteristics of common anode materials. [a]Commercially available capacity.

Anodes	Theoretical capacity (mAh/g)	Practical capacity[a] (mAh/g)	Avg. potential (V versus Li/Li^+)	True density (g/cc)
Li metal	3860	_	0.0	0.535
Graphite	372	~360	~0.1	2.2
Cokes	_	~170	~0.15	<2.2
Silicon	4200	~1000	~0.16	2.36
Tin	790	~700	~0.4	7.30

2.2.3. Electrolytes

An electrolyte is the indispensable component in all electrochemical devices to serve as the medium for the movement of ions between a pair of electrodes. The electrolytes generally consist of solvents, salts, and also additives if necessary. According to a particular battery application, various kinds of material components can form different types of electrolytes. The key to construct a safe and high-performance LIB lies in the identification of a suitable electrolyte. Table 2.4 summarizes the properties of some electrolytes commonly used in LIBs.

As listed in Table 2.3, these electrolytes exhibit different characteristics depending on the nature of material types. Liquid electrolytes are comprised of lithium salt dissolved

in one or more organic solvents that have been widely used since Li primary batteries were first developed. Carbonates as the organic liquid solvents and the two inorganic solvents $LiAlCl_4$ and SO_2 are incorporated in organic and inorganic liquid electrolytes, respectively [23].

Table 2.3 Different types of electrolytes for lithium secondary batteries.

Properties	Organic Liquid electrolytes	Ionic liquid electrolytes	Solid polymer electrolytes	Gel polymer electrolytes
Composition	Organic solvents + lithium salts	RT ionic liquids + lithium salts	Polymer + lithium salts	Organic solvents + polymer + lithium salts
Ion conductivity	High	High	Low	Relatively high
Low-temp. performance	Relatively good	Poor	Poor	Relatively good
Thermal stability	Poor	good	Excellent	Relatively good

Although the inorganic solvents benefit from the non-flammability compared to the organic solvents, their electrochemical window, i.e., the voltage range where no redox reaction occurs, appears to be too small to make them competitive. Ionic liquid electrolytes contain molten salts with a melting temperature below room temperature and used along with lithium salts. These electrolytes are known to generate safer batteries due to the absence of flammable organic solvents in addition to their better thermal stability, low vapor pressure, low toxicity, high boiling points, high lithium salt solubility, and high oxidation potential (~5.3 V vs Li^+/Li^0) [24]. However, their high viscosity reduces the

lithium ion conductivity. Solid polymer electrolytes are produced by dissolving Li salts in polymers with high polarity. This type of electrolyte can also operate as the separator of the electrodes and maintain contact over an electrode/electrolyte interface during moderate changes of the electrode volume with the state of charge of the battery. Nevertheless, solid polymer electrolytes have only been applied in thin-film battery applications due to their low ionic conductivity [25]. Gel polymer electrolytes are produced based on a polymer matrix gelled by liquid electrolytes. In this type of electrolyte, the mostly organic molecules serve as the main solvents, while the lower percentage of polymer that inflated by these solvents provide the dimensional stability. These electrolytes show transitional characteristics between liquid and polymer electrolytes [26]. Since the non-aqueous organic liquid electrolytes are focused on in this study, characteristics and relevant components of this electrolyte type will be addressed in the following sections.

2.2.3.1. Requirements of Liquid Electrolytes

The liquid electrolytes used in LIBs are typically lithium salts dissolved in organic solvents. Because there are different types of liquid salts and organic solvents, the combinations should be selected consciously to satisfy the specific purpose of lithium secondary batteries applications. Consequently, the following requirements have to be met [27,28]:

1) The electrolyte should have a high ionic conductivity and also be a good electronic insulator. Accordingly, it should facilitate the movements of lithium ions between the electrodes and increase the battery performance especially in rapid charge/discharge processes. In addition, the self-discharge phenomenon can be kept as minimum as possible.

Typically, the Li^+-ion conductivity (σ_{Li}) and electronic conductivity of the electrolyte (σ_e) should be higher than 10^{-4}S/cm and lower than 10^{-10} S/cm, respectively.

2) The electrolyte should be electrochemically stable to place the potential range of electrodes redox reactions within its wide electrochemical window. Furthermore, the electrolyte has to be chemically stable toward various materials applied for the production of electrodes and battery. The energy separation of the lowest unoccupied molecular orbital (LUMO) and the highest occupied molecular orbital (HOMO) of the electrolyte is the "window" of the electrolyte. Also, the two electrodes are electronic conductors with anode and cathode electrochemical potentials (μ_A and μ_C) as the reductant and oxidant, respectively. An anode with a μ_A value above the LUMO will reduce the electrolyte and a cathode with a μ_C value below the HOMO will oxidize the electrolyte unless a passivation layer blocks electron transfer from the electrolyte to the electrodes. Thus, locating the electrode electrochemical potentials within the electrolyte window is required to provide the thermodynamic stability of the cell.

3) Liquid electrolytes are usually employed in the LIBs with mobile applications. Consequently, they should have electrochemical stability in the temperature ranging from -20 to 60 °C.

4) Non-flammable and non-explosive components with higher ignition points or flash points are preferred to apply in order to provide safe usages at high temperatures during short circuits. Additionally, the low toxic electrolyte is required in case of leakage or disposal.

5) Low production costs are indispensable to commercialize the high-performance electrolytes for LIBs.

2.2.3.2. Components of Liquid Electrolytes

2.2.3.2.1. Organic Solvents

In general, the solvents should meet minimal requirements in accordance with the electrolyte properties. The dielectric constant (ε) of the solvent affects the ionic dissociation and association of Li salts. A higher amount of dielectric constant results in more ability of the solvent to dissolve salts to a sufficient concentration as it is inversely proportional to the Columbic forces between anions and cations of the lithium salt. The solvent should be fluid with low viscosity (η) to facilitate the ion transport. Moreover, it needs to remain inert to the cell components, especially to the charged surfaces of anode and cathode. Additionally, the solvent should have low melting point (T_m) and high boiling point (T_b) to remain liquid in a wide temperature range. It also has to be safe with high flash point (T_f), nontoxic, and economical.

LIBs consist of the strongly reducing anodes and strongly oxidizing cathodes which lead to a high working voltage. Accordingly, organic solvents are employed widely instead of any solvents that have active protons including aqueous electrolytes since the reduction of such protons along with the oxidation of the corresponding anions occur within 2.0 - 4.0 V vs. Li^+/Li^0, while the charge potentials of the anode and the cathode are 0.0 - 0.2 V and 3.0 - 4.5 V, respectively [29]. The organic solvents are categorized into cyclic and linear solvents with difference in physicochemical properties due to their structures as mentioned in table 2.4 [30,31].

Table 2.4. Physicochemical characteristics of organic solvents in Li-ion batteries [30,31].

Solvent	Structure	M.W	T_m	T_b	η	ε	Density

		(g/mol)	(°C)	(°C)	(cP)	(25 °C)	g/cm^3(25 °C)
Cyclic							
Ethylene carbonate (EC)	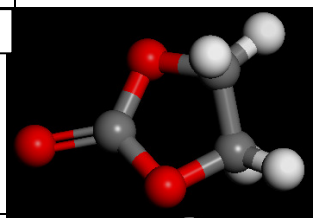	88	36.4	248	1.86 (40°C)	89.78	1.321
Propylene carbonate (PC)	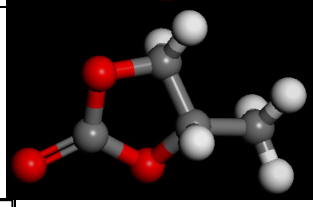	102	-48.4	242	2.53	64.92	1.2
Linear							
Diethyl carbonate (DEC)	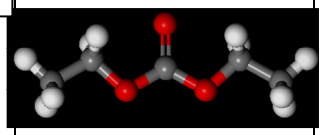	118	-43	126	0.75	2.805	0.97
Dimethyl carbonate (DMC)	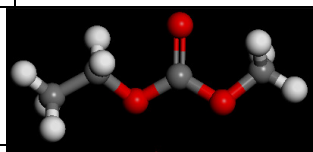	90	0.5	91	0.59	3.11	1.063
Ethylmethyl carbonate (EMC)	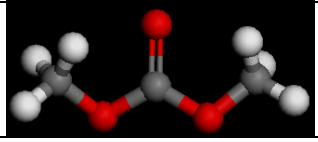	104	-53	108	0.65	2.96	1.00

Although a high dielectric constant and low viscosity are required for the electrolytes to provide high ionic conductivity, a higher dielectric constant commonly results in increased viscosity and polarity. It is noteworthy to mention that the impact of molecular cyclicity on the dielectric constant which is ascribed to the intermolecular strain of the cyclic structures favors the conformation of better alignment of molecular dipole, while the mutual cancellation of these dipoles in linear carbonates is originated from their more flexible and open structure.

2.2.3.2.2. Lithium Salts

Lithium salt is one of the key components affecting the performance of LIBs. Salt association may induce a salt decomposition, thus leading to electrolyte degradation. It determines the number of free ions in an electrolyte, and consequently the electric conductivity. Also, the salt anion along with the decomposed organic solvents play a critical role in the formation of the solid electrolyte interphase (SEI) layer which is electronically insulating but a good conductor of lithium ions to prevent further decomposition of solvents. A lithium salt should meet the following prerequisites to insure the enhanced performance of LIBs [32,33]:

1) It should be able to completely dissolve and dissociate in the non-aqueous media (diverse organic solvents, especially cyclic and linear carbonates), and the solvated ions (especially lithium cations) should be able to move in the electrolyte with high mobility.

2) It should be able to exhibit high ionic conductivity in various non-aqueous solvent systems.

3) It should be able to form the solid electrolyte interfaces on electrodes (especially carbonaceous anodes) with lower resistivity to provide long-term cyclicity and cell safety.

4) It should be capable of passivating an aluminum current collector from anodic dissolution.

5) Both the anion and the cation should remain inert toward the other cell components such as the separator, electrode substrates, and cell packaging materials.

6) The anion should be inert to electrolyte solvents.

7) The anion should be stable against oxidative decomposition at the cathode.

8) The anion should be non-toxic with chemical stability against thermally induced reactions with electrolyte solvents and other cell components.

Table 2.5 shows the physicochemical properties of lithium salts commonly used in LIBs. It is necessary to consider the optimal properties to fulfill the mentioned requirements. For example, anions with larger radii are more desired since the lithium salts having delocalized anions are inclined to dissociate more readily. Generally, the dissociation of lithium salts takes the following order:

$Li(CF_3SO_2)_2N > LiAsF_6 > LiPF_6 > LiClO_4 > LiBF_4 > LiCF_3SO_3$

On the other side, increasing the ionic radius leads to less ionic mobility according to the Stokes' law:

$$\mu_\circ = \frac{\lambda_\circ}{zF} = \frac{ze}{6\pi\eta_\circ r} = \frac{zFD}{RT} \quad (2.1)$$

Where $\mu_\circ$, $\lambda_\circ$, z, F, e, r, $\eta_\circ$, R, and T represent the ionic mobility, the limiting molar conductivity, the charge number, the Faraday constant, the elementary electric charge, the ionic radius, the viscosity, the gas constant, and the absolute temperature, respectively. In this study, lithium hexafluorophosphate $LiPF_6$ was employed as the lithium salt due to its distinguished balanced properties and wide usage where it is briefly introduced in following [34,35].

Table 2.5. Physicochemical properties of representative lithium salts.

Lithium Salts	Molecular weight	Anion diameter (nm)	T_m (^{0}C)	Al Corrosion	σ (mScm^{-1}) (1.0 M, 25 ^{0}C)	
					in PC	in EC/DEC
$LiBF_4$	93.9	0.229	>300[34],293[35]	N	3.4	4.9
$LiPF_6$	151.9	0.254	194[34],200[35]	N	5.8	10.7
$LiClO_4$	106.4	0.237	236	N	5.6	8.4
$LiAsF_6$	195.9	0.260	340	N	5.7	11.1
$Li(CF_3SO_2)_2N$	286.9	0.325	228[34],234[35]	Y	5.1	9.0
$LiCF_3SO_3$	155.9	0.270	>300	Y	1.7	-

Among the great number of salts rivaling for LIBs, $LiPF_6$ was the undisputed winner to be commercialized. As mentioned previously, the success of $LiPF_6$ was not achieved by any single prominent property, but by the combination of well-balanced properties with compromises and restrictions. The anion of $LiPF_6$ can be considered as F^- complexed by Lewis acid PF_5. These anions, also known as anions of super acids, have a structure in which the negative charge is distributed uniformly by the strongly electron-withdrawing Lewis acid ligands. Thus, the corresponding complex salts have lower melting temperature and they are soluble in low dielectric electrolytes which causes higher ionic conductivity. Nevertheless, absorption the trace amount of moisture even in non-aqueous electrolyte solutions in ambient temperature leads to the production of PF_5 as a strong Lewis acid and gaseous product:

$$LiPF_6 + H_2O_{(moisture)} \leftrightarrow LiF + PF_5 \quad (2\text{-}4)$$

It initializes some desired or undesired reactions such as ring opening in the presence of non-aqueous solvents and adsorbing moisture causes the formation of HF since P-F bond are highly susceptible to hydrolysis even at room temperature. Thus, it produces polymeric compounds on the cathodic side that prevents the release of transition metal elements and accordingly restricts the battery operation on thermal runaway. The chemical and thermal instability of the salt do not impede its extensive participation as an electrolyte component. For instance, in the commonly used carbonate solvent mixtures, $LiPF_6$ has a lower dissociation constant but higher ionic mobility than $LiAsF_6$. Also, it shows higher ionic conductivity than $LiBF_4$. It also has excellent solubility and good low-temperature performance. Altogether none of the other salts could meet all these multifaceted requirements simultaneously as well as $LiPF_6$ does [34-36].

2.2.3.2.3. Additives

Employing the electrolyte additives is one the most efficient and economic approaches for the improvement of lithium ion battery performance. Generally, the amount of an additive used in the media is not more than 5% either by weight or volume while its presence significantly enhances the cycle life of LIBs. The additives are categorized according to their functions [37,38] :

1) Facilitate the formation of SEI on the surface of graphite. Vinylene carbonate (VC) and lithium alkyl dicarbonate are some instances of this category.

2) Cathode protection agents- These additives protect cathode material from dissolution and overcharge. LiBOB is one of the additives that are capable of carrying out this duty.

3) $LiPF_6$ salt stabilizers- These agents enhance the thermal stability of $LiPF_6$ against the organic electrolyte solvents. For instance, tris(2,2,2-trifluoroethyl)phosphite (TTFP) is able to stabilize $LiPF_6$- based electrolyte solutions.

4) Safety protection additives which these agents can be classified as overcharge protectors and fire-retardant additives. Tetra-methylphenylenediamine and tetracyanoethylene are the examples of safety protection additives.

5) Wetting agent and viscosity diluter- Wetting additives are normally considered to incorporate in the electrolyte composition when the content of cyclic carbonates, such as EC and PC, is increased to enhance the performance of the batteries at high temperatures. Ionic and non-ionic surfactants, linear eaters with high molecular weight, i.e., dodecyl acetate, methyl decanoate, and a series of eaters of tertiary carboxylic acids are very effective to improve the electrolyte permeation into the electrodes and separator which leads to higher columbic efficiency in the first cycle and reversible capacity of the cell.

Additionally, the electrolyte viscosity is decreased at the low temperatures. It has been claimed that the addition of small amount of P_2O_5 can effectively reduce the viscosity of $LiPF_6$- based electrolytes and consequently, develop the applications of Li-ion batteries at low temperatures [39].

2.2.4. Separators

Separators are non-active components that separate the physical contact between the cathode and the anode to provide a pathway for ion transport. Polyolefins such as polypropylene (PP) and polyethylene (PE) are the commercialized separators employed in LIBs. These separators are the micro porous polymer films with porosity of 30-50 % and pore sizes of 0.03-1 μm. Separators experience redox reactions in contact with the

electrodes where polyolefin separators undergo oxidative decomposition due to their low resistance to oxidation. This oxidative decomposition worsens at higher operating temperatures and eventually reduces cycle characteristics. Although PE separators are widely employed in LIB cells due to their good mechanical strength and electrochemical stability, PP separators are known to be more oxidative resistant than PE. Accordingly, three- layer products consist of PP/PE/PP stacks have a higher oxidative resistance compared to a single layer of PE [40,41].The film thickness of separator should be less than 25 μm to maximize the battery discharge capacity by increasing the concentration of surrounding electrolyte and facilitating movement of the electrolyte components. A good separator should be optimized for improved battery safety and to prevent problems with mechanical strength that may occur during the production process. Accordingly, it should have high ionic flow, negligible electronic conductivity, complete wettability, high chemical stability against electrolytes, adequate physical strength to withstand the assembly process, and high mechanical and dimensional stability. Furthermore, PE and PP have low thermal shutdown temperatures (PE: ~135 ^{o}C and PP: ~165 ^{o}C) which is vital to be considered in case of short circuits. Shutdown is a safety function that cuts off the circuit by blocking micro pores during excess current caused by internal or external short circuits. This phenomenon usually occurs by melting all or parts of the separator, filling the pores and fully preventing ions from flowing between the electrodes [42]. It should be noted that at temperatures above the PE meltdown temperature, there is limited movement of ions and organic solvents through pores which results in deactivation of the battery. Since PE remains mobile at high temperatures, it is difficult to make the electrodes apart or proceed with meltdown during ignition. By stacking PP and PE layers having different meltdown

temperatures, battery safety is enhanced with insulation near the core during short circuits since PP has a meltdown temperature greater by at least 30 ºC. Thus, the method of combining separator layers with different meltdown temperatures is known to provide insulation across a wide range of temperatures.

2.3. Electrochemical and transport properties of electrolytes

Generally, all the key phenomena in electrochemical cells as the most basic unit comprising any battery including lithium ion cells, involve conducting charge particles (ions and electrons) between the electrodes. Since the electrochemical reaction of a cell is based upon a change of oxidation state, the ease of electron-transfer between anode and cathode can dictate the magnitude of the cell's driving force. Electrons are transferred from anode to cathode during the discharge of a cell and vice versa as the battery is charged where the related cell components are electrodes, current collectors, and electrical leads. In addition to electrical conduction, ionic conduction through the electrodes and electrolyte is necessary to complete the electrochemical reaction. Therefore, it is necessary to optimize both electrical and ionic conductivities in electrodes due to their indispensable roles in determining the overall cell properties including cycle ability and capacity stability [43]. However, assuming that motion of ions through the electrolyte and into the electrodes governs charge/discharge rates of the cell, greater emphasis usually falls on ionic conductivity rather than electronic conductivity. Since electrolytes serve as the medium to provide ionic conduction path between the electrodes as their basic function, enhancement of the electrolytic conductivity is the prime concern to achieve an optimized characteristics of the cell. Although many contributions on thermodynamic properties of alkyl carbonates mixed with salts have been described in the literature, little information has been provided

regarding the correlation between interfacial properties of the electrolyte and an electrode with electrochemical performance of the cell [44-47]. The effect of salt concentration and temperature dependent properties of Li-ion battery on wettability and conductivity has been illustrated schematically in Fig. 2.5.

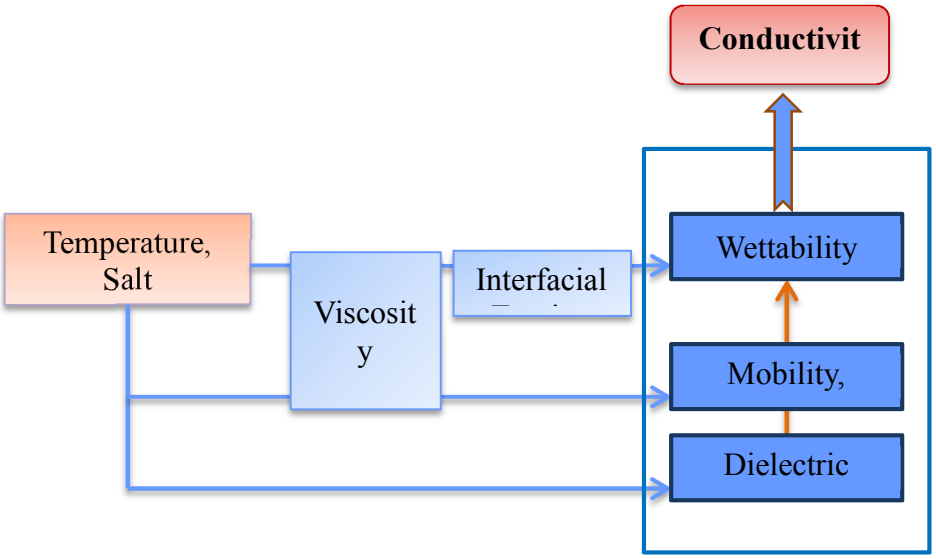

Fig. 2.5 Correlation of temperature and salt concentration with conductivity.

The chart shown in Fig. 2.5 briefly illustrates the relationship between the temperature/salt concentration and conductivity. The viscosity of an electrolyte inversely changes with temperature while there is a consistent relationship between salt concentration and viscosity of the solution. These two variables may affect interfacial tension and wetting properties with respect to the viscosity and dielectric constant of the solvents. Moreover, there is an undisputed relationship between salt concentration and dielectric constant of the solvents as their ability to dissociate salt ions. Thus, this solvent property directly impacts ion conductivity and subsequently, electrolyte-electrode/separator wettability by the same procedure that mobility and diffusivity of ions act. The mentioned relationships are explained more comprehensively in the following.

In liquid electrolytes, the transport of ions is realized via a three-step process: (1) the solvation and dissociation of crystalline salts as ionic compounds by polar solvent molecules, (2) the migration of these solvated ions through the electrolyte, and (3) the interaction of electrolyte species with separator and electrodes. When lithium salts such as $LiPF_6$ are dissolved in a solvent, cations (Li^+) and anions (PF_6^-) are produced and dissociation of salt is determined by the dielectric constant of the solvent as its polarity. Solvation occurs since the Li ions are wholly encircled by the solvent molecules reducing the influence of the anion. Accordingly, salts with large anions are lucrative for higher solubility and conductivity due to their uniform distribution of charge and prevention of ionic pairing as a result [48].Consequently, dielectric constant ε of the solvents and charge carrier number are consistently related to each other. Charged particles, comprising lithium ions, can cross the electrolyte under two driving forces: a concentration gradient and an externally applied electric field. Diffusivity, which is generally described by the Fick's law as Eq. 2.2, demonstrates the effect of concentration gradient in facilitating the movement of ions through the electrolyte, and the degree of ease with which ions pass through the media in presence of an external electric field is represented by ionic mobility as a viscosity dependence phenomenon. The mobility of an ion μ_i is known to vary inversely with its solvated radius and viscosity of the electrolyte η according to the Stokes-Einstein relation expressed in Eq. 2.3 [49,50]:

$$J = -D\nabla \mathrm{c} \tag{2.2}$$

Where J is the diffusion flux (amount of media per unit area per unit time), D is the diffusion coefficient, and $\nabla \mathrm{c}$ indicates the concentration flux. The experimental value of

lithium ion mobility is measured by methods such as nuclear magnetic resonance (NMR) spectroscopy [51].

$$\mu_i = \frac{1}{6\pi\eta\, r_i} \tag{2.3}$$

Thus, the viscosity determines the motion of ions where low viscosity facilitates ionic movement. Cationic (Li^+) transport in electrolytes, as dictated by the viscosity and solvating power of the solvents, is expressed as the transport (t^+) and transference (T^+) numbers. The transport number expressed by Eq. 2.2 is defined as the net charge carried by the cations out of the total charge carried by both the cations and anions passing across a reference plane [52]:

$$t^+ = \frac{i_+}{i_+ + i_-} = \frac{i_+}{i_t} = \frac{u_+}{u_+ + u_-} = \frac{D_+}{D_+ + D_-} \tag{2.4}$$

Where i_+ and i_- are the currents carried by the cations and the anions, respectively, i_t is the total current, and $u_\pm$ and $D_\pm$ are the mobility and the diffusion coefficients of the cations and the anions, respectively.

Practically, since the according measurements cannot be specified to either of the anions or cations groups, the associated solvent molecules are considered which induce drag such as resistance. Consequently, transference number is employed instead of transport number. The transference number of a Li-ion is measured experimentally using the following Eq. [53]:

$$T_{Li^+}^+ = \frac{R_b}{\frac{\Delta V}{I(\infty)} - R_{ct}} \tag{2.5}$$

Where ΔV is the polarization voltage, $I(\infty)$ is the steady state current after polarization, R_b and R_{ct} are the bulk resistance and the charge transfer resistance, respectively, in the complex impedance spectra before polarization. It is noteworthy to mention that the ionic conductivity of the electrolytes is measured empirically by employing the standard complex impedance method using an electrochemical work station in a particular frequency range.

At the salt concentrations less than 1M, the number of free ions increases with salt concentration in conjunction with ion conductivity until it peaks at a higher concentration. However, after the highest conductivity is reached, the conductivity no longer depends on the number of ionic carriers in the solution while it is determined by the mobility of ionic carriers in the electrolyte. Hence, any increase in salt concentration results in higher ion aggregation due to the insufficient dielectric constant value of solvents and existence of many species including dissociated and undissociated salt in the solution which retard the movement of free ions and lead to higher viscosity of the solution as well as a decrease in conductivity. The value of maximum conductivity as a function of salt concentration is determined by the dielectric constant of the solvents in collaboration with temperature. Generally, a higher dielectric constant would shift the occurrence of ion pairing to higher salt concentrations, while a higher temperature reduces the solution viscosity. The common result of both scenarios is the shift of maximum conductivity to higher salt concentrations. Nernst-Einstein Eq. validates the undisputed impact of number of ionic carriers, diffusivity, and temperature on the ionic conductivity [54]:

$$\kappa = \frac{q_i^2 .\ N_i}{k_B\ .\ T} D_i \tag{2.6}$$

Where N is the particle density of the charge carriers and q and k_B are the ion charge and the Boltzmann constant, respectively.

Additionally, Ionic conductivity σ as the quantified measurement of the electrolyte ion conduction ability is affected by solvation/dissociation and the subsequent migration in terms of the free ion number n_i and ionic mobility μ_i, respectively [55]:

$$\sigma = \sum_i n_i \, \mu_i Z_i e \tag{2.7}$$

Where Z_i is the valence order of ionic species i, and e is the unit charge of electrons, respectively. For a single salt solution, the cations and anions are the only two charged species present.

When the electrolyte has high viscosity, the wetting of separator and electrodes is more difficult since the Li ions are not able to easily migrate to the mentioned cell components and through them, particularly during the first cycle. Additionally, high viscosity can strongly attenuate the uniform wettability of the electrodes because of the quasi three-dimensional fractal nature of the electrodes. Wetting in the electrodes and separator is monitored principally by the electrolyte penetration and spreading in pores. Electrolyte penetration is controlled by viscosity. On the other side, electrolyte spreading is determined by interfacial tension. Therefore, characterization and prediction of wetting phenomenon by calculating the surface energy at the interface of liquid-solid components is a useful approach to optimize the electrochemical performance of LIBs.

2.4. Interactions of electrolytes and electrodes/Separators

Interfacial tension is the force per unit length that exists at the interface between molecules of electrolyte and electrodes/separator. It results from an imbalance of intermolecular attractive forces, the cohesive forces, between the adjacent liquid molecules. As Fig. 2.6 illustrates, the molecules in the bulk liquid experience cohesive forces with other molecules in all directions but the molecules at the surface of the liquid experience an inward force towards the bulk or middle of the liquid.

On the other hand, forces of attraction between a liquid and a solid surface are called adhesive forces. The difference in strength between cohesive forces and adhesive forces determines the behavior of a liquid in contact with a solid surface. In other words, in the bulk of the liquid, each molecule is pulled equally in every direction by neighboring liquid molecules, resulting in a net force of zero.

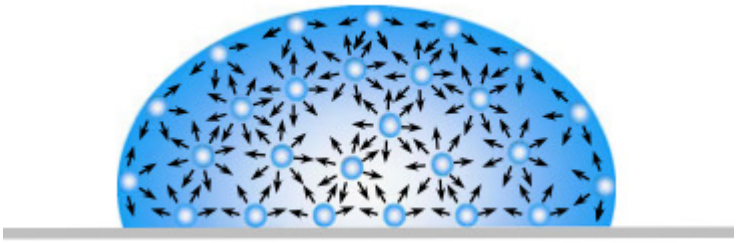

Fig. 2.6 Diagram of the forces on molecules of a liquid. In the bulk of the liquid, the forces are same in all directions, while at the surface the net effect is downward into the interior [56].

At the surface of liquid, the molecules are pulled inwards by other molecules deeper inside the liquid and are not attracted as intensely by the molecules in the neighboring medium. Therefore, all of the molecules at the surface are subject to an inward force of molecular attraction which is balanced only by the liquid's resistance to compression, meaning there is no net inward force. However, there is a driving force to diminish the

surface area. Therefore, the surface area of the liquid shrinks until it has the lowest surface area possible. Interfacial tension of a fluid interface can be defined mainly by employing thermodynamic aspect of view or mechanically. Thermodynamically, it is the excess free energy as the difference of the free energy of adhesion and cohesion per unit area caused by the presence of the interface. The energy per molecule is greater in the interfacial region than in the bulk liquid. From mechanical point of view, interfacial tension is the force per unit length parallel to the interface, i.e., perpendicular to the local density or concentration gradient and it requires the knowledge of the tangential and normal components of the pressure at the interface.

Experimental characterization of solid/liquid interfacial tension and consequently, wetting phenomenon, is applied based on the Young's Eq. represented by Fig. 2.7 and Eq. 2.8 as the infrastructure of many methods using contact angle (CA) measurements through the sessile drop method and surface free energy (SFE)calculations [57,58].

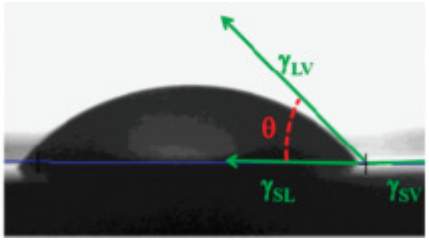

Fig.2.7 Interfacial tension measurement based on the contact angle snapshot [59].

$$\gamma_{SL} = \gamma_{sv} - \gamma_{Lv}cos\theta \qquad (2.8)$$

Where γ_{SL} is the solid-liquid interfacial tension energy while γ_{sv} and γ_{Lv} are the surface energies required to create a unit area of solid- vapor and liquid-vapor interfaces, respectively.

Organic solvent composition, lithium salt concentration, and temperature may influence the wettability of electrodes and separator due to changes in the viscosity and interfacial tension of the electrolyte affected by temperature and the dielectric constant value of the solvents. In general, interfacial tension decreases when temperature increases because cohesive forces decrease with an increase of molecular thermal activity. There are two empirical equations that relate surface tension and temperature [59]:

- Eötvös:

$$\gamma V^{\frac{2}{3}} = k(T_C - T) \tag{2.9}$$

Where V is molar volume (V = M/ρ; M: molar mass, ρ: density), k is a constant valid for all liquids. The Eötvös constant has a value of 2.1×10^{-7} J/(K·mol$^{2/3}$), and T_c is critical temperature at which the surface tension goes to zero.

- Guggenheim-Katayama:

$$\gamma = \gamma^*(1 - \frac{T}{T_C})^n \tag{2.10}$$

Where γ* is a constant for each liquid and n is an empirical factor, whose value is 11/9 for organic liquids. This Eq. was also proposed by Van der Waals, who further proposed that γ* could be given by the expression $K_2T_c^{1/3}P_c^{2/3}$ where K_2 is a universal

constant for all liquids, and P_c is the critical pressure of the liquid (although later experiments found K_2 to vary to some degree from one liquid to another).

While wettability and ion conduction are mainly affected by the interplay between the viscosity and dielectric constant of the electrolyte components, studying the solvation phenomenon as the infrastructural process should be considered indispensably. During the solvation, the salt dissociation occurs and the stability of the salt crystal lattice is energetically compensated by the coordination of solvent dipoles with the salt ions (cations). Thus, these ions are surrounded by a mobile solvation sheath which is incorporated with a certain number of oriented solvent molecules. Accredited by the results gained from various modeling approaches including ab initio quantum mechanics and also a new mass spectrum (MS) technique, the small ionic radius of lithium cannot be coordinated by more than four solvent molecules regardless of the solvent type where the peaks corresponding to Li $(solv)_{2\sim3}^{+}$are the most abundant [60]. In addition, the MS technique endorses the stability of the solvation sheath during the salt ions migration via the electrolyte, which confirms the belief that the composition of solvated lithium ion shell remains unchanged during its migration in an electrolyte solution [61]. Considering that both cation and anion could be coordinated by solvents, ion conduction actually consists of the oriented movement of ion/solvent complexes of both charges. It is noteworthy to mention that lithium ions are more favorable to be solvated due to their small current portion in the non-aqueous electrolytes which caused by the high surface charge density on the cations due to their small ionic radii. Therefore, the cations move at a slower speed with the solvation sheath while high populations of anions are relatively free.

During the dissociation process of a certain salt lattice, the solvation of the ions is more energetically favored by a solvent molecule with a higher relative dielectric constant. This selective solvation of lithium ions excludes the solvents with low viscosity such as the linear carbonates from the solvation shell and leaves them as the non-coordinating molecules which impart their low viscosity to facilitate the migration of solvated ions. Microscopic investigations depict that the solvents involved in the solvation sheath and migrate with the lithium ions to electrode surfaces have more contribution in the oxidative or reductive processes and thus, more highlighted role in the electrochemical stability of the electrolytes. This phenomenon has a profound impact on the chemical nature of the electrolyte/electrode interfaces (i.e., SEI layer). This layer consists of the electrolyte decomposed components and sieves the charge and mass transfer across the electrodes. The existence of SEI constitutes the foundation on which lithium ion chemistry could operate reversibly. As a result, an ideal SEI should meet some important requirements such as (i) the electron transference number of zero and low solubility in electrolytes to prevent electron tunneling, persistent decomposition of electrolyte, and consumption of the limited source of lithium from the cathode, (ii) high ion conductivity to encourage the ion migration to intercalate into or deintercalate from the electrode, and (iii) uniform morphology and chemical composition to assure homogeneous current distribution and good adhesion to the electrode surface [62,63].

3. Previous Analytical and Computational Models

Molecular dynamics (MD) simulations can be used to derive equilibrated electrolyte structures, and resulting atomic trajectories are employed to examine electrochemical properties and interfacial phenomena. MD simulations are particularly well suited for studying the electrolytes used in LIB since ions move sufficiently far on times scales accessible to MD simulations (multiple nanoseconds). In this chapter, we briefly discussed some of the most common procedures employed to explore the electrochemical and wetting properties of electrolytes. Previously, the simulations were conducted with various molecular dynamics software packages such as Materials Studio [64], GROMACS [65], LAMMPS [66], CHARMM [67], AMBER [68], MDNAES [69], and Lucretius [70]. In this Chapter, we provide an overview of the previous analytical and computational efforts on quantifying the solvent material properties including conductivity, diffusivity, dielectric constant, and interfacial energy.

3.1. Conductivity

The isotropic ionic conductivity is calculated by the Nernst-Einstein relation considering the collective mean-square displacement in MD simulations. The mentioned relation was introduced by Borodin et al. as follows [71]:

$$\lambda = \lim_{t\to\infty} \lambda^{app}(t) = \lim_{t\to\infty} \frac{e^2}{6tVk_BT} \sum_{i.j}^{N} z_i z_j \langle ([R_i(t) - R_i(0)])([R_j(t) - R_j(0)]) \rangle \quad (3.1)$$

Where e is the electron charge, V is the volume of the simulation box, k_B is Boltzmann's constant, T is the temperature, t is time, z_i and z_j are the charges over ions I and j in electrons, $R_i(t)$ is the displacement of ion i during time t, the summation is performed over all ions,⟨⟩ denotes the ensemble average, and N is the total number of ions in the simulation box. For the anisotropic system, Eq.3.1 will yield an average over all directions. $\lambda^{app}(t)$ is the apparent time-dependent conductivity whose long-time limit determination is problematic even at high temperatures where the diffusion coefficients can be accurately determined because $\lambda^{app}(t)$, being a collective property, has poorer statistics and a higher uncertainty compared to MSD(t).The isotropic conductivity as an off-diagonal term decreases the total charge transport arising from cations and anions moving in the same direction (correlated ion motion). By assuming that the diffusion of individual species independently contributes to the total ionic conductivity of the system and that there are no correlated motions, conductivity can be decomposed into an ideal conductivity that would be realized if ion motion were uncorrelated, denoted $\lambda_{uncorr}(t)$ due to the diagonal (i = j) terms in Eq. 3.1, and α_d as the degree of uncorrelated ion motion [71].

$$\lambda_{uncorr}^{app} = \lim_{t\to\infty} \lambda_{uncorr}^{app}(t) = \lim_{t\to\infty} \frac{e^2}{6tVk_BT} \sum_{i}^{N} z_i^2 \langle [R_i(t) - R_i(0)]^2 \rangle$$

$$= \frac{e^2}{Vk_BT} \left(n_+ D_+^{app} + n_- D_-^{app} \right) \quad (3.2)$$

Where n_i is the number of atoms of type i (Li^+ or PF_6^-) and D_i is the apparent diffusion coefficient.

The degree of uncorrelated ion motion is given as the ratio of the collective (total) charge transport (λ) to the charge transport which is only caused by self-diffusion (λ_{uncorr}). Thus, the Nernst-Einstein Eq. is obtained as [71]:

$$\alpha_d = \frac{\lambda}{\lambda_{uncorr}} = \lim_{t\to\infty} \alpha_d(t) = \lim_{t\to\infty} \frac{\lambda^{app}(t)}{\lambda^{app}_{uncorr}(t)} \tag{3.3}$$

While,

- α_d = 1 occurs when there is completely uncorrelated ion motion, and
- α_d = 0 corresponds to the situation where all the cations only move together with anions.

Fig. 3.1and 3.2 illustrate some of the results obtained by employing Eq. 3.1 and 3.2 regarding the carbonate-based electrolytes in literature. The trend of conductivities calculated by the Nernst-Einstein equation in Fig. 3.2 is same as that of ion diffusivity where conductivity of pure DMC systems is conspicuously higher than pure EC systems and the intermediate values are assigned for mixed EC-DMC systems. Comparing the results of uncorrelated and correlated (true) conductivities, it can be figured out that the trend of values obtained for the pure systems are in contrary to the Nernst-Einstein conductivities.

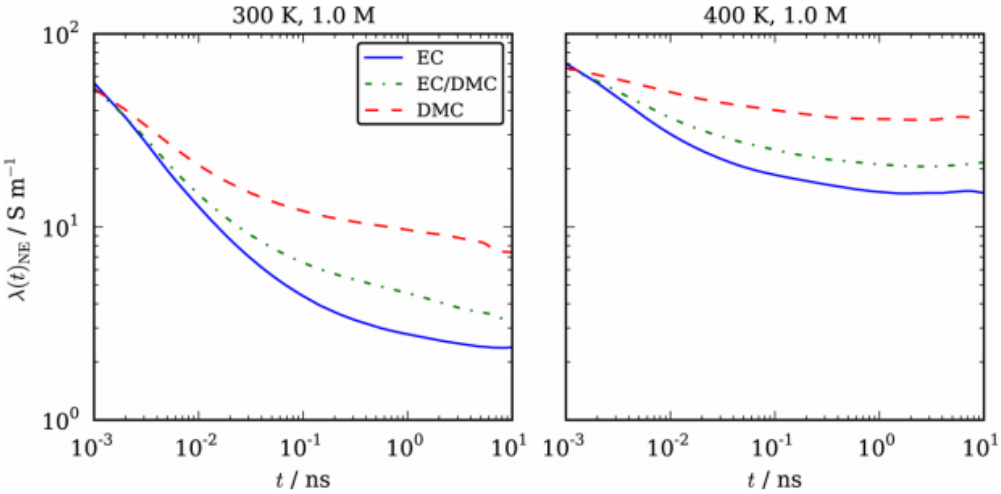

Fig. 3.1 Uncorrelated (theoretical Nernst-Einstein) ion conductivity $\lambda_{NE}(t)$ vs. time for 1.0 M $LiPF_6$ in EC, DMC, and EC-DMC solvents at 300 and 400 K [72].

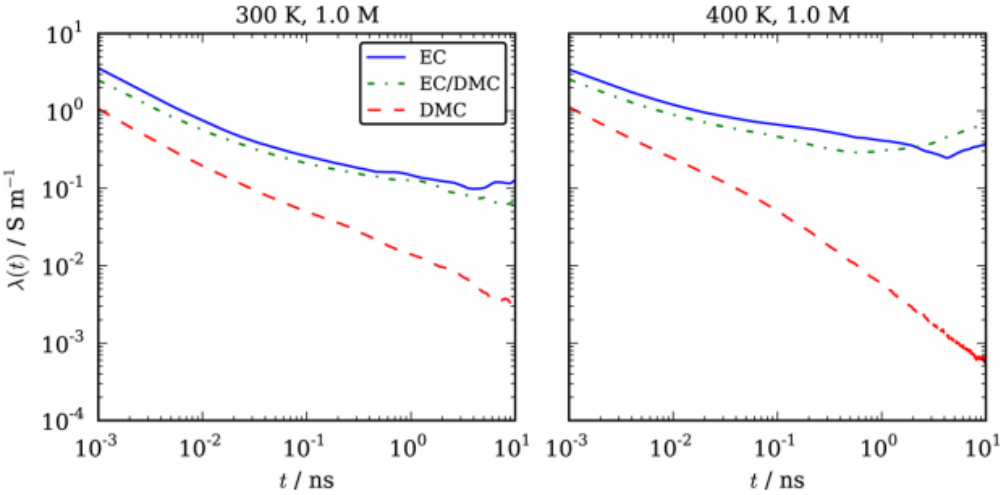

Fig. 3.2 Correlated ion conductivity λ (t) vs. time for 1.0 M $LiPF_6$ in EC, DMC, and EC-DMC solvents at 300 and 400 K [72].

Consequently, according to all these observations, conductivity can strongly be influenced by correlated ion movement which varies significantly between solvents [72]. The total and true ion conductivities may not necessarily reflect the ability of electrolyte to conduct lithium-ion. Therefore, Li^+ transference number is calculated in molecular dynamics simulations according to the Eq.2.5 by considering the number of ions of type *i*.

3.2. Diffusivity

The self-diffusion coefficients of ions/molecules were calculated from the mean-square displacement (MSD) of the species center-of-mass using the Einstein relation in MD simulations [73]:

$$MSD(t) = \frac{1}{N}\sum_{i=1}^{N}\langle[\,r_i(t) - \,r_i(0)]^2\rangle \tag{3.4}$$

$$D_i = \lim_{t\to\infty}\frac{MSD_i(t)}{2nt} \tag{3.5}$$

Where $r_i(t)$ is the coordinate of center of the mass *i* at time *t*, and ⟨⟩ denotes an ensemble average, *n* is the dimensionality of the space as n=3 is used for 3-D diffusion in the solution, n=2 for the diffusion within a particular slab (x-y plane), and n=1 for the diffusion perpendicular to the slab (z-direction), respectively.

Self-diffusion coefficient values for some one-component and binary electrolytes were calculated by researcher employing atomistic modeling for carbonate solvents. Some of the results are depicted in Fig. 3.3. According to the results, since both self-diffusion and inverse viscosity of solvents are composition-dependent properties, the effects of increasing the weight fraction of EC as a cyclic solvent are in contrary with having higher diffusivity and inverse viscosity.

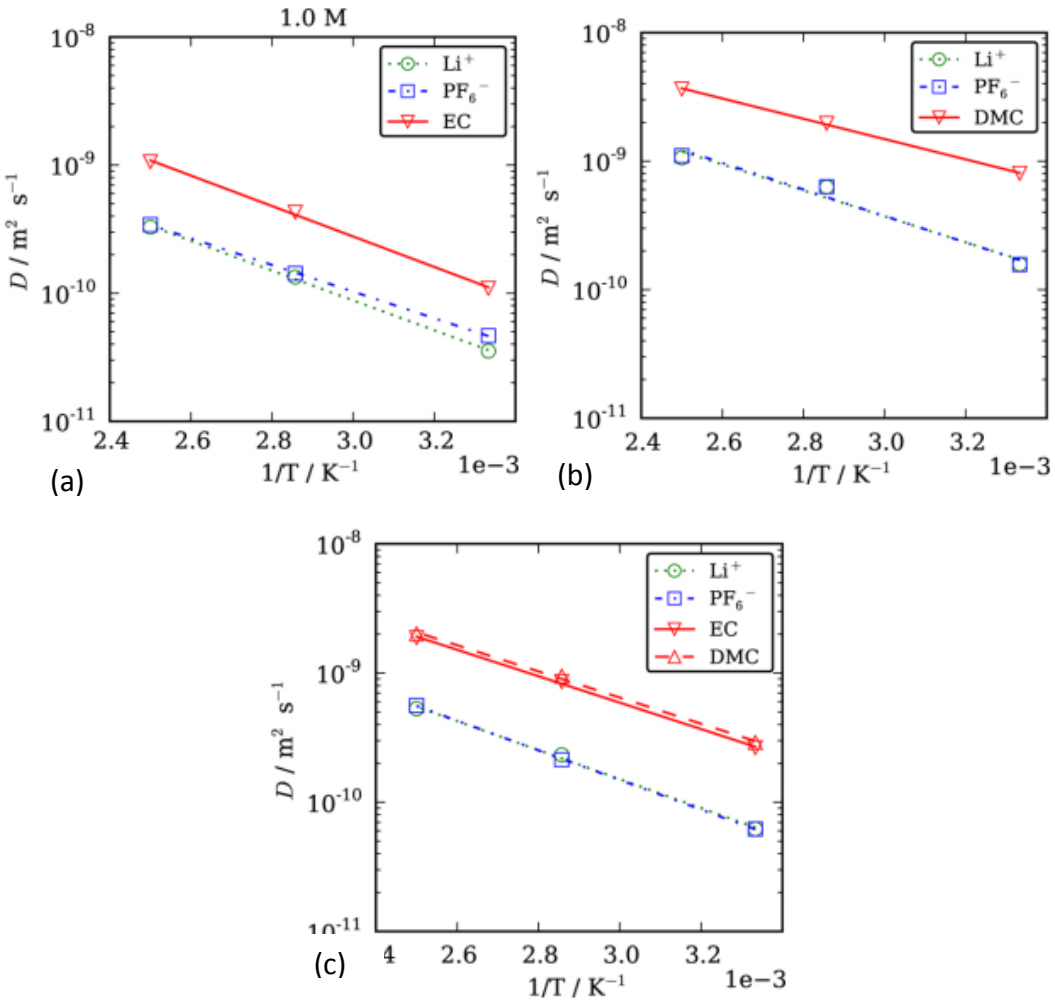

Fig. 3.3 Ion and solvent diffusion coefficients versus 1/T for 1.0 M $LiPF_6$ in (a) EC, (b) DMC, and (c) EC-DMC system [72].

The trend is reasonable due to the high viscosity and melting point of EC compared with DMC. In binary EC/DMC electrolyte system, diffusion coefficients of EC and DMC are approximately equal to the average of values for pure EC and DMC systems because they mutually affect each other. Due to the formation of bulky, slowly diffusing molecular clusters associated with the ions, solvent diffusivities are 2-5 times larger than ion diffusivities for any studied system. Additionally, it is noteworthy to mention an interesting achievement gained by Borodin and Smith [74,75] by employing a quantum chemistry

study in collaboration with MD simulations to shed more light on the Li^+ transport mechanism in carbonate-based electrolytes. They quantified the fraction of vehicular motion, i.e., motion of lithium-ion along with its first solvation shell and the fraction of cation motion belonged to its self-diffusivity during exchange of the solvent molecules. The approach is based on calculating the residence time of a particular solvent molecule in the Li^+ first solvation shell, and as a result, the distance a lithium-ion can travel along with a solvent according to the size of the solvent molecule. Predictably, the contribution of vehicular mechanism would be increased as the cation travels longer with the solvent molecule. The results reveal that there is an equal contribution for vehicular and solvent exchange motion during the Li^+ transport in the carbonate-based solutions.

3.3. Dielectric Constant

The dielectric constants of pure carbonate solvents and binary mixtures have been determined by employing polarizable and non-polarizable MD simulations performed by the relevant force fields such as APPLE&P many-body polarizable force field [76] and COMPASS, AMBER, and CHARMM as the instances for non-polarizable force fields. These two methods are applied in collaboration with molecular dynamics with electronic continuum (MDEC) model and density functional theory (DFT) calculations.

Neumann's dipole moment fluctuation formula is used to obtain dielectric constants [77]:

$$\varepsilon = \varepsilon_\infty + \frac{4\pi}{3Vk_BT}\langle M^2 \rangle \tag{3.6}$$

Where ε_∞ is the high frequency dielectric constant, and $\langle \mathrm{M}^2 \rangle$, V, k_B, and T are the mean square fluctuation of the total dipole moment, volume, the Boltzmann constant, and temperature, respectively. With applying the polarizable MD simulations, dielectric constants are directly estimated by calculating $\langle M^2 \rangle$ and ε_∞ which can be obtained from DFT calculations or experiments ($\varepsilon = \varepsilon_{pol-MD}$). However, as reported in recent studies [78], the dielectric constant obtained with non-polarizable force fields does not explicitly describe pure electronic polarization of the electrolyte. The reason is that the fixed (additive) partial charges in the non-polarizable force fields cannot describe the screening effect by the electronic polarization and MDEC model is employed as the solution. The MDEC model considers point charges moving in electronic continuum of known dielectric constant where $\varepsilon_{el} = \varepsilon_\infty$. In this case, all electrostatic interactions are scaled by the factor$1/\varepsilon_\infty$, while the electronic polarization energy of the solvated charges is calculated explicitly using the electronic continuum mode. There is a simple scaling relation between the total dielectric constant ε and ε_{non-MD}:

$$\varepsilon = \varepsilon_\infty \cdot \varepsilon_{non-MD} \tag{3.7}$$

According to the MDEC scaling procedure, ε_{non-MD} is calculated by Eq. 3.8 where $\langle M^2_{non-MD} \rangle$ is the mean square fluctuation of the dipole moment obtained by the non-polarizable MD and $\langle M^2_{non-MD} \rangle = \langle M^2 \rangle / \varepsilon_\infty$.

$$\varepsilon_{non-MD} = 1 + \frac{4\pi}{3Vk_BT} \langle M^2_{non-MD} \rangle \tag{3.8}$$

Therefore, the dielectric constants can be calculated through non-polarizable MD simulations by knowing the values of ε_∞.

High frequency dielectric constants ε_∞ are determined for pure linear and cyclic solvents with high accuracy employing DFT calculations, while the mixing rule of Lorentz-Lorenz should be applied for the mixing systems:

$$\frac{\varepsilon_{\infty,12}-1}{\varepsilon_{\infty,12}+2} = \phi_1\left(\frac{\varepsilon_{\infty,1}-1}{\varepsilon_{\infty,1}+2}\right)+\phi_2\left(\frac{\varepsilon_{\infty,2}-1}{\varepsilon_{\infty,2}+2}\right) \tag{3.9}$$

Where$\varepsilon_{\infty,12}$,$\varepsilon_{\infty,1}$, and $\varepsilon_{\infty,2}$are the high frequency dielectric constants of the mixture and the pure components respectively, and ϕ_1 and $\phi_2$are the volume fractions.

Fig. 3.4 and 3.5 illustrate the dielectric constants of PC, DMC, and EC as one-component systems and mixtures of PC + DMC and PC + EC, which were calculated as the results of polarizable MD, non-polarizable MD, and non-polarizable MD model applying scaling factor ε_∞ (MDEC) in the literature [84]. According to the following results, the ε values obtained by polarizable MD and MDEC are close to each other especially in the cases of cyclic solvents and binary electrolytes. Polarizable MD method produced much more accurate values compared with the non-polarizable MD for all the species while particularly for the high-dielectric cyclic carbonates (EC and PC) the values predicted by the non-polarizable MD were reported as 1/3 of experimental data. Additionally, the slow convergences of dielectric constants are a well-known fact due to their dependency upon long-ranged and collective fluctuations. Furthermore, increasing the mole fraction of the component that possesses higher dielectric constant in binary solutions (PC and EC in PC + DMC and PC + EC, respectively) results in having a more polar electrolyte.

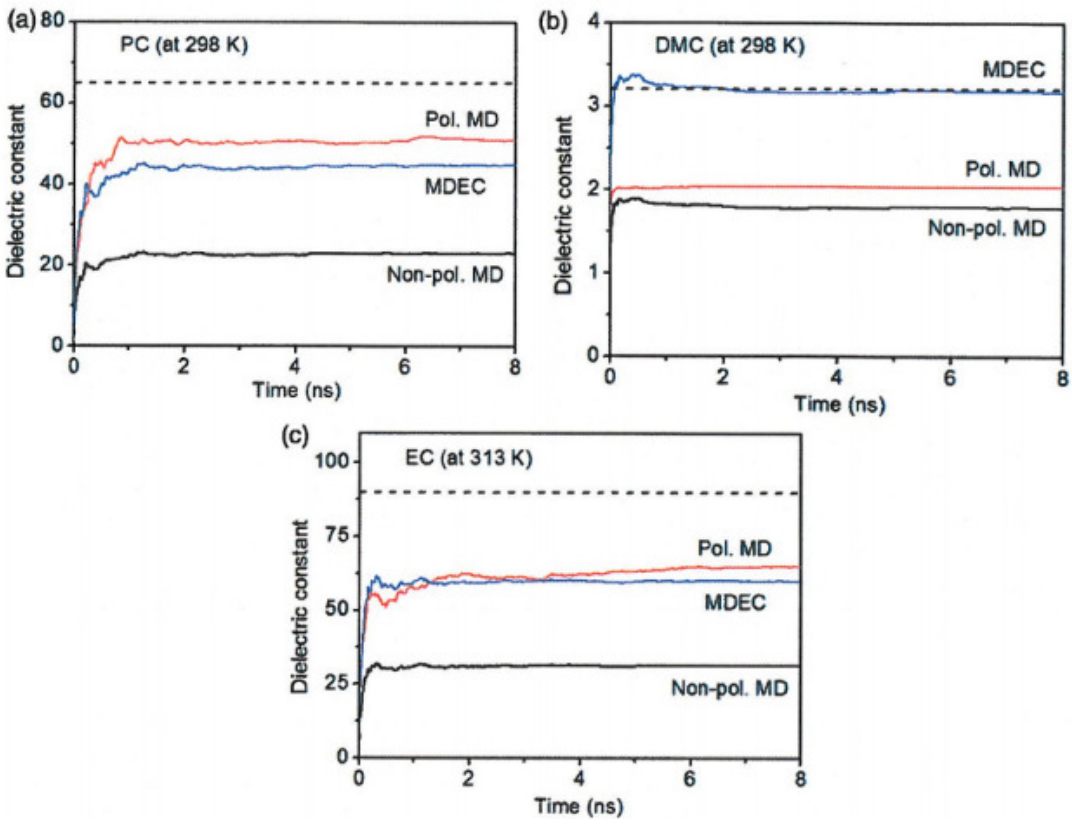

Fig. 3.4 Cumulative average of dielectric constants for (a) PC, (b) DMC at 298 K, and (c) EC at 313 K calculated by polarizable MD, non-polarizable MD, and MDEC. The dotted lines represent the experimental data [77].

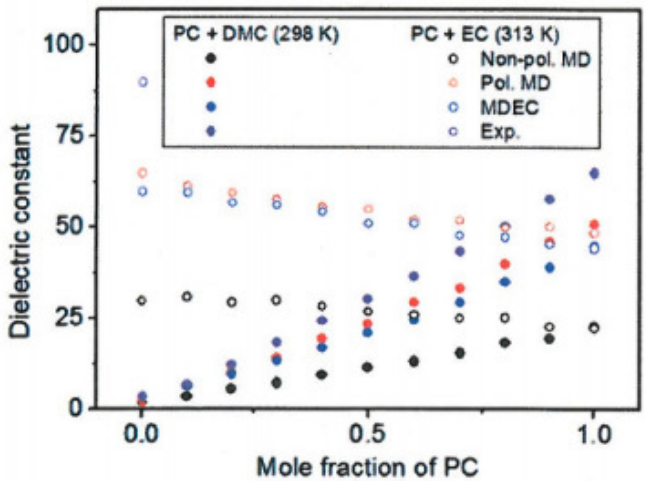

Fig. 3.5 Dielectric constants of PC + DMC at 298 K and PC + EC at 313 K calculated by polarizable MD, non-polarizable MD, MDEC, and experiment [77].

3.4. Wettability and Interfacial Tension

The direct evaluation of the interfacial tension in solid and fluid systems using computer simulations has followed two routes, the mechanical method based on the Clausius virial theorem [79] and the thermodynamic method based on the Helmholtz (or Gibbs) free energy [80]. Atomistic modeling of interfacial energy and wetting properties of carbonate-based electrolytes with the electrodes and separator were rarely investigated in the literature which shed more light on the unique aspect of this study [81]. Nevertheless, numerous researches have focused on studying the liquid-solid contact angle and interfacial tension in different other systems by employing the main following molecular dynamics (MD) methods:

- Thermodynamic integration (cleaving method)
- Pressure tensors calculation
- The interface fluctuation method
- Sessile drop method

3.4.1. Thermodynamic integration (cleaving method)

The direct determination of the crystal-fluid interfacial energy can be achieved by thermodynamic integration applying the definition of γ_{SL} as the reversible work required forming a unit area of the interface. This method is performed along a continues path beginning with separate crystal and fluid bulk systems prepared at the coexistence conditions and ending with a system containing a crystal–liquid interface at equilibrium with the surrounding bulk phases. The construction of such a path requires the development

of a procedure to reversibly cleave a simulation box into two non-interacting systems. Fig. 3.6 depicts the following steps that should be considered to fulfill this goal:

Step 1: Gradually introduce an external "cleaving potential" into the solid at a specific position between two adjacent crystal layers of a specified orientation while maintaining the periodic boundary conditions.

Step 2: Cleave the liquid system in a similar way.

Step 3: Juxtapose the cleaved crystal and liquid systems by rearranging the boundary conditions while maintaining the cleaving potentials.

Step 4: Gradually remove the cleaving potential from the combined interfacial system.

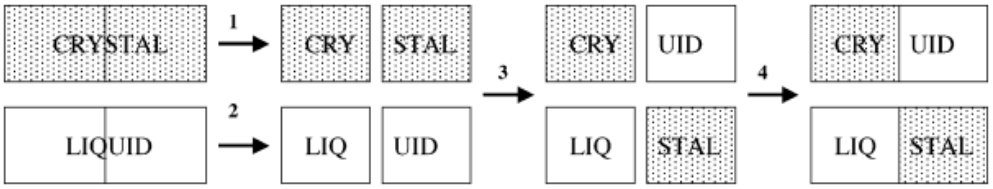

Fig. 3.6 The procedure of calculating interfacial energy by employing the thermodynamic integration method [82].

In addition to the coexistence conditions, the result also depends on the orientation of the crystal with respect to the interfacial plane. The plane along which the crystal and liquid systems are split is referred as the "cleaving plane". The location of the cleaving plane in the crystal system is chosen in the center of the simulation box between two crystal layers, while in the liquid system the precise location is arbitrary [83].

The reversibility and precision of the thermodynamic integration process are very sensitive to the choice of cleaving potentials. The requirements for the cleaving potential are two-fold: First, the cleaving potential should perturb the system as little as possible. Consequently, it is desirable that, in Step 2, the potential introduces structure into the cleaved liquid which is compatible with the structure of the crystal layers. Second, the cleaving potential must be strong enough to prevent the particles from crossing the cleaving plane. Otherwise, the rearrangement of the boundary conditions in Step 3 cannot be performed. On the other side, an approach for constructing a set of rather complicated cleaving potentials should be optimized specifically for each system and it is not easily adaptable to a general case. Researchers solved this problem by implementing the cleaving process using a pair of "cleaving walls" placed on either side of the cleaving plane [82]. For the hard sphere system as the representative of the systems studied by thermodynamic integration, the walls were constructed of layers of hard spheres frozen in the ideal positions of the specified crystal orientation. Each wall interacts only with the system on the opposite side of the cleaving plane as illustrated in Fig. 3.7. Therefore, if the distance z of the walls to the cleaving plane is larger than the sphere diameter σ, the walls do not interact with the system.

The cleaving process in Steps 1 and 2 is performed by gradually moving the walls toward the cleaving plane from the initial position $z = z_i$, which is just outside the range of the interaction potential (σ) determined by the cut-off radius r_w. The final wall position z_f is determined by the requirement that the cleaving potential is sufficiently strong to prevent the particles from crossing the cleaving plane. The interfacial energy is obtained by the sum of works done through these four steps [84].

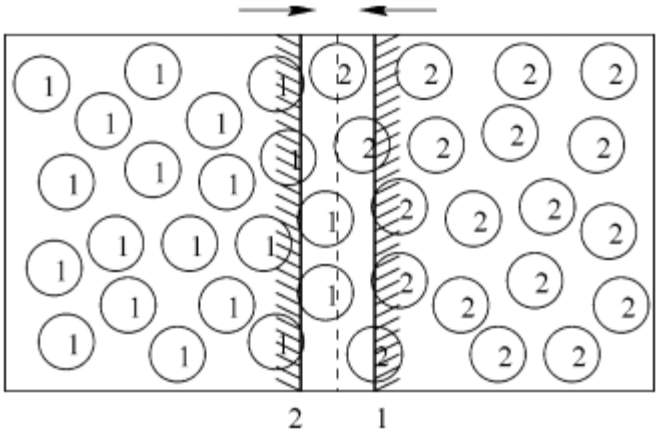

Fig.3.7 Two moving walls and spheres are assigned as types 1 and 2 according to their position with respect to the cleaving plane indicated as the dashed line. The walls interact with the spheres of similar type and placed on the opposite sides where potential plane is the reference. Initially, there is no collision between walls and spheres and the system is then cleaved by moving the walls in directions indicated by the arrows [82].

To calculate the reversible work in steps 1, 2, and 4, the wall position z is considered as the integration coordinate. The reversible work is thus determined by evaluating the integral:

$$w_{1,2,4} = -\int_{z_i}^{z_f} \langle \frac{\partial \Phi}{\partial z} \rangle \, dz \tag{3.10}$$

Where the angle brackets denote averaging over a simulation run at a fixed cleaving wall position. Since interactions in the crystal are usually dominated by the short-range repulsive part of the potential, it is sufficient to choose the interaction potential of the wall particles as a monotonically decreasing function $\Phi(r)$ with a relatively small cut-off radius r_w. The cleaving potential $\Phi(r,z)$ is constructed from the potentials of wall particles $\Phi(r)$ in such a way that each wall interacts only with the system on the opposite side of the cleaving plane. In Step 4, the initial and final positions of the walls are reversed. Because of the

repulsive character of the cleaving potential, the work in Steps 1 and 2 is expected to be positive, while it is negative in Step 4.

In hard sphere systems, the work needed to rearrange the boundary conditions of the cleaved interfaces in Step 3 is zero since the spheres do not have any interaction when they are not in contact with each other. In contrary to hard spheres, the boundary rearrangement work in Step 3 is nonzero for systems with continuous interactions. For such systems, the work in Step 3 is calculated by making the potential energy U of the system dependent on the coupling parameter λ. $U(\lambda = 0)$ is the potential energy of the separate crystal and melt systems at the end of Steps 1and 2, while $U(\lambda = 1)$ is the total potential energy of the crystal and melt systems interacting with each other across the cleaving planes. The work required to perform Step 3 is calculated using thermodynamic integration over λ by employing the following equation:

$$w_3 = \int_0^1 \langle \frac{\partial \mathrm{U}}{\partial \lambda} \rangle \, dz \tag{3.11}$$

3.4.2. Pressure tensors calculation

From the mechanical point of view, interfacial tension is determined from the diagonal elements of the pressure tensor. Fundamentally, pressure arises as a consequence of the flux of momentum, a physical mechanism that can be decomposed into different ways in which this flux takes place. There is a flux due to the momentum transported by the molecules, and there is another flux due to elastic collision between molecules [85]. In this way, the Clausius virial theorem takes into account both mechanisms. Collision between particles is due to the intermolecular forces acting between molecules, so the average of the virial $r \cdot F$ gives the non-ideal contribution to the pressure. The analysis of

the flux of momentum can be done for homogeneous and inhomogeneous phases. In inhomogeneous systems, the diagonal elements of the pressure tensor calculated by volume-perturbation (VP) method are not equal, and the interfacial tension is obtained due to this difference [86]. As mentioned, the mechanical method based on the Clausius virial theorem allows us to evaluate the pressure in a molecular simulation. Assuming a system with pairwise interactions in the absence of external fields, the usual virial form for pressure is:

$$p = \langle \rho k_B T \rangle + \langle \frac{1}{3V} \sum_i \sum_{i<j} r_{ij} \cdot f_{ij} \rangle \tag{3.12}$$

Where the angular brackets indicate the statistical average in the appropriate ensemble, $\rho = N/V$ is the number density, k_B is the Boltzmann constant, T is the temperature, r_{ij} is the intermolecular vector between a molecular pair, and f_{ij} is the corresponding intermolecular force, respectively.

To calculate the interfacial tension using the pressure tensors, the volume perturbation method can be applied with relevant anisotropic volume changes to calculate the pressure tensor, p_{ij}, where $i, j = x, y, z$. For a fluid in hydrostatic conditions, all the non-diagonal elements are null and the pressure p is given by one third of the trace of p_{ij}, i.e., $p = (p_{xx}+p_{yy}+p_{zz})/3$. Accordingly, pressure tensor can be used to calculate the surface tension γ for systems with interfaces. Assuming a planar interface lying in the x-y plane, the components of the pressure tensor depend on the distance z to the interface,

$$\gamma = \int_{-\infty}^{\infty} dz \, [p_N(z) - p_T(z)] \tag{3.13}$$

Where $p_N(z)$ is the local pressure normal to the surface, $p_N(z) = p_{zz}(z)$, and $p_T(z)$ is the local pressure tangential to the surface, defined by $p_T(z) = (p_{xx}(z) + p_{yy}(z))/2$. Since it is considered that an interface is isotropic in the x and y directions, $p_{xx}(z) = p_{yy}(z)$. For planar interfaces, the mean value theorem allows to write the last expression in terms of the macroscopic normal and tangential components, P_N and P_T [87]:

$$\gamma = \frac{1}{2} L_z \left[p_N - p_T\right] \tag{3.14}$$

In the equation, the factor 2 is applied considering the two interfaces of the simulated system.

3.4.3. Interface fluctuation method

The fluctuation method examines the magnitude of capillary fluctuations in the profile of a thin strip of the interface by employing the spectrum of interfacial fluctuations to calculate the interfacial stiffness, from which interfacial tension γ can be indirectly calculated. If the liquid-solid interfacial free energy were isotropic, then the fluctuations in interface position would be governed entirely by the magnitude of γ directly. However, in a usual case of anisotropic γ, the fluctuation spectrum depends not only on the magnitude of γ but also on the energy required for local orientation fluctuations. Therefore, the fluctuations depend on the interface stiffness γ + γ". The quantity of γ" (i.e., second derivatives) is defined as $\gamma'' = d^2\gamma/d\theta^2$, where θ is the angle between the instantaneous interface normal and the y axis depicted in Fig. 3.8. Using capillary wave theory, the interfacial stiffness can be related to $A(q)$, the Fourier transform of the interface height [88]:

$$\langle |A(q)|^2 \rangle = \frac{k_B T}{bW(\gamma + \gamma^{"})q^2} \tag{3.15}$$

Where bW is the area of the flat interface and q is the wave number, respectively. Accordingly, the interfacial stiffness $\gamma + \gamma^{"}$ is determined from the intercept of logarithmic plot of $\langle |A(q)|^2 \rangle$ versus q. Once $\gamma + \gamma^{"}$has been measured for several interfacial orientations, the value of γ in each orientation is obtained indirectly by constructing a functional form for the dependence of γ on orientation and fitting $\gamma + \gamma^{"}$ to obtain the best fits for the parameters of the functional form.

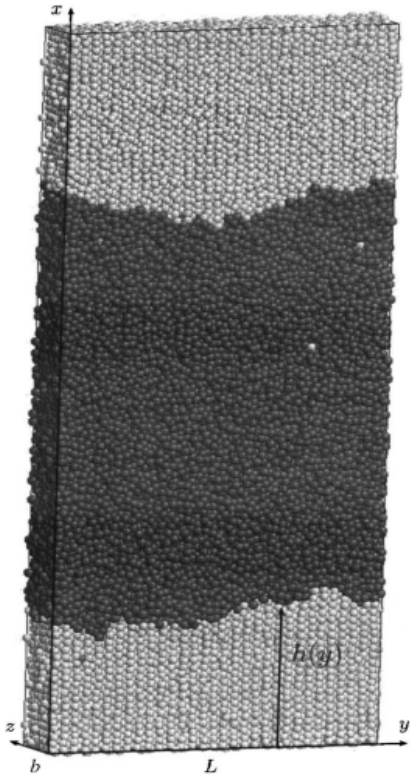

Fig. 3.8 Snapshot of simulation box for determining the interfacial free energy of liquid (dark gray)-solid (light gray) employing the fluctuation method in a hard-sphere system [89].

The studied interface is constructed as quasi-one-dimensional. Accordingly, a slab geometry is used with a simulation box that is of length *W* along the *x* axis, of length *L*

($L>W$) along the y axis (normal to the interfacial plane), and of thickness b ($b \ll W$) along the z axis. To ensure a quasi-one-dimensional interface, the value of b is small -typically about 3-4 lattice spacing. Additionally, the height of the interface $h(x)$ can be defined as the position of the boundary (interface) separating the solid and fluid phases[$h(x) = \sum_q A(q)\exp(iqx)$].

3.4.4. Sessile drop method

This method is employed in the cases that calculation of the contact angle between the two solid-liquid phases is favored instead of their interfacial tension energy. The equilibrated contact angle is determined according to the projection of the time averaged density profile of the drop located on the surface. The droplets simulated by MD studies can be constructed spherical [90], cubic [91], or cylindrical [92] based on the different approaches employed to analyze the droplet density profile. As a common procedure, the droplet is initially located above the surface and spontaneous wetting occurs during a relaxation time (varies from several hundred pico seconds to several nano seconds) by applying the canonical (NVT) ensemble. The wetting process includes three steps as illustrated in Fig. 3.9.

In the first stage, liquid molecules on the droplet surface adjacent to the solid surface escape from the droplet and get trapped by the solid surface due to the random thermal motion. Their vacancy sites left on the droplet are filled by the neighboring liquid molecules to reserve the minimal surface area. Accordingly, liquid molecules keep migrating from the droplet to the solid surface, and the liquid droplet deforms from its original shape to an irregular shape.

When significant interfacial area is formed on the solid surface, the wetting procedure enters the second stage. In this stage, liquid molecules above the contact line move from the droplet to the model surface. It results in propelling the contact line between the surface and the droplet and spreading the droplet on the surface. These two steps can be distinguished based on the change of the droplet height which is not obvious in the first stage.

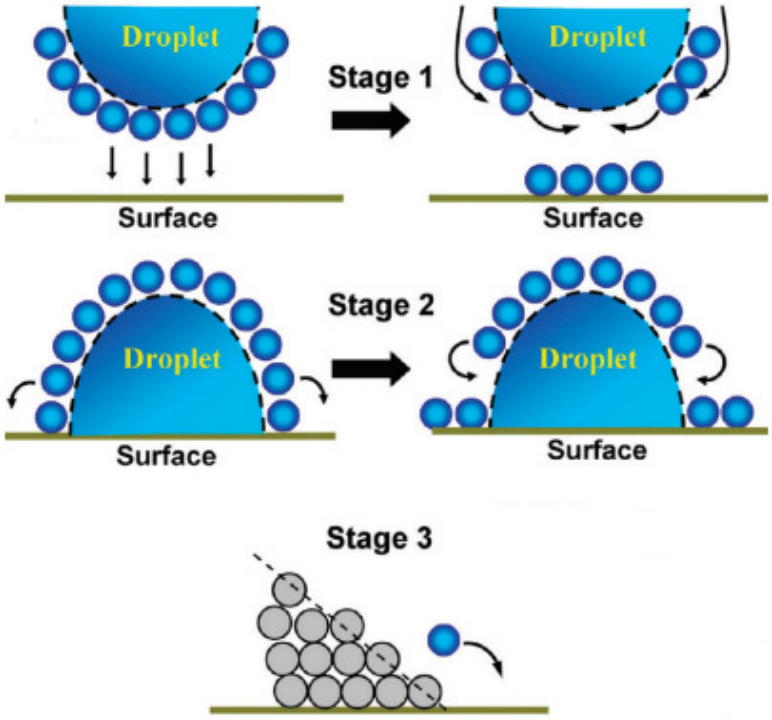

Fig. 3.9 Three stages of the wetting process of a liquid droplet on a solid surface considered to determine the contact angle during MD simulation [93].

In the third stage, equilibrium is established where the spreading of the liquid droplet stops while the exchange of liquid molecules between the surface and the droplet goes on near the contact line [94]. The calculation procedure of the contact angle begins with achieving the density distribution profiles by time average statics on the equilibrium

conformation of the adsorbed liquid droplets. Near the solid surface, large fluctuation occurs in the density profile because of the presence of the substrate. The density profile from the bulk liquid region across the liquid–solid interface is usually obtained by the following hyperbolic tangent function [95]:

$$\rho(z) = \frac{1}{2}(\rho^l + \rho^s) - \frac{1}{2}(\rho^l - \rho^s)\tanh(\frac{2(z - z_e)}{d}) \quad (3.16)$$

Where ρ^l and ρ^s are the bulk liquid and solid densities, respectively; z_e is the height of the water droplet and d is the thickness of liquid-solid interface. These profiles are projected on the $x - z$ plane and $y - z$ plane. Contour maps were then generated from the density profiles and fitted by a circular shape to achieve the contact angles of θ_{xz} and θ_{yz} and the final contact angle θ is calculated from the average of these two terms.

As a comparative overview of the four MD methods commonly used to investigate the wetting properties, it would be figured out that thermodynamic integration can be processed to calculate the interfacial energies directly while determining the accurate location of cleaving walls along with the necessity of producing the lowest possible rate of perturbation make this method quite challenging. As the second direct method, calculating pressure tensors are carried out based on anisotropic volume changes of the two phases where the method is more reliable to calculate the surface energies at fluids interfaces. The fluctuation method examines the magnitude of capillary fluctuations in the profile of a thin strip of the interface by using the spectrum of interfacial fluctuations to calculate the interfacial stiffness, from which interfacial tension γ can be indirectly calculated. Sessile drop method is employed in the cases that calculation of the contact angle between the two

solid-liquid phases is favored instead of their interfacial tension energy. This method needs large simulation boxes and prolonged simulation times to equilibrate the systems.

By considering the applicability, advantages, and limitations of the mentioned methods, we developed a model as a combination of pressure tensor calculations to determine the electrolyte-vacuum surface tension and a thermodynamic-based method arises from the thermodynamic integration procedure to calculate γ values of electrolyte-anode/separator interfaces. The cleaving method has been modified in our study based on the Helmholtz free energy to eliminate the sensitivity of locating and removing cleaving walls.

4. Model Development

In this chapter, we will introduce the details of generic molecular dynamics (MD) computational simulation techniques to derive equilibrated electrolyte structures where the resulted atomic trajectories can be used to examine electrochemical and wetting properties in LIB cells. We then explain the MD computation methodologies and the procedures developed to calculate electrolyte-anode interfacial tension energies in our current work.

4.1. Molecular Dynamics Computations

There are generally two main families of molecular dynamics (MD) methods, which can be distinguished according to the model (and the resulting mathematical formalism) chosen to represent a physical system. In the classical mechanics approach of MD simulations, molecules are treated as classical objects resembling the "ball and stick" model. Atoms are routinely represented by soft balls and bonds are represented by elastic sticks, and the laws of classical mechanics define the dynamics of the system. The quantum or first-principles MD simulations are the second category which started in the 1980's with the seminal work of Car and Parinello and explicitly consider the quantum nature of the chemical bond [96]. The electron density functional for the valence electrons that

determine bonding in the system is computed using quantum equations, whereas the dynamics of ions (nuclei with their inner electrons) is followed classically.

4.1.1. Molecular dynamics algorithm

A working definition of MD simulation is technique by which one generates the atomic trajectories of a system of *N* particles by numerical integration of Newton's equations of motion, for a specific interatomic potential with certain initial condition (IC) and boundary condition (BC). In MD simulations, the time evolution of a set of interacting particles is followed via the solution of Newton's equations of motion by integrating the set of their coupled differential equations given by:

$$m_i \frac{dv_i}{dt} = \sum_i F_2\left(r_i, r_j\right) + \sum_j \sum_k F_3(r_i, r_j, r_k) + \cdots$$

$$\frac{dr_i}{dt} = v_i \tag{4.1}$$

Where $r_i(t) = (x_i(t), y_i(t), z_i(t))$ is the position vector of *i*-th particle, and m_i is the mass of the particle, respectively. "Particles" usually correspond to atoms although they may represent any distinct entities (e.g., specific chemical groups) that can be conveniently described in terms of a certain interaction law. F_i is the force acting upon *i*-th particle at time *t*, where F_2 is a force function describing pairwise interactions between the particles, F_3describes three-body interactions, and many-body interactions can be added [97].

Fig. 4.1 illustrates the typical algorithm that an MD simulation is constructed.

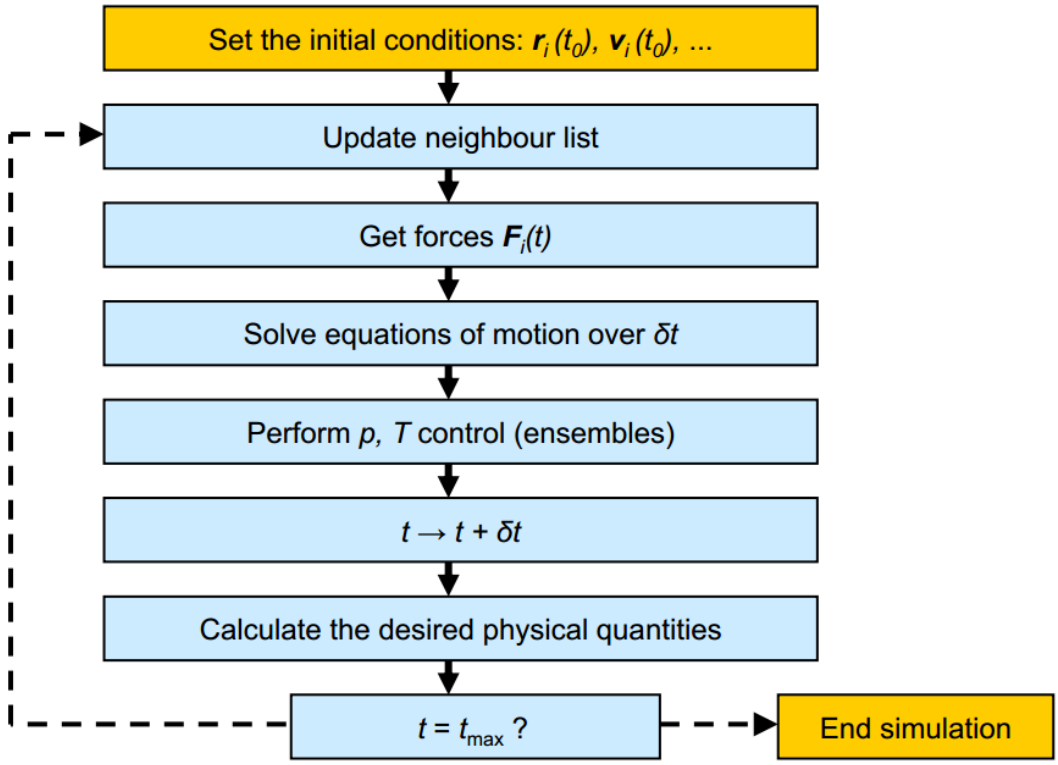

Fig. 4.1 The general algorithm applied to run molecular dynamics simulations.

In an MD simulation, it is first required to select a model system consisting of N particles and specify the conditions of the run (e.g., initial temperature, number of particles, density, and time step). Then, the boundary conditions (BC) should be considered and the system has to be initialized by assigning the initial positions and velocities of the particles. As the next steps, the forces are calculated on all the particles and Newton's equations of motions are integrated to obtain the particles trajectories. These two steps are the core of the simulation and are repeated until the system is equilibrated and its properties are no longer changed with the time. Finally, the actual measurements of the desired properties are calculated after the equilibration. The velocities themselves are not used to solve Newton's equations of motions. Rather, the positions of all particles at the present and

previous time step, combines with the knowledge of the force acting on the particles are employed to predict the positions at the next time step.

4.1.2. Boundary conditions (BCs)

There are two major types of BCs: isolated boundary condition (IBC) and periodic boundary condition (PBC). IBC is ideally suited for studying clusters and molecules, while PBC is suited for studying bulk liquids and solids. There could also be mixed BC such as slab or wire configurations for which the system is assumed to be periodic in some directions but not in the others. In IBC, the *N*-particle system is surrounded by vacuum; these particles interact among themselves, but are presumed to be so far away from everything else in the universe that no interactions with the outside occur except responding to some well-defined "external forcing." In PBC, one explicitly keeps track of the motion of *N* particles in the so-called supercell, but the supercell is surrounded by infinitely replicated, periodic images of itself. Therefore, a particle may interact not only with particles in the same supercell but also with particles in adjacent image supercells as depicted in Fig. 4.2. As pointed out before, PBC is intended to simulate the bulk environment effectively. During a simulation, particularly of a fluid, objects such as atoms and molecules will tend to move out of the unit cell, but the application of PBC means that an image object will always move into the unit cell to take its place. This is important as it allows the object in question to maintain a continuous trajectory while still experiencing the same potential energy field if it remained in the primary cell, allowing the calculation of quantities such as diffusion coefficients [98].

The trajectories of only the atoms in the center cell called the supercell (defined by edge vectors h_1 and h_2 of Fig. 4.2) are explicitly tracked, which is infinitely replicated in

all three directions (image supercells). The cut-off distance of the interatomic potential r_c determines the distance beyond which interaction may be safely ignored. Minimum image convention and explicit image convention are the methods that apply PBC to the simulations [99].

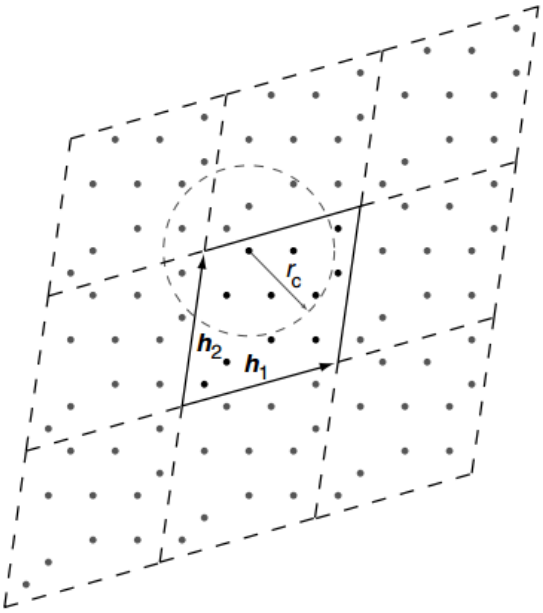

Fig. 4.2 Illustration of periodic boundary condition (PBC) [99].

If molecules in the interior cell are allowed to interact only with the molecule or molecular image closest to it, this is called a minimum-image structure. Each molecule interacts only with those molecules and images within a distance of half the cell size. The advantage of this approach is its simplicity. On the other side, the important feature of explicit image convention approach is that it allows the interactions between objects that may be many cells apart.

4.1.3. Force fields

A crucial part of any MD simulation is the proper choice of force field. The purpose of a force field is to describe the potential energy surface of entire classes of molecules with reasonable accuracy. Each atom in a structure that is to be modeled must be assigned a force field type. The force field type reflects the microchemical environment of the particular atom. By matching combinations of force field types, parameters for various potential energy terms can be assigned, ultimately leading to a full potential energy surface that can be used to calculate the forces between atoms. The force fields commonly used for describing molecules employ a combination of internal coordinates and terms, i.e., bonds, angles, and torsions to describe that part of the potential energy surface due to interactions between bonded atoms, and non-bond *terms* to represent the long-range Van der Waals and electrostatic interactions between atoms [100,101].

$$E_{total} = E_{valence} + E_{non-bond} \tag{4.2}$$

$$E_{valence} = E_{bond} + E_{angle} + E_{prop.\ torsion} + E_{improp.\ torsion} \tag{4.3}$$

$$E_{non-bond} = E_{vdW} + E_{coulomb} \tag{4.4}$$

When the atoms are covalently bonded to others, strong forces hold them together as stable chemical groups. Thus, $E_{valence}$ represents the bonded potential energies where E_{bond} is the bond stretching energy standing for the elastic interaction between a pair of atoms connected by a covalent bond, E_{angle} the angle-bending energy standing for the interaction among three covalently-bonded atoms that form a stable angle, and $E_{prop.\ torsion}$ and $E_{improp.\ torsion}$ the proper and improper torsional energies standing for the interactions among four covalently-bonded atoms that forma stable proper and improper dihedral angle as depicted in Fig. 4.3.

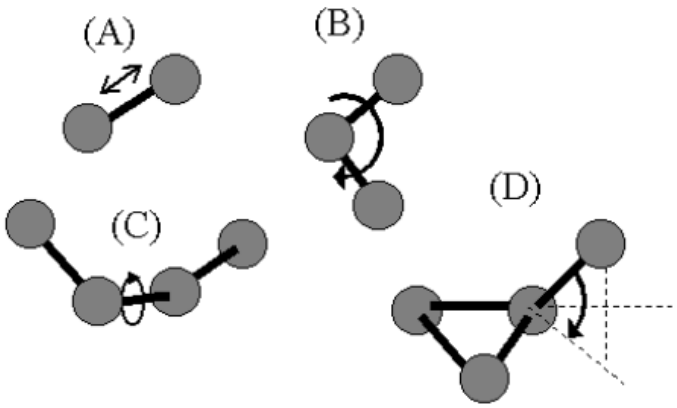

Fig. 4.3 A schematic illustration of the interactions that model covalent bonding: (A) Bond-stretching force; (B) Angle-bending force; (C) Proper torsional force; (D) Improper torsional force [101].

$$E_{bond} = \frac{1}{2} \sum_{m \in bonds} k_m^l \ (l_m - \ l_m^0)^2 \tag{4.5}$$

$$E_{angle} = \frac{1}{2} \sum_{m \in angles} k_m^\theta \ (\theta_m - \ \theta_m^0)^2 \tag{4.6}$$

$$E_{prop.\ torsion} = \frac{1}{2} \sum_{m \in torsions} V_m \left[1 + \cos(n_w \omega_m - \ \gamma_m)\right] \tag{4.7}$$

$$E_{improp.\ torsion} = \frac{1}{2} \sum_{m \in torsions} k_m^\xi \ (\xi_m - \ \xi_m^0)^2 \tag{4.8}$$

Where k_m^l is the bond strength, l_m is the distance between the two atoms of the m-th bond, l_m^0 is the equilibrium bond length, k_m^θ is the angle strength, $\theta_m$the m-th angle between the two adjacent bonds that share a common atom, θ_m^0 is the equilibrium bond angle, V_m is the amplitude of dihedral angles, n_w is the periodicity factor which determines the number of equilibrium dihedral angles in a 360º rotation, ω_m is the m-th dihedral angle

between the two adjacent angles that share a common bond, γ_m is the phase shift, k_m^{ξ} is the strength, ξ_m is the m-th improper dihedral angle among four atoms that are not bonded successively to one another, and ξ_m^0 is the equilibrium improper dihedral angle, respectively [100,101].

The non-bonded interactions of atoms encapsulate both van der Waals and electrostatic energies. The Lennard-Jones potential is the most applicable functional form that is incorporated in determining the total potential energy by introducing an attractive part representing the Van der Waals energy and a repulsive part representing the Pauli repulsion:

$$V_{LJ} = \frac{1}{2}\sum_{i,j,i\neq j} 4\varepsilon_{ij}\left[\left(\frac{\sigma_{ij}}{R_{ij}}\right)^{12} - \left(\frac{\sigma_{ij}}{R_{ij}}\right)^{6}\right] \tag{4.9}$$

Where ε_{ij} represents the van der Waals dissociation energy, σ_{ij} the collision diameter, and R_{ij} the distance between the i-th and j-th atom, respectively. The dissociation energy is equal to the amount of energy needed to pull a pair of atoms in the strongest van der Waals binding state apart. The collision diameter is approximately the distance at which a pair of atoms bounces off from each other in a normal, non-reacting condensed state. The Lennard-Jones potential basically depends on ε_{ij} and σ_{ij} as the basic energy-scale and length-scale parameters, respectively, and $V_{LJ}(r)$ has been plotted in Fig. 4.4 [100].

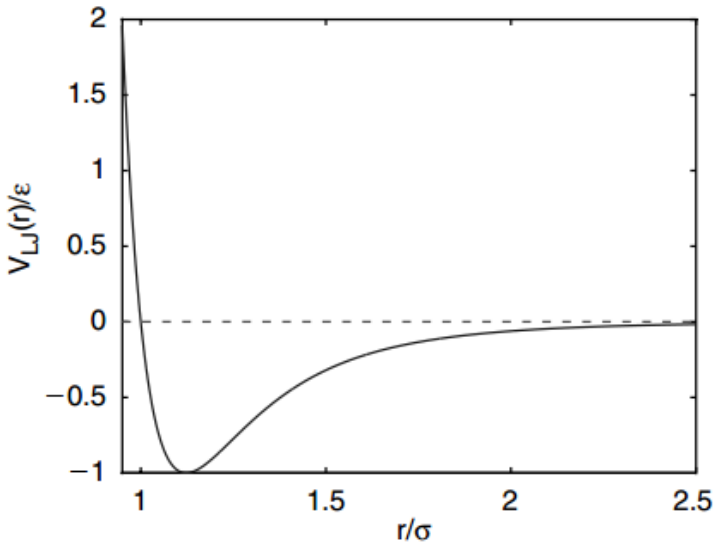

Fig. 4.4 The Lennard-Jones potential [102].

The other term that contributes in determining the non-bonded potential energies is the electrostatic potential energy according to the Coulomb's Law:

$$E_{coulomb} = \frac{1}{2}\sum_{i,j,i\neq j}\frac{q_i q_j}{R_{ij}} \tag{4.10}$$

Where $q_i$is the charge of the *i*-th atom. Compared with the Van der Waals potential, the electrostatic potential is a stronger and characterized by a more long-range interaction [103]. In MD simulations, the Van der Waals and electrostatic interactions as the non-bonded interactions are typically considered as important to be considered since it is the non-bonded interactions among the atoms of a macromolecule that affect its secondary structure and also these interactions among the atoms of different molecules organize them into crystals, complexes, and other assemblies.

There are several methods to determine the non-bonded potential energies as following:

- Atom-based
- Group-based
- Ewald
- PPPM (particle-particle particle-mesh method)

In the following sub-sections, atom-based method and Ewald summation method are briefly explained due to their applicability in this study.

4.1.3.1. Atom-based cutoffs

A simple approach to the calculation of long-range non-bond interactions is the direct method, where non-bond interactions are simply calculated to a cutoff distance and interactions beyond this distance are ignored. However, the direct method can lead to discontinuities in the energy and its derivatives. As an atom pair distance moves in and out of the cutoff range between calculation steps, the energy jumps, since the non-bond energy for that atom pair is included in one step and excluded from the next. To avoid the discontinuities caused by direct cutoffs, most simulations use a switching function $S(r)$ to smoothly turn off non-bond interactions over a range of distances. Fig.4.5 shows the features that a switching function must have:

- It must be unity for small non-bond distances where the greatest changes in the potential occur.
- At intermediate non-bond distances, it must smoothly tend to zero.
- It must be zero for large distances.

An effective potential is created by multiplying the actual potential by the smoothing function. Clearly the choice of the function in the intermediate range is crucial

and should be continuously differentiable in this region so that forces can be calculated. One possible choice for this function is to use a spline. Spline width specifies the size of the region within which non-bond interactions are to be splined from their full value to zero when the cubic spline truncation method is used for atom-based and group-based summations. A spline width of zero switches off spline interpolation and is equivalent to a direct cutoff. The range over which the *S(r)* tends to zero is also important. As indicated in Fig.4.5, the upper limit, i.e., large non-bond distance for this range is the cutoff distance. The location of the lower limit is variable and often requires some investigation.

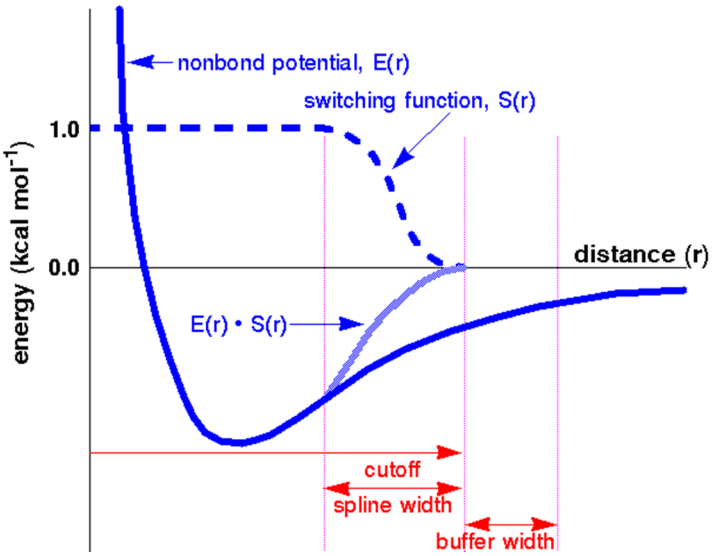

Fig. 4.5 Application of a switching function; energy=E(r) • S(r). Thick dark curve: the unmodified Van der Waals potential; dashed curve: the switching function S(r); gray curve: the resulting switched potential [104].

Additionally, the buffer width is the size of the buffer that is to be used when creating the non-bond neighbor lists. When any interaction pair moves more than half this distance, the neighbor list (if used) is recreated. This does not affect any values calculated, but does affect the computation time [104].

4.1.3.2. Ewald summation method

The Ewald technique is a method for computation of non-bonded energies in periodic systems, particularly electrostatic energies. Crystalline solids are the most appropriate candidates for Ewald summation, partly because the error associated with using cutoff methods is much greater in an infinite lattice. However, the technique can also be applied to amorphous solids and solutions. Since electrostatic energies consist of both short- and long-range interactions, it is maximally efficient to decompose the interaction potential into a short-range component summed in real space and a long-range component summed in Fourier space. Ewald summation rewrites the interaction potential as the sum of two terms:

$$\varphi(r) = \varphi_{sr}(r) + \varphi_{lr}(r) \tag{4.11}$$

Where $\varphi_{sr}(r)$ represents the short-range term whose sum quickly converges in real space and $\varphi_{lr}(r)$ represents the long-range term whose sum quickly converges in Fourier space. The long-ranged part should be finite for all arguments (most notably r = 0) but may have any convenient mathematical form, most typically a Gaussian distribution. The method assumes that the short-range part can be summed easily; hence, the problem becomes the summation of the long-range term. The long-range interaction energy is the sum of interaction energies between the charges of a central unit cell and all the charges of the lattice. Due to the use of the Fourier sum, the method implicitly assumes that the system under study is infinitely periodic (a sensible assumption for the interiors of crystals). One repeating unit of this hypothetical periodic system is called a unit cell. One such cell is chosen as the "central cell" for reference and the remaining cells are called images. The

most common reason for lack of convergence in Ewald method is a poorly defined unit cell, which must be charge neutral to avoid infinite sums [105,106].

4.1.3.3. Force field types

The purpose of a force field is to describe the potential energy surface of entire classes of molecules with reasonable accuracy. The force field extrapolates a larger set of related models from the empirical data of the small set of models used to parameterize it. Some force fields are employed due to their high accuracy for a limited set of elements, thus enabling good predictions of many molecular properties. Others are used for the broadest possible coverage of the periodic table, with necessarily lower accuracy. A force field type has to be assigned for each of the atoms in a modeled. As the name suggests, the force field type gives an indication of the nature and properties of a given particle in a simulation. If the simulation is atomistic then the principal determinant of the force field type is the element to which the atom belongs. The force field type also gives an indication of the nature of the local microchemical environment of a given atom (or, more generally, particle). A number of properties can be used to define a force field type where definition may include a combination of the following properties:

- Element (if particle is an atom)
- Type of bonds (for example single, double, resonant, etc.)
- Number of other particles to which the given particle is bonded
- The type of particles to which the given particle is bonded
- Hybridization
- Formal Charge

It should be considered that the particle properties that can change as a result of simulation such as particle coordinates, velocities, or actual charge are not used to define force field types (formal charge is usually fixed during a simulation and it can be used as one of the factors to define a force field type).

There have been a number of consistent force fields such as CFF91, pcff, CFF and COMPASS that were employed to consider the potential energies for different materials [107]. These force fields are parameterized against a wide range of experimental observables for organic compounds containing H, C, N, O, S, P, halogen atoms and ions, alkali metal cations, and several biochemically important divalent metal cations. We will provide more details about COMPASS force field since it was used to describe the potential energies in our studied systems.

COMPASS (new version of pcff) is an ab initio force field, of which parameterization procedure can be divided into the two phases of ab initio parameterization and empirical optimization [108]. In the first phase, the parameterization is focused on partial charges and valence parameters. The atomic partial charges were derived using ab initio electrostatic potentials. In the second phase, emphasis is on optimizing the force field to yield good agreement with experimental data. A few critical valence parameters are adjusted based on the gas phase experimental data. More importantly, the Van der Waals parameters are optimized to fit the condensed-phase properties. For covalent molecular systems, this refinement is achieved based on molecular dynamics simulations of liquids.

The COMPASS force field has broad coverage in covalent molecules including most common organics, small inorganic molecules, and polymers. For these molecular

systems, the COMPASS force field has been parameterized to predict various properties for molecules in isolation and condensed phases. The properties include molecular structures, vibrational frequencies, conformation energies, dipole moments, liquid structures, crystal structures, equations of state, and cohesive energy densities. The COMPASS development has extended the coverage to include inorganic materials. Consequently, the combination of these parameters makes the study of interfacial and mixed systems possible for organic and inorganic materials [107].

4.1.4. Numerical integration of the equations of motion

The idea of the numerical integration of Newton's equations of motion is to find an expression that defines positions $r(t + \Delta t)$ at time $t + \Delta t$ in terms of the already known positions at time *t.* Because of its simplicity and stability, the velocity Verlet algorithm is commonly used in MD simulations. The basic formula of this algorithm can be derived from the Taylor expansions for the positions $\mathbf{r}_i(t)$:

$$r(t + \Delta t) = r(t) + \Delta t.\boldsymbol{v}(t) + \frac{\Delta t^2 \boldsymbol{a}(t)}{2} \tag{4.12}$$

$$\boldsymbol{v}(t + \Delta t) = \boldsymbol{v}(t) + \frac{1}{2}\Delta t[\boldsymbol{a}(t) + \boldsymbol{a}(t + \Delta t) \tag{4.13}$$

$$\boldsymbol{a}(t + \Delta t) = \frac{\boldsymbol{F}(t + \Delta t)}{m} \tag{4.14}$$

Where $r(t)$, $\boldsymbol{v}(t)$, $a(t)$, and $F(t)$ are the position, velocity, acceleration, and force pertinent to the particle with mass *m* at time *t*, respectively [109].

It is noteworthy to mention that the exact trajectories correspond to the limit of an infinitesimally small integration step. It is however desirable to use possibly large time steps to sample longer trajectories. In practice, Δt is determined by fast motions in the

system. Bonds involving light atoms (e.g., *O-H* bond) vibrate with periods of several femtoseconds, implying that Δt should be on a sub-femtosecond scale to ensure stability of the integration.

4.1.5. Thermodynamic ensembles

Simple integration of Newton's equations of motion allows us to explore the dynamical properties of a system which is isolated from changes in number of moles N, in various environments as the combinations of conserved volume V, temperature T, pressure P, and enthalpy H. Therefore, various ensembles are created to provide the desired conditions as the constant-volume, constant-energy NVE ensemble, canonical ensemble NVT, isothermal- isobaric ensemble NPT, and isoenthalpic-isobaric ensemble NPH.

Generally, NVT ensemble is employed to study a system which is capable of transporting heat with an infinity heat source, and it is an appropriate choice for the systems with PBC. The energy of endothermic and exothermic processes is controlled with a thermostat. The NPT ensemble is always chosen in the cases when the correct pressure, volume, and density are very important in the simulations. This ensemble can be applied in systems with PBC and the temperature and pressure are controlled by an appropriate thermostat and barostat, respectively. The barostat maintains constant pressure by varying the cell parameters [110,111].

4.1.6. Thermostats

Temperature is a state variable that specifies the thermodynamic state of the system that is an important concept in MD simulations. This macroscopic quantity is related to the

microscopic description of simulations through the kinetic energy which is calculated from the atomic velocities. The temperature and the distribution of atomic velocities in a system are related through the Maxwell-Boltzmann equation where the same relation can be used to define a temperature at a particular time *t*:

$$T_{instan} = \frac{2}{k_B N_f} K_{instan} \tag{4.15}$$

Where T_{instan} and k_B are the instantaneous temperature of the system at time *t* and the Boltzmann constant, respectively. N_f is the number of degrees of freedom. If all atoms move independently, N_f equals 3*N* because each atom has three velocity components, i.e., v_x, v_y, and v_z. K_{instan} is the total kinetic energy of the system at time *t* as following:

$$K_{instan} = \sum_{i=1}^{N} (\frac{1}{2} m_i v_{x,i}^2 + \frac{1}{2} m_i v_{y,i}^2 + \frac{1}{2} m_i v_{z,i}^2) \tag{4.16}$$

Although the initial velocities are generated so as to produce a Maxwell-Boltzmann distribution at the desired temperature, the distribution does not remain constant as the simulation continues. This is especially true when the system does not start at a minimum-energy configuration of the structure. During dynamics, kinetic and potential energy are modified, and the temperature changes as a consequence. To maintain the correct temperature, the computed velocities have to be adjusted appropriately. In addition to maintaining the desired temperature, the temperature-control mechanism must produce the correct statistical ensemble. This means that the probability of occurrence of a certain configuration obeys the laws of statistical mechanics.

The temperature-control methods or thermostats that are commonly employed in molecular dynamics simulations are considered as [112-114]:

- Andersen
- Berendsen
- Nosé
- Nosé-Hoover-Langevin (NHL)
- Direct velocity scaling

Andersen method is the thermostat which controls the temperature in this study and has two different versions. One version involves randomizing the velocities of all atoms at a predefined collision period while the other version involves choosing atom collision times from a Poisson distribution at each time step and changing their velocities according to the Boltzmann distribution. The first version was implemented in the current study. The collision period is proportional to $N^{2/3}$ where N is the number of atoms in the system.

4.1.7. Barostats

Similar to the temperature-control methods, the pressure (and stress) control mechanism must produce the correct statistical ensemble. The following batostats are used to control the pressure [115]:

- Andersen
- Berendsen
- Parrinello-Rahman
- Souza-Martins

The volume can change by employing the Berendsen and Andersen methods while there is no change in the shape of the simulation cell. Thus, only the pressure can be controlled through these barostats. However, the Parinello-Rahman method modifies both the volume and shape of the cell which results in controlling the stress in addition to the pressure. The Andersen method as the barostat employed in this study is useful for liquid simulations since the box can become quite elongated in the absence of restoring forces since the shape of the cell is not allowed to change. A constant shape also makes the dynamics analysis easier. However, this method is not very useful for studying materials under anisotropic stress or undergoing phase transitions, which involve changes in both cell lengths and cell angles (in these situations, the Parrinello-Rahman method should be used where available).

The basic idea is to treat the volume V of the cell as a dynamic variable in the system. The Lagrangian of the system is modified so that it contains a kinetic energy term mass Q_A and a potential term which is the potential derived from an external pressure P_0 acting on volume V of the system.

4.2. Molecular dynamics simulation methodology

Here, the details of MD methodology that we employed in this study are described to calculate the interfacial energies between liquid solvents and solid electrolytes/separators.

4.2.1. Interfacial tension calculation

MD simulations of investigating the wetting properties of carbonate-based electrolytes with graphite as the anode and the PE/PP separators were performed with the

most recent version of non-polarizable COMPASS force field by employing the FORCITE module implemented in Materials Studio 7.0 commercial package (Accelrys Inc).

Various systems incorporating diethyl carbonate (DEC), ethyl methyl carbonate (EMC), or propylene carbonate (PC) one-component electrolytes were constructed at temperatures 0 °C and 25 °C including different $LiPF_6$ concentrations. The Ewald summation method was employed to consider the electrostatic interactions and the Van der Waals interactions were monitored via the atom-based method with the cutoff distance of 12.5 Å. Additionally, velocity Verlet algorithm was used to determine the trajectories of the atoms. A five-layer graphene system was built as the anode component employing aromatic sp^2 hybridized carbon. Three-dimensional, periodic orthorhombic simulation cells were used to construct the electrolyte systems and the periodic conditions were retained during all the simulation processes. The dimensions of the electrolyte and graphite cells were separately reduced to yield estimated densities at the studied temperatures followed by NPT equilibration runs with a time step of 1 fs and total simulation time of 500 ps. Andersen's thermostat and barostat were employed to control the temperature and pressure with collision ratio of 1 as a factor by which the collision period should be multiplied. The maximum energy difference that was allowed between successive steps of each simulation was defined as 50000.0 kcal/mole and the atomic force and velocity data required for interfacial tension calculations was written to each frame of the trajectory file. After the accomplishment of dynamics simulations through NPT ensemble, geometry optimization was applied to the cells based on reducing the magnitude of calculated forces until they become smaller than defined convergence tolerances. This was done using an iterative process, in which the atomic coordinates, and possibly the cell parameters, were

adjusted until the total energy of the structure was minimized. Consequently, the optimized structure corresponded to a minimum value in the potential energy surface. Accordingly, the convergence threshold values for the maximum energy change and force were assigned as 0.001kcal/mol and 0.5 $kcal.mol^{-1}.Å^{-1}$, respectively. Also, maximum iterations were determined as 500 cycles of geometry optimization where the calculation stops even if the convergence criteria are not satisfied. It is noteworthy to mention that the NPT equilibration was applied in two steps (500 ps at 25 °C and 500 ps at 0 °C) for the systems studied at 0 °C to gradually decrease the temperature of the system and reach to a more confident equilibration.

Next, the electrolyte cells were separately merged with anode and separator cells to construct the systems required for the calculation of interfacial tension energies. Dynamics simulations were carried out to equilibrate the merged systems for 500 ps with the NVT ensemble at the studied temperatures employing Andersen's thermostat and the results were extracted by considering the last 250 ps of the simulation process. The electrolyte-vacuum surface tension was calculated for each system from the atomic trajectories by using the pressure tensors stored in each frame and the electrolyte-anode/separator interfacial tension was obtained subsequently via a thermodynamics-based developed formula which will be explained in the next chapter.

4.2.2. Salt aggregation

Three-dimensional, periodic cubic simulation cells were constructed with the approximate length of 45 Å, in which EMC, DEC, or PC solvents with 1 M $LiPF_6$ salt were incorporated each in a one-component system. The cells were equilibrated for 500 ps with

the NPT ensemble at 25 °C with a time step of 1 fs and the temperature and the pressure of each system controlled by the Andersen's barostat and thermostat. The coordination of salt ions was determined in each of the three cells to investigate the impact of solvents dielectric constant on clustering of the salt ions.

5. Results and Discussion

In this chapter, we will discuss the method developed to calculate the electrolyte - graphite anode and electrolyte – PE/PP separators interfacial tension energies based on the combination of both mechanical and thermodynamic approaches, and subsequently, the resulted structures are illustrated. The calculated interfacial energies were investigated according to the impact of solvent cyclicity, temperature, and salt concentration. Moreover, the clustering phenomena are monitored in different solvent systems containing 1 M $LiPF_6$.

5.1. Electrolyte – graphite anode interfacial tension energies

The interfacial tension values were obtained by considering the Clausius virial theorem based on the knowledge of pressure tensors to calculate the electrolyte-vacuum surface tension γ_{ev}. A thermodynamic-based method was employed according to the total change in Helmholtz free energy to calculate the electrolyte-solid interfacial tension γ_{es} particularly at the anode and the separator interfaces. Thus, γ_{ev} values were calculated via Eq. 3.14 as the results required to participate in the formula developed thermodynamically to calculate γ_{es}:

$$\gamma_{es}\,\Delta A = \Delta F = \Delta U_{ev-ee} + \Delta U_{sv-ss} + \Delta U_{ev-es} + \Delta U_{sv-es} - T(\Delta S_{ev-ee} + \Delta S_{sv-ss} + \Delta S_{ev-es} + \Delta S_{sv-es}) \quad (5.1)$$

Where the interfacial tension can be presented as the difference between the cohesion and adhesion free energies divided by the surface area of the created interface. ΔF is the total change in Helmholtz free energy, ΔU_{ev-ee} is the change of internal cohesion energy between the two electrolyte surfaces, i.e., the energy required for surface separation, and ΔU_{ev-es} is the energy of adhesion between electrolyte and anode or separator (solid phases) which is the energy required to bring each of the two phase surfaces close to each

other where the electrolyte surface was separated by vacuum, respectively. ΔS terms are defined as the entropies of the corresponding processes.

It is assumed that the total entropy change is mainly affected by the limitation of electrolyte conformation due to the creation of the interface in the electrolyte system. Therefore, since the solid surfaces stay intact and their deformation is negligible, their separation does not produce any substantial entropy changes. Therefore, $\Delta S_{sv-ss} + \Delta S_{ev-es} + \Delta S_{sv-es} \ll \Delta S_{ev-ee}$ and Eq. 5.1 can be reduced to:

$$\Delta F \approx \Delta U_{ev-ee} - T\Delta S_{ev-ee} + \Delta U_{sv-ss} + \Delta U_{ev-es} + \Delta U_{sv-es} \tag{5.2}$$

By considering the fact that at the conditions equivalent to the NVT ensemble, interfacial tension equals Gibbs free energy per surface area:

$$\Delta U_{ev-ee} - T\Delta S_{ev-ee} = \gamma_{ev} A \tag{5.3}$$

Thus, the electrolyte-anode interfacial energies finally were obtained as:

$$\begin{aligned} \gamma_{es} &= \gamma_{ev} + (1/A)(\Delta U_{sv-ss} + \Delta U_{ev-es} + \Delta U_{sv-es}) \\ &= \gamma_{ev} + (1/A)(\Delta U_{sv-ss} - 2 \times \Delta U_{es}) \end{aligned} \tag{5.4}$$

Where ΔU_{ss-sv} is the change of internal cohesion energy between the two solid surfaces which is the energy required for surface separation and ΔU_{es} represents the energy of separation of the electrolyte and the solid phase surfaces, respectively. The sum of the energies required to bring the electrolyte and anode or separator surfaces together where each are separated by vacuum equals to the negative sum of the energies should be employed to separate each phase from the other one. Since each phase has two surfaces

with PBC, the interfacial tension value relevant to one common surface was calculated via the following expression:

$$\gamma_{es} = [\,\gamma_{ev} + (1/A)(\Delta U_{sv-ss} - 2 \times \Delta U_{es})]/2 \quad (5.5)$$

5.1.1. Structures

Diethyl carbonate (DEC), ethyl methyl carbonate (EMC), and propylene carbonate (PC) were employed along with $LiPF_6$ as depicted in Fig. 5.1 to investigate the impacts of solvent cyclicity and salt concentration on the electrolyte – graphite/PE/PP interfacial tension at various temperatures. Accordingly, the studied systems mentioned in table 5.1 were constructed based on these three solvents at temperatures 0 °C and 25 °C to study electrolyte – anode wetting properties while EMC and PC solvents at T = 25 °C were chosen to calculate electrolyte – separators interfacial energies.

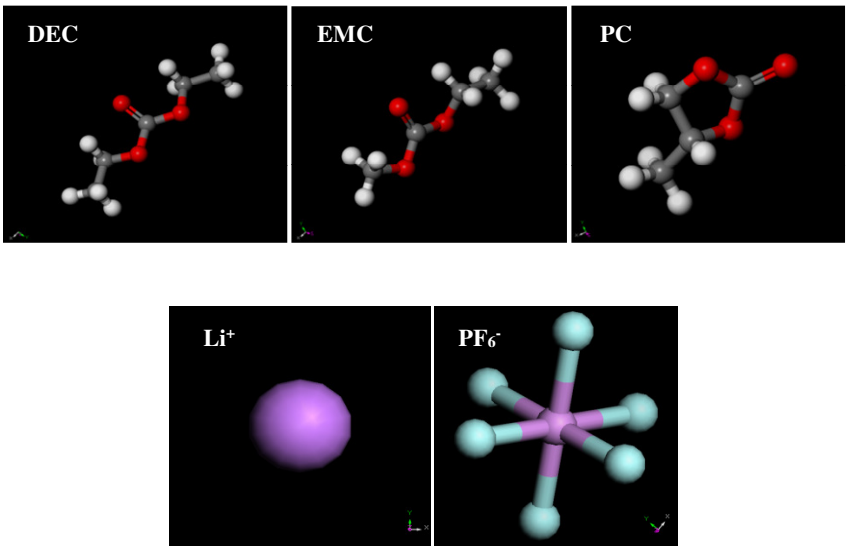

Fig. 5.1 The carbonate solvents and salt ions employed in the studied systems.

Table 5.1 The constructed systems at temperatures 0 °C and 25 °C.

Temperature (°C)	**Systems**							
0	DEC			EMC			PC	
25	DEC	DEC: 1 M $LiPF_6$	EMC	EMC: 0.752 M $LiPF_6$	EMC: 1 M $LiPF_6$	EMC: 1.254 M $LiPF_6$	PC	PC: 1 M $LiPF_6$

To check the appropriateness of COMPASS force field for our systems and to test the MD computation produces reliable results, NPT ensemble was employed to calculate their densities during 500 ps. The results obtained for EMC: 1 M $LiPF_6$ electrolyte as the representative system have been illustrated in Fig 5.2. The initial cell density was considered as 1.106 g/cm^3 while the final calculated density was 1.118 g/cm^3. The small amount of difference between the initial and final density values in addition to the low fluctuations are consistent with the densities obtained for all other systems which validate the pertinence of using COMPASS force field for our calculations.

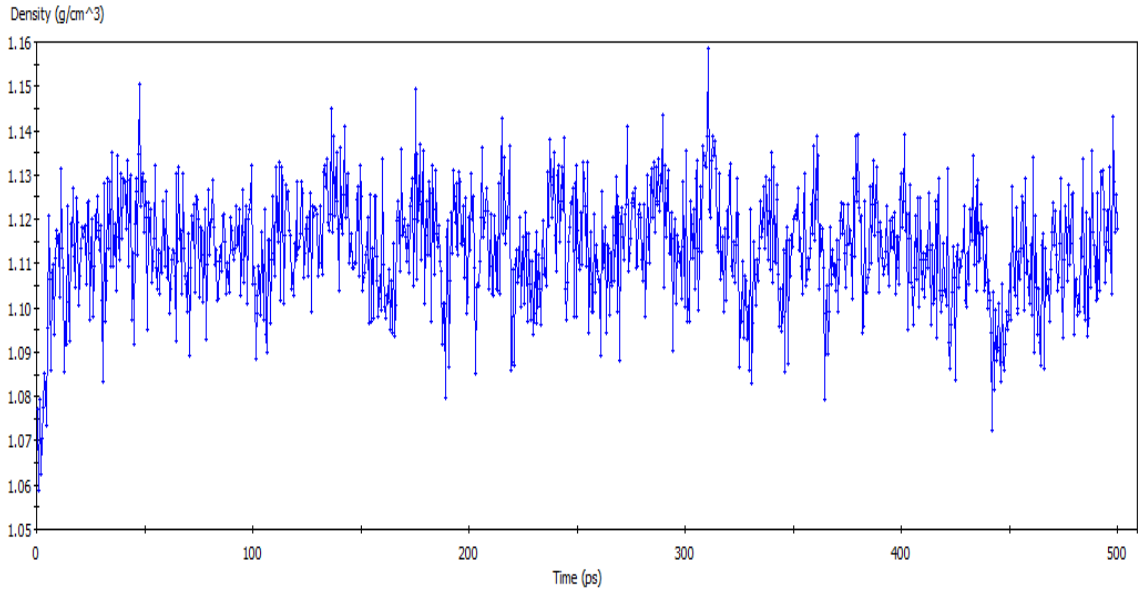

Fig. 5.2 Density profile of EMC: 1 M $LiPF_6$ electrolyte.

In accordance with Eq. 5.5, five independent structures must be built for each system to calculate the electrolyte-vacuum surface tension and determine the difference between cohesion and adhesion energies of the graphite/PE/PP and the electrolyte-graphite/PE/PP cells for the ultimate calculation of the interfacial tension energies between two phases. Additionally, five sets of simulations were run for each of the systems mentioned in Table 5.1. An instance of a system comprised of the mentioned five structures is illustrated in Fig. 5.3.

Fig. 5.3 (a) An electrolyte-vacuum structure employed to calculate γ_{ev} mechanically.

Fig. 5.3 (b) One of the two structures(U_{sv}) required to calculate the change in cohesion energy relevant to the separation of two anode surfaces(ΔU_{sv-ss}).

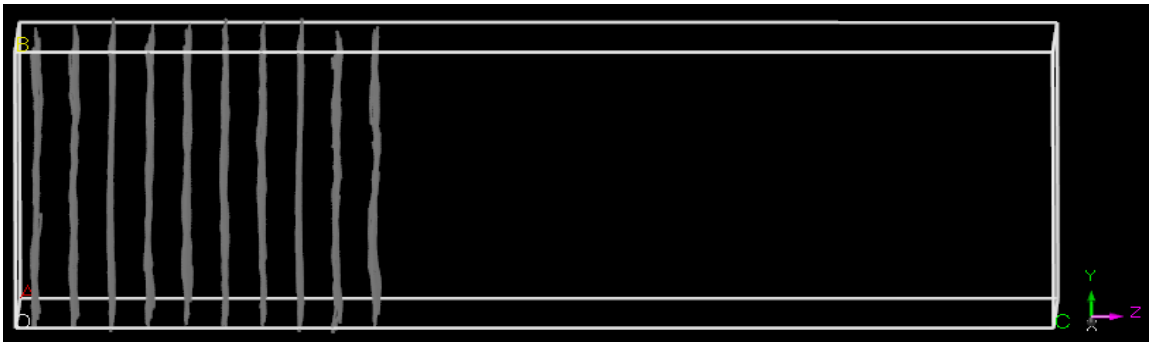

Fig. 5.3 (c) One of the two structures(U_{ss}) required to calculate the change in cohesion energy relevant to the separation of two anode surfaces(ΔU_{sv-ss}).

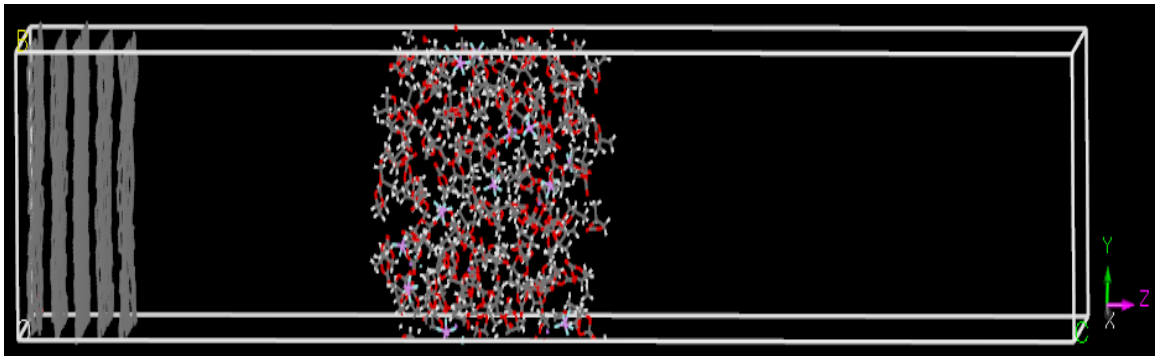

Fig.5.3 (d) The electrolyte and graphite layers were kept separated for calculation of ΔU_{es}. The dimensions of simulation box are 21.8 x 29.4 x 160.2 Å in average.

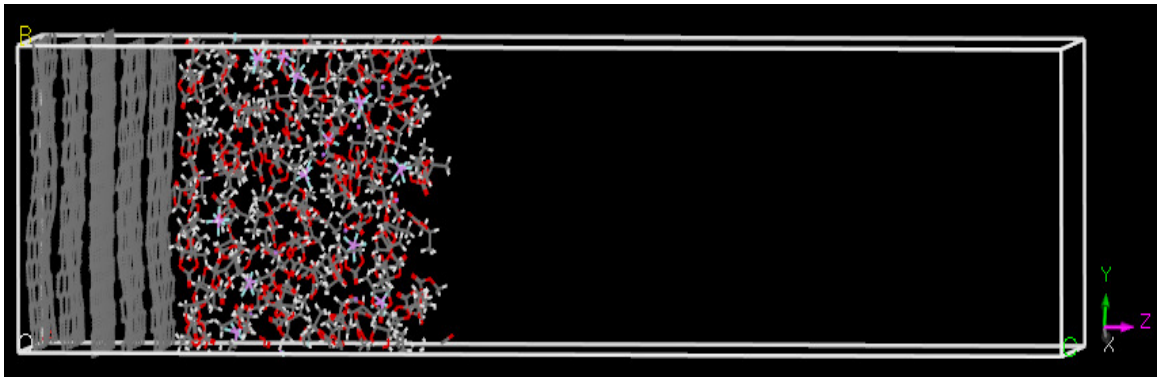

Fig. 5.3 (e) The electrolyte and graphite layers were placed in contact with each other for calculation of ΔU_{es}. The dimensions of simulation box are 21.8 x 29.4 x 125.2 Å in average.

Fig. 5.3 Five types of structures constructed for each system to calculate the electrolyte-anode interfacial tension energy. The vacuum thickness of structure (a) is 60 Å while the graphite and electrolyte surfaces were separated by 35Å and 70 Å distances in the other structures accordingly.

5.1.2. Impact of solvent cyclicity and temperature

The average values (based on five independent computations) of electrolyte-vacuum surface energies (γ_{ev}) and the electrolyte-anode interfacial tension (γ_{es}) obtained for the systems incorporate linear carbonate solvents as EMC and DEC in one-component solutions have been illustrated in Fig. 5.4 and 5.5, respectively. The systems were simulated at temperatures 0 °C and 25 °C along with 1 M $LiPF_6$ at T = 25 °C. Also, the numerical values of γ can be extracted from Table 5.2 for more precise comparison.

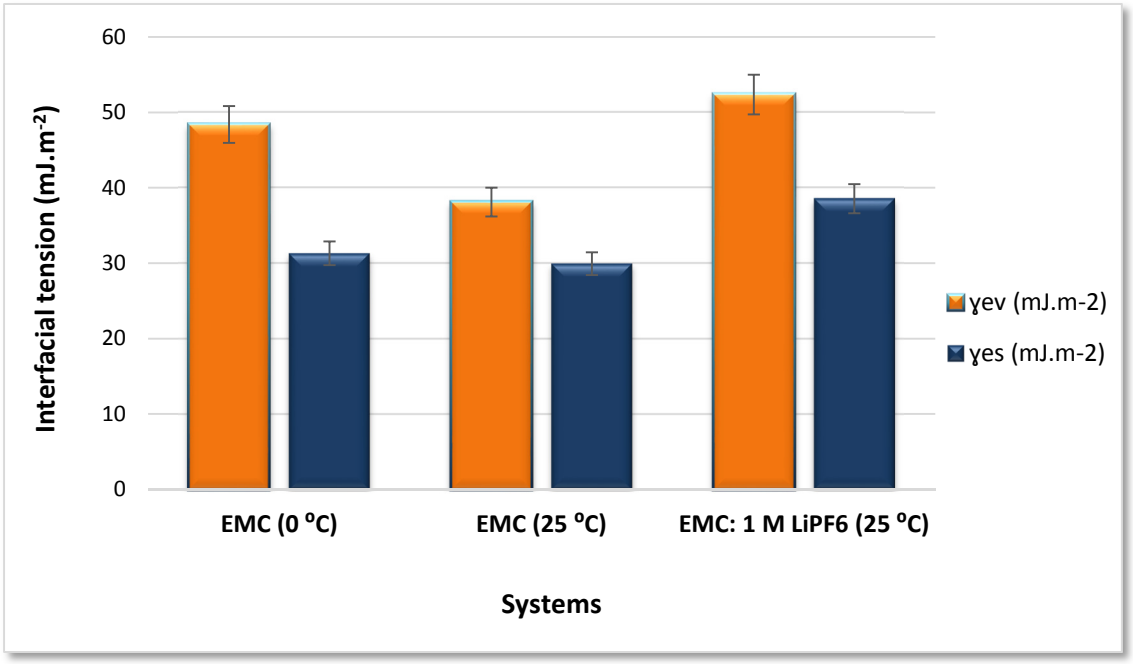

Fig. 5.4 γ_{ev} and γ_{es} values obtained for one-component EMC electrolyte at T = 0 °C solely and with/without 1 M $LiPF_6$ at T = 25 °C.

The electrolyte-vacuum surface energy is controlled by the difference value of the tangential and normal components of pressure at the interface according to the surface normal direction. As depicted in Fig. 5.3 and 5.4, γ_{ev} has the highest value at 0 °C while the force per unit length perpendicular to the local concentration gradient reaches its lowest values in systems without salt at 25 °C.

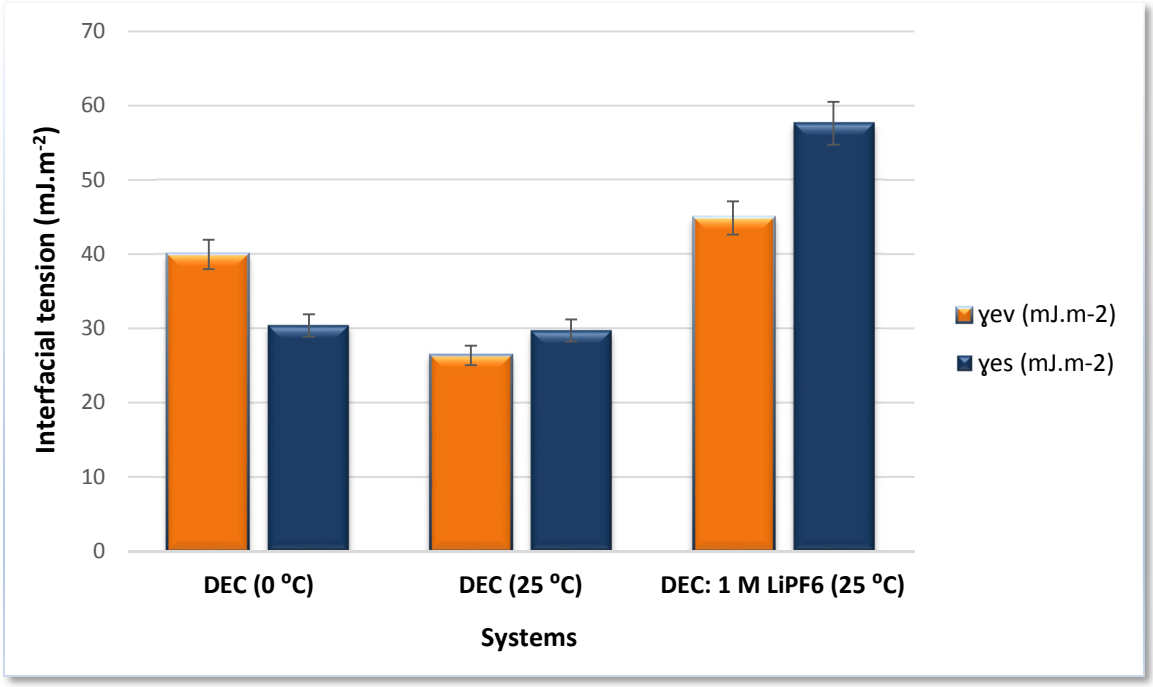

Fig. 5.5 γ_{ev} and γ_{es} values obtained for one-component DEC electrolyte at T = 0 °C solely and with/without 1 M $LiPF_6$ at T = 25 °C.

To clarify the dependency of pressure tensors to the temperature of a system, the temperature-dependent properties of the electrolyte, particularly viscosity, should be investigated by considering the rheological behavior of the carbonate-based solutions. According to the empirically-obtained Volger-Fulcher-Tamman (VFT) equation, viscosity of the electrolyte changes inversely with the temperature [116]:

$$\eta = \eta_0 \cdot \exp\left(\frac{B}{T - T_0}\right) \tag{5.6}$$

Where η_0 is the limiting viscosity at $T \to \infty$, B is a fitting parameter, and T_0 is the ideal glass transition temperature, respectively.

Table 5.2 γ_{ev} and γ_{es} values of the systems contain one-component linear carbonate electrolytes.

System	γ_{ev} (mJ.m^{-2})	γ_{es} (mJ.m^{-2})
EMC (0 °C)	48.4	31.33
EMC (25 °C)	38.1	29.94
EMC: 1 M $LiPF_6$ (25 °C)	52.36	38.57
DEC (0 °C)	39.93	30.37
DEC (25 °C)	26.36	29.69
DEC: 1 M $LiPF_6$ (25 °C)	44.85	57.6

Generally, the concept of viscosity is defined based on the friction of neighboring particles in a fluid that are moving at different velocities due to the relationship between the viscous stress applied to the fluid and the resulting strain rate. The Newtonian behavior of carbonate-based electrolytes certified by the experimental studies [117,118] draws our attention to discuss the rheological behavior of our electrolytes based on the linear relationship between the deformation of the solution and the corresponding stress as indicated in Eq. 5.7 [119]:

$$\eta = \frac{\tau}{\dot{\gamma}} \tag{5.7}$$

Where η is the Newtonian viscosity, and τ and $\dot{\gamma}$ are the viscous stress tensor and strain rate tensor, respectively. The viscous stress tensor is a tensor employed to model the part of the stress at a point within some material that can be attributed to the strain rate, the rate of change of deformation around that point. The strain rate tensor can be defined

as the derivative of the strain tensor with respect to the time, or as the symmetric component of the gradient of the flow velocity according to the position of the point.

According to the VFT equation and Eq. 5.7, the viscosity of the electrolyte is increased by decreasing the system temperature which results in higher values of viscous stress tensor. In Newtonian fluids the pressure tensor is given by the sum of the external pressure applied to the system p and the viscous stress tensor τ where I is the identity tensor [120].

$$P = \tau - pI \tag{5.8}$$

Since no external pressure applied to our systems, $pI = 0$ and $P = \tau$ as a result. Therefore, decreasing the temperature results in the increasing of the electrolyte viscosity and subsequently, the viscous stress tensor and the pressure tensor will be increased. The pressure tensor in Eq. 5.8 can be considered equivalent to ΔP in Eq. 3.14 as the difference between the tangential and normal pressure tensors applied to the electrolyte-vacuum interface in our systems. Therefore, the surface tension γ_{ev} changes consistently with ΔP values which increase by decreasing the temperature. The results illustrated in Fig. 5.4 and 5.5 validate the mentioned relationships for the systems with the same solvent. The viscosity of the mentioned systems was measured experimentally in courtesy of Dr. C.W. Lee (Kyung Hee University, South Korea) by employing viscometer SV-10. The obtained values shown in Table 5.3 confirm the dependency of γ_{ev} to the electrolyte viscosity.

Table 5.3 Experimental results of the viscosity of the studied systems contain linear carbonate solvents simulated in different conditions (Courtesy of C.W. Lee, Kyung Hee University).

Systems	Viscosity (cP)
EMC (0 °C)	0.77
EMC (25 °C)	0.50
EMC: 1 M $LiPF_6$ (25 °C)	1.52
DEC (0 °C)	0.99
DEC (25 °C)	0.59
DEC: 1 M $LiPF_6$ (25 °C)	1.75

The viscosity values shown in table 5.3 inversely change with temperature for each system containing the same solvent as it was expected according to the VFT equation. Moreover, the systems containing salt have a higher viscosity value in comparison to the similar systems without salt due to the lower mobility rate of the solvating molecules and the effect of drag forces that the solvated ions apply due to the possession of solvation sheath. As a consequence, the data provided in Tables 5.2 and 5.3 imply that the drag forces imposed by the presence of less mobile species in the electrolytes with salt affect the viscosity of electrolyte dominantly compared with the temperature change.

It should be noted that the dielectric constant value of each solvent has to be considered besides the impact of the electrolyte viscosity to make one able to compare the γ_{ev} values of the systems with different solvents. The surface tension between two bulk phases is identified as the cumulative effect of several factors each due to a specific type of intermolecular force across an interface, i.e., hydrogen bonds, electron acceptor-electron donor forces, etc. It is empirically believed that the values of surface tension depend on the

polarity of the electrolyte as the dominant factor [121,122]. When the dielectric constant of the solvent and in general, the polarity of the electrolyte with salt incorporated converges with the polarity of the other phase, the attraction between the two phases increases at the interface by decreasing the cohesive forces which results in lower interfacial tension values and better wetting properties. Thus, the higher polarity of the electrolyte results in the higher values of interfacial tension energies. Comparison of the results illustrated in Table 5.2 with the experimental values of viscosity mentioned in Table 5.3 affirms the dominancy of the electrolytes polarity effect compared with their viscosity. The values of dielectric constant for EMC and DEC are 2.96 and 2.80, respectively. Hence, although the viscosity of the systems contain DEC is higher than the equivalent systems contain EMC, the γ_{ev} values obtained for the EMC systems are higher due to its higher dielectric constant value.

In a nutshell, viscosity is the criterion that determines the electrolyte-vacuum surface tension in a system with constant solvent type. Viscosity is controlled by temperature change in systems without salt and dielectric constant of the solvent for the systems $LiPF_6$ is included. Dielectric constant of a solvent represents its ability to dissociate the salt ions where its lower values result in the salt aggregation phenomenon which creates the species with lower mobility and ultimately, a more viscous electrolyte. When solvated ions migrate within the electrolyte, the drag force applied by the surrounding solvent molecules is measured by the solvent viscosity. This is the reason of lower experimental viscosity value obtained for EMC: 1 M $LiPF_6$ (25 °C) system compared with DEC: 1 M $LiPF_6$ (25 °C) due to the higher ability of EMC to dissociate the salt ions which leads to lower amounts of salt clustering. However, based on the value reported, investigating the surface tension γ_{ev} for the systems with different solvent type is

dominantly monitored by the influence of the electrolyte polarity where all the surface tension values for the systems contain EMC are higher than equivalent systems of DEC. These results explicitly illustrate the interplay between viscosity and dielectric constant of the solvents in determination of surface tension values.

As pointed out before, wettability in electrodes/separators is principally monitored by the electrolyte penetration and spreading in the pores. Therefore, viscosity of the electrolyte is known as the driving force that controls the electrolyte penetration while the interfacial tension is the critical factor which manages the spreading of the electrolyte in to the pores. Considering the temperature and polarity of the electrolyte as the dominant factors that influence viscosity and interfacial tension, respectively; the electrolyte-electrode interfacial tension energy is higher for the systems contain salt compared with the sole solvent. Thus, solvent: 1 M $LiPF_6$ electrolytes show lower wettability in EMC and DEC systems due to their higher polarity compared to the relevant solutions in absence of salt ions. We found that the γ_{es} values of the systems contain EMC or DEC (i.e., linear solvents) do not change considerably with temperature. These results imply that the temperature change affects the polarity of the mentioned electrolytes negligibly which is in agreement with the results obtained by the limited available experimental studies [123].

The dependency of dielectric constant on temperature is different for linear and cyclic carbonate solvents. The origin for the effect of molecular cyclicity on the dielectric constant has been attributed to the intramolecular strain of the cyclic structures that favors the conformation of better alignment of molecular dipoles, while the more flexible and open structure of linear carbonates results in the mutual cancellation of these dipoles. Therefore, the dielectric constant of linear carbonates is not changed significantly with

temperature in general while the consistent variation of dielectric constant versus temperature in the case of cyclic carbonates affects their wetting properties.

From Figs. 5.4 and 5.5, as we expected, the interfacial tension values of the systems containing EMC solely at temperatures 0 °C and 25 °C are relatively higher than those of DEC due to the slightly higher dielectric constant of the EMC solvent. However, the average interfacial tension value obtained from the EMC: 1 M $LiPF_6$ system is interestingly lower than the DEC system containing 1 M $LiPF_6$. The energies required to separate the electrolyte and anode components of EMC: 1 M $LiPF_6$ and DEC: 1 M $LiPF_6$ systems in a cell are 153.82 x 10^{-23} kJ and 140 x 10^{-23} kJ, respectively. The higher energy of separation in the system contains EMC confirms the existence of stronger intermolecular attractions and affinity between two phases which subsequently affirms better wettability and lower interfacial tension energy. Fig. 5.6 illustrates the comparison between the energy of separation and γ_{es} values from EMC and DEC systems containing salt at $T = 25$ °C. Besides the linear carbonates, we investigated the wetting properties of cyclic PC in the similar conditions. The obtained results are illustrated in Fig.5.7 and Table 5.4. Again, these results are based on five independent MD computations.

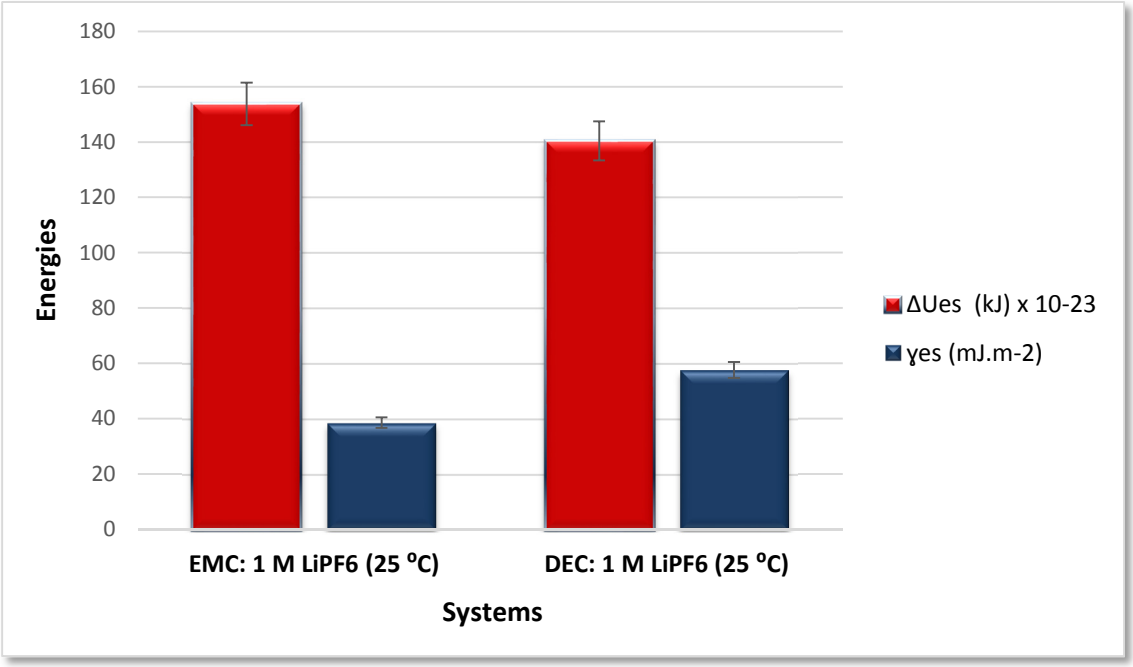

Fig. 5.6 ΔU_{es} and γ_{es} values of EMC: 1 M $LiPF_6$ and DEC: 1 M $LiPF_6$ systems.

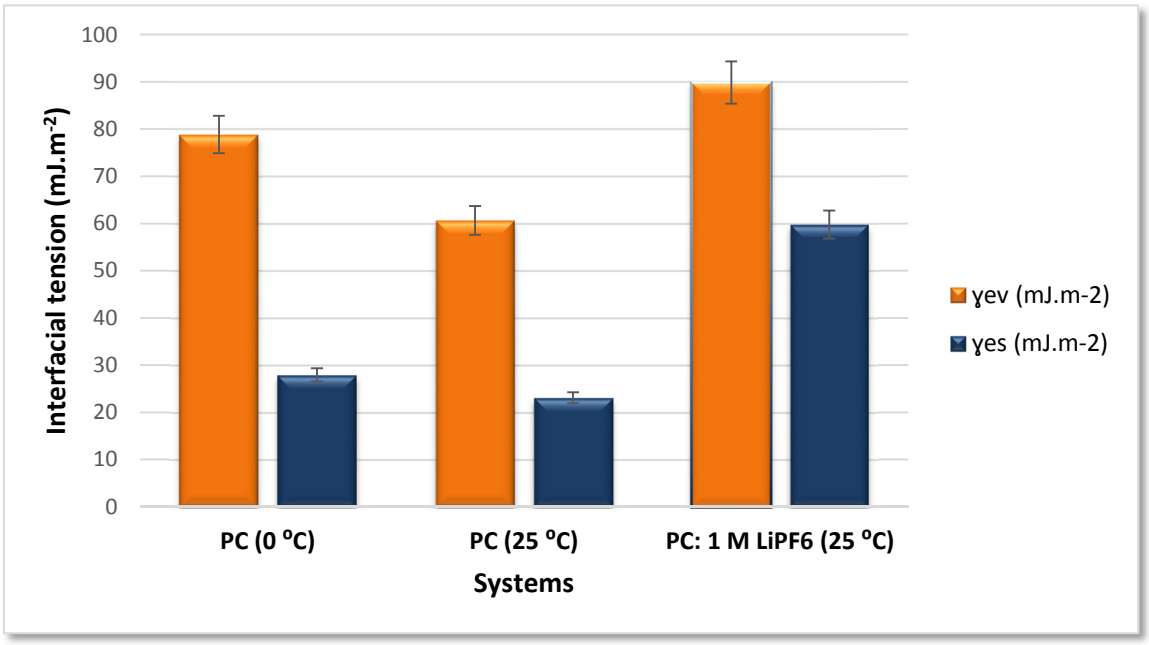

Fig. 5.7 γ_{ev} and γ_{es} values obtained for one-component PC electrolyte at T = 0 °C solely and with/without 1 M $LiPF_6$ at T = 25 °C.

Table 5.4 Surface tension and interfacial tension energies of the systems contain PC solvent simulated in different conditions.

System	γ_{ev} (mJ.m^{-2})	γ_{es} (mJ.m^{-2})
PC (0 °C)	78.83	27.91
PC (25 °C)	60.65	23.1
PC: 1 M $LiPF_6$ (25 °C)	89.86	59.74

Due to better alignment of molecular dipoles in cyclic carbonates, PC possesses higher dielectric constant (ε = 64.92) compared with the linear carbonate solvents. This property along with the high viscosity of PC (η = 2.53 cP) are considered as the reasons for the highest values of γ_{ev} and γ_{es} of PC: 1 M $LiPF_6$ at T = 25 °C in Fig. 5.6 and Table 5.4. In electrolytes that contain a solvent with a high dielectric constant value, salt ions would have a higher probability of staying free at a given salt concentration and ion aggregation would be less likely to occur. When solvated ions migrate within the electrolyte, the drag force applied by the surrounding solvent molecules is measured by solvent viscosity. Consequently, the migration of solvated ions is more difficult in an electrolyte contains a solvent of higher viscosity. Accordingly, the electrolyte-vacuum surface tension we calculated for the system of PC solvent associated with 1 M $LiPF_6$ at T = 25 °C has the highest value compared with the systems PC is incorporated solely. Additionally, the high value of PC dielectric constant resulted in higher γ_{es} obtained for the PC: 1 M $LiPF_6$ system.

The electrolyte-electrode interfacial tension calculated for PC electrolyte at T = 0 °C is higher than the same system simulated at T = 25 °C which is consistent with the

results we obtained for the linear carbonate electrolytes. However, the difference between γ_{es} (T = 0 °C) and γ_{es} (T = 25 °C) values are slightly higher than those of EMC and DEC solvents. This trend reflects the higher impact of temperature on variation of PC dielectric constant as a cyclic solvent based on the orientation of molecular dipoles.

The interfacial tension values from all of the three solvent categories are generally lower than their relevant surface energies. This phenomenon happens because the adhesive forces between electrolyte and graphite anode forming an interface are greater than the similar forces at the electrolyte-vacuum interface. The two systems contain DEC at temperature 25 °C behave inversely which reflect the dominancy of cohesive forces in each of the liquid and solid phases. The interfacial tension values calculated for the three studied systems have been illustrated in Fig. 5.8 by considering the constant simulation conditions where DEC and EMC solvents reveal close values of γ_{es} at temperatures 25 °C and 0 °C. However, there is higher affinity of the electrolyte system that contains DEC and the graphite anode due its lower dielectric constant at both temperatures which may result in higher wettability of the anode.

In addition, we interestingly found that the interfacial tension energies of the electrolytes incorporate sole PC solvent are lower than the equivalent systems containing linear solvents at each temperature despite its higher dielectric constant. Quantum chemistry studies ascribe this phenomenon to the special packing motif of the PC carbonate planes where the outer (O1) oxygen of one molecule snuggles into the positively charged propyl end of another PC neighbor as depicted in Fig. 5.9.

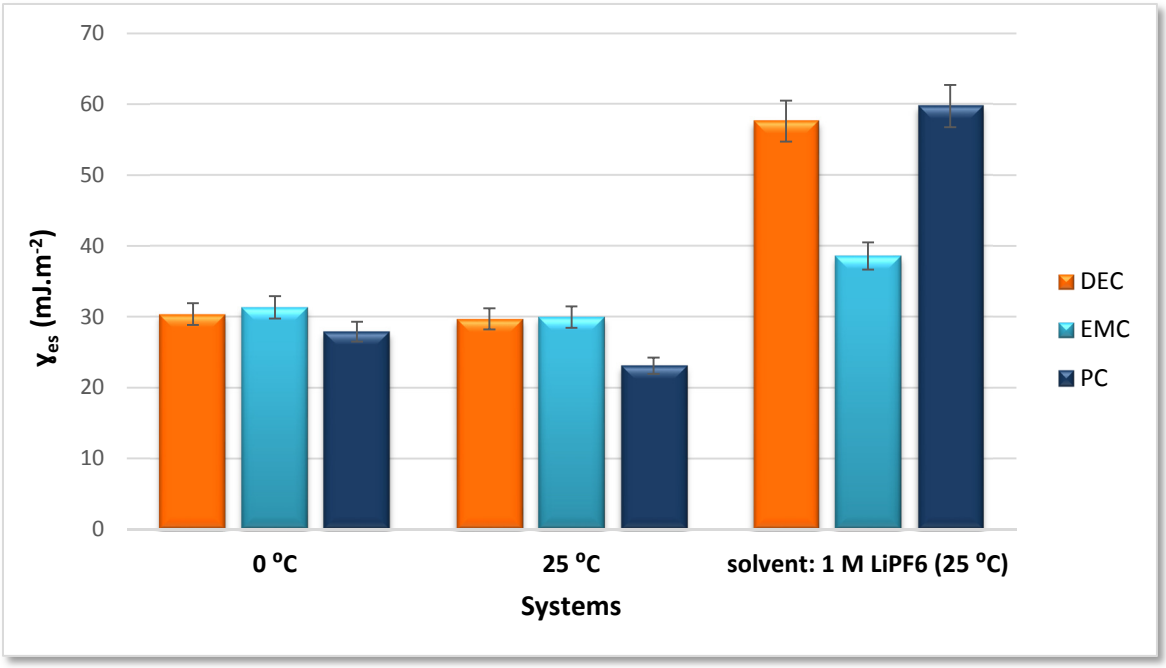

Fig. 5.8 Interfacial tension energies of the three system categories in similar simulation conditions.

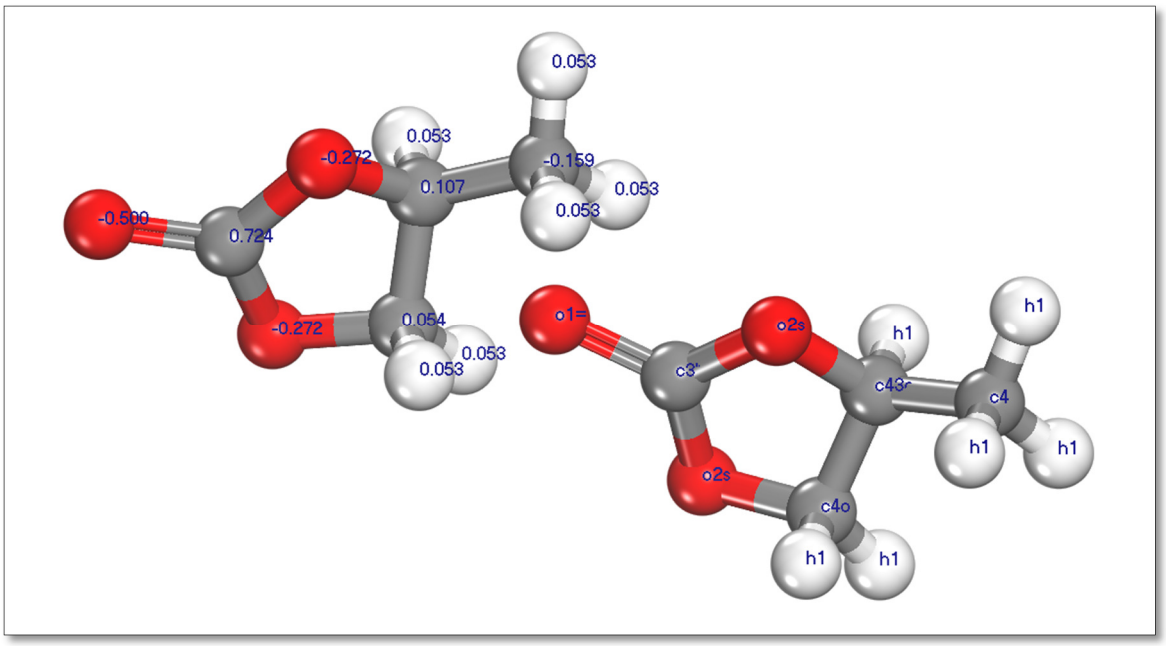

Fig. 5.9 Alignment of two neighboring PC molecules. The affinity between the outer oxygen of one molecule and the positively charge propyl group of another molecule results in the antiparallel arrangement of molecular dipole moments.

This arrangement of PC molecules results in the approximate antiparallel alignment of the neighboring molecular dipole moments [81]. Therefore, these molecules have more tendencies to stay close to the graphite layers and the relevant interfacial tension energy would be decreased significantly.

Although, to our knowledge, there is no study investigating the interfacial tension energies of each carbonate solvent with the graphite anode or PE and PP separators, a comparative study between the experimental results of one-component electrolyte-vapor surface energies and the values we calculated has been provided in Table 5.5 in absence of lithium salt.

Table 5.5 Experimental and theoretical values of carbonate solvents surface tension.

Solvent	Temperature (K)	Experimental γ_{ev} ($mJ.m^{-2}$)	Theoretical γ_{ev} ($mJ.m^{-2}$)
PC	273	n/a	78.83
	293	40[124]	n/a
	298.15	45[125]	60.65
	300	40.8[81]	n/a
EC	298.15	54.6[125]	n/a
	338	43.93[126]	n/a
DMC	298.15	31.9[125] 28.63,28.58[127]	n/a
	297.11	28.5[128]	n/a
DEC	273.18	29.2[129]	39.93
	298.15	25.92,25.87[127] 25.43,25.92[130]	26.36
	298.10	26.3[129]	n/a
EMC	273	n/a	48.4
	298	n/a	38.1

Accordingly, the empirical values change inversely with temperature while the surface energies of solvents with higher dielectric constants are higher than the solvent molecules with lower polarity where the both results are consistent with our calculations.

5.1.3. Impact of salt concentration

The influence of salt concentration on the electrolyte-electrode interfacial tension energy was investigated by employing three different $LiPF_6$ salt concentrations as 0.752, 1, and 1.254 M in an EMC electrolyte at $T = 25$ °C. It should be noted that the structure of graphite anode and the employed simulation process were identical. All the simulations were performed in a simulation cell with dimensions of 22.1 x 29.8 x 30.1 Å. The details of each simulated electrolyte system are shown in Table 5.6.

Table 5.6 Simulation specifications of three systems with variable of salt concentration.

Systems, salt molarity (M)	# of EMC molecules	# of $LiPF_6$ molecules	Cell density (g/m^3)
EMC:0.752 M $LiPF_6$	111	9	1.09
EMC:1 M $LiPF_6$	111	12	1.115
EMC:1.254 M $LiPF_6$	108	15	1.142

It is obvious to have higher densities by increasing salt concentration due to the fixed cell dimensions, which influences the interactions between solvent molecules and

salt ions and subsequently can affect the variation of interfacial tension energies. The three electrolyte systems are illustrated in Fig. 5.10 with a focus on relative positions of the salt ions. The encircled PF_6^- ions also represent the approximate positions of Li^+ ions since they were found close to each other but more difficult to be assigned in the bulk solution.

As pointed out before, the dielectric constant of a solvent is consistently considered as its power to dissociate the salt ions and produce free ionic charge carriers. Thus, there is an interplay between the value of solvent dielectric constant and the salt concentration as the factors which determine the salt dissociation rate in an electrolyte. According to the electrolytes depicted in Fig. 5.10, the relative distribution of PF_6^- and Li^+ ions are uniform in EMC: 0.752 M $LiPF_6$ system, which reflects the adequate value of EMC dielectric constant according to the salt concentration while by increasing the concentration of $LiPF_6$, EMC molecules would be less able to process the ion solvation successfully and consequently, salt aggregation occurs increasingly by addition of salt concentration. In the experimental studies, 1 M salt concentration has been introduced as a general maximum value where the number of free ions increases with salt concentration at values less than 1 M. However, any increase in salt concentration after this critical value results in more ion aggregation and, subsequently, higher viscosity of the electrolyte. This phenomenon reduces the number of free ions and the ionic mobility simultaneously [35,131]. The dielectric constant value of the solvent dictates the exact amount of critical salt concentration where a higher dielectric constant would shift the incidence of ion aggregation to higher salt concentrations.

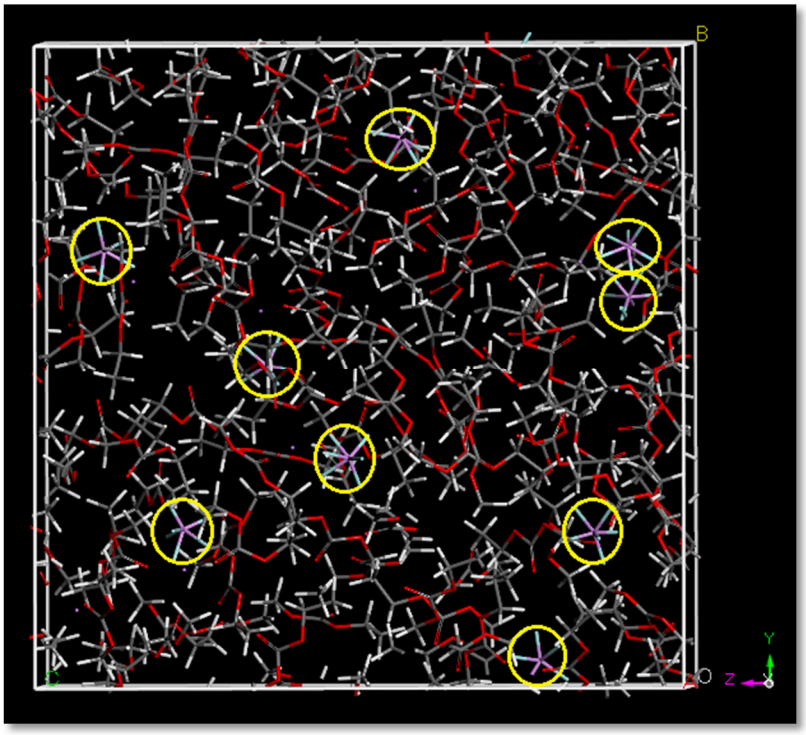

(a)

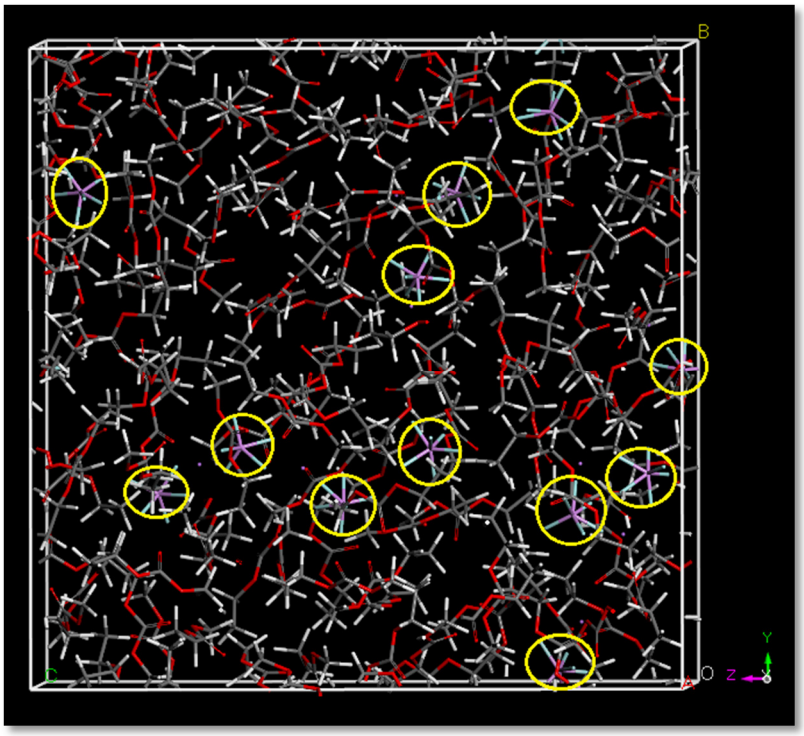

(b)

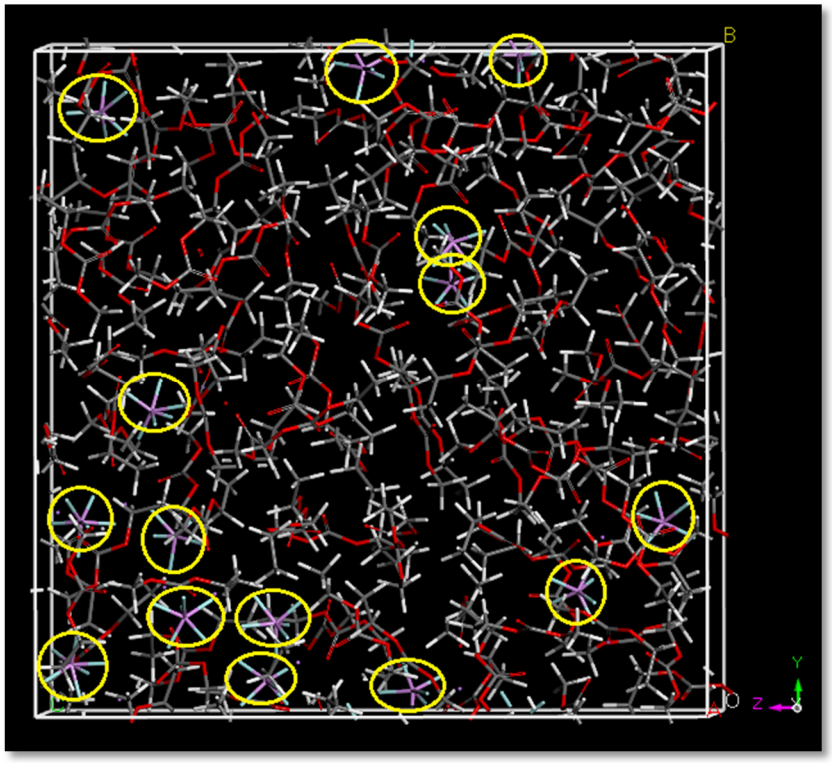

(c)

Fig. 5.10 Three EMC electrolytes with different $LiPF_6$ salt concentrations: (a) 0.752 M, (b) 1 M, and (c) 1.254 M. PF_6^- ions were assigned by yellow circles.

Since the salt concentrations higher than the dissociation ability of the solvent impose higher viscosity on electrolytes, the electrolyte-vacuum surface energies increase accordingly which result in higher γ_{es} values where the results are illustrated in Fig. 5.11.

According to the constant solvent type through all the three systems, viscosity is the dominant criterion to determine the interfacial tension values. Thus, the EMC: 0.752 M $LiPF_6$ system has the lowest γ_{es} and viscosity based on the results we provided in Fig. 5.11. However, it should be considered that this system may not supply adequate number of ionic charge carries which has detrimental effects on conductivity and capacity of LIB cell. Thus, employing the EMC: 1 M $LiPF_6$ system with a slightly higher value of γ_{es} would

be assigned as a more efficient choice. The related values of γ_{ev} and γ_{es} accompanied with the amounts of energy required to separate the electrolyte and the graphitic electrode were shown in Table 5.7.

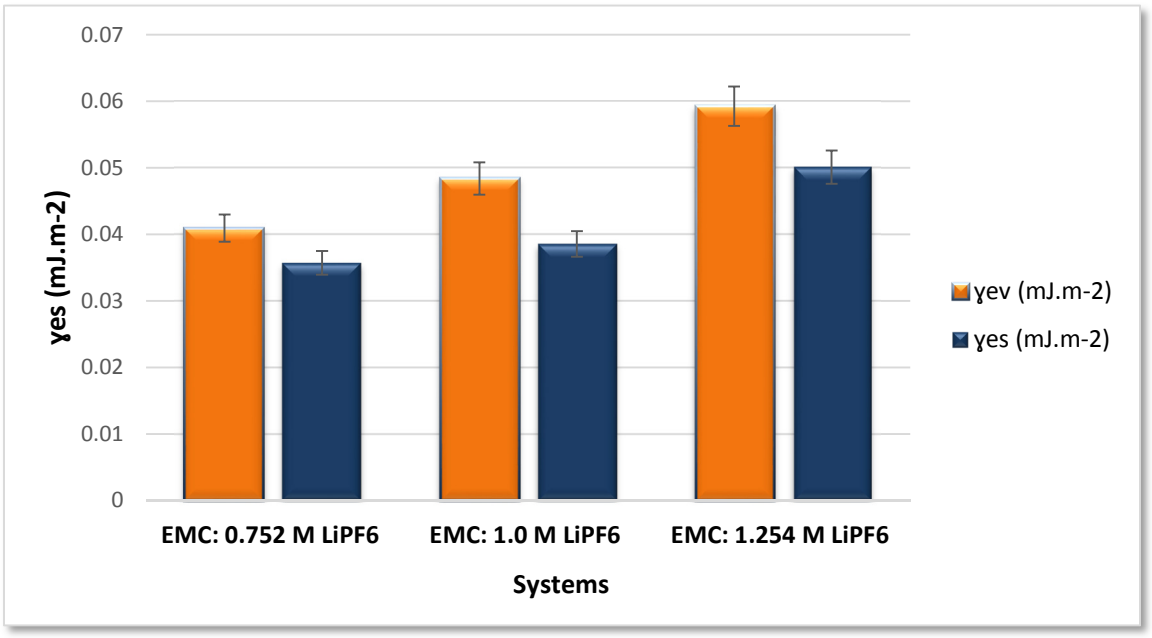

Fig. 5.11 $\gamma_{ev}$and γ_{es} values obtained for EMC: $LiPF_6$ electrolytes with different salt concentrations at T = 25 ºC.

The higher energies of separation are ascribed to the stronger intermolecular adhesion energies between the electrolyte and the electrode compared with the cohesion energies in each phase. Consequently, the two phases have more tendencies to interact with each other and subsequently the interfacial tension values are lower.

Table 5.7 γ_{ev}, γ_{es} , and ΔU_{es} values calculated for the systems incorporate EMC solvent with different salt concentrations.

System	γ_{ev} (mJ.m^{-2})	γ_{es} (mJ.m^{-2})	ΔU_{es} (kJ) x 10^{-23}
EMC: 0.752 M $LiPF_6$	40.94	35.73	154.48
EMC: 1 M $LiPF_6$	48.4	38.58	153.82
EMC: 1.254 M $LiPF_6$	59.25	50.1	123.69

5.2. Clustering phenomena

According to the results obtained from simulating the electrolytes incorporated EMC solvent with different salt concentrations, probability of ion aggregation will be increased by increasing the salt concentration. In these systems, the low dielectric constant of the solvent serves as the limiting factor to determine its ability to dissociate the salt ions. Consequently, the salt concentration and solvent dielectric constant are the two factors that mainly influence the occurrence of ion aggregation and clustering phenomena in the LIB electrolytes. The impact of salt concentration was studied in previous section while we investigate the effects of solvent dielectric constant on clustering of $LiPF_6$ ions in the current section.

Three systems of DEC, EMC, and PC one-component electrolytes were constructed which contained 1 M $LiPF_6$ salt in a cubic cell with length of 45Å as the structural details are shown in Table 5.8. All systems were equilibrated by NPT ensemble for 500 ps and

geometry optimization was done to reach the optimized density and a system in the most possible equilibrated status.

Table 5.8 Simulation specifications of three systems with variable of solvent type.

Systems, Solvent type	# of solvent molecules	# of $LiPF_6$ molecules	Cell density ($g.cm^{-3}$)
DEC:1 M $LiPF_6$	430	55	1.092
EMC:1 M $LiPF_6$	504	55	1.116
PC:1 M $LiPF_6$	618	55	1.285

The three investigated electrolytes are illustrated in Fig. 5.12 where the PF_6^- ions were assigned by yellow circles.

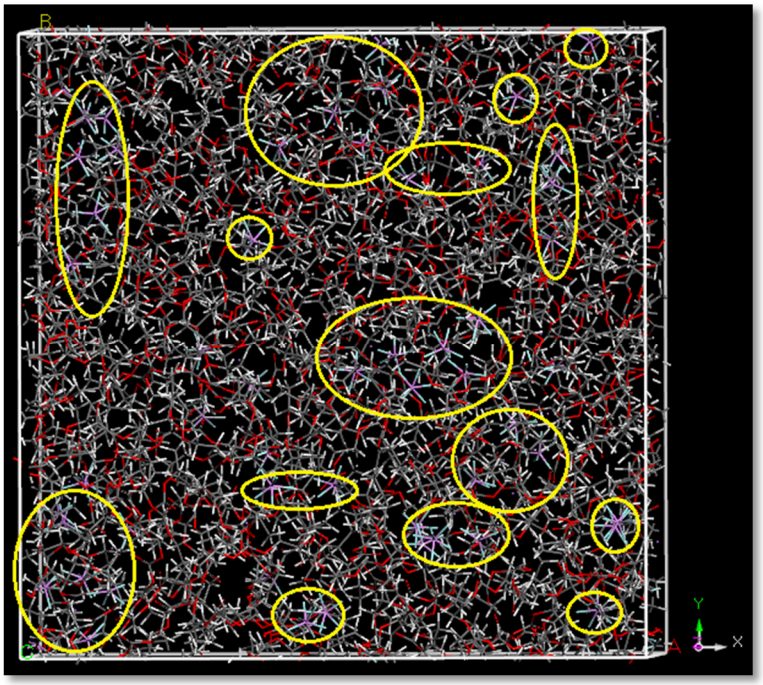

(a)

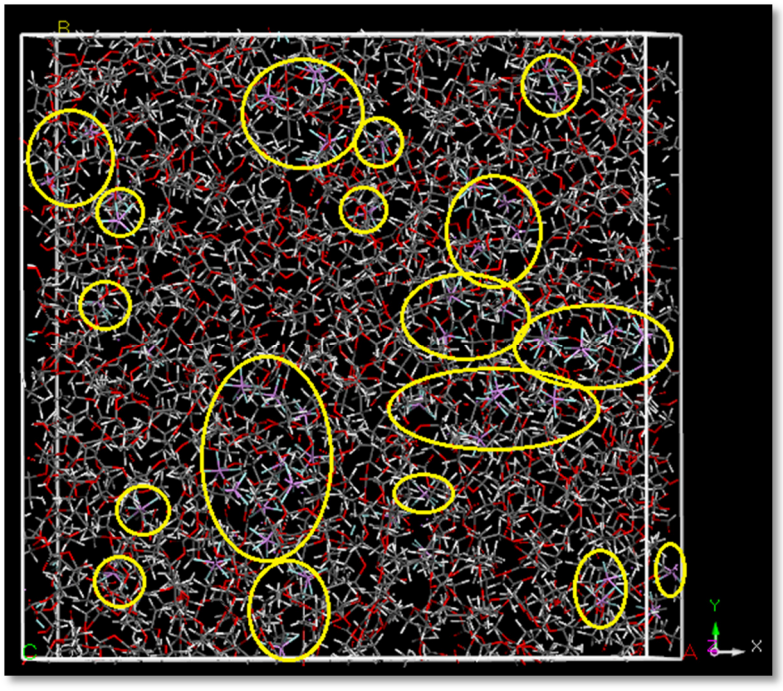

(b)

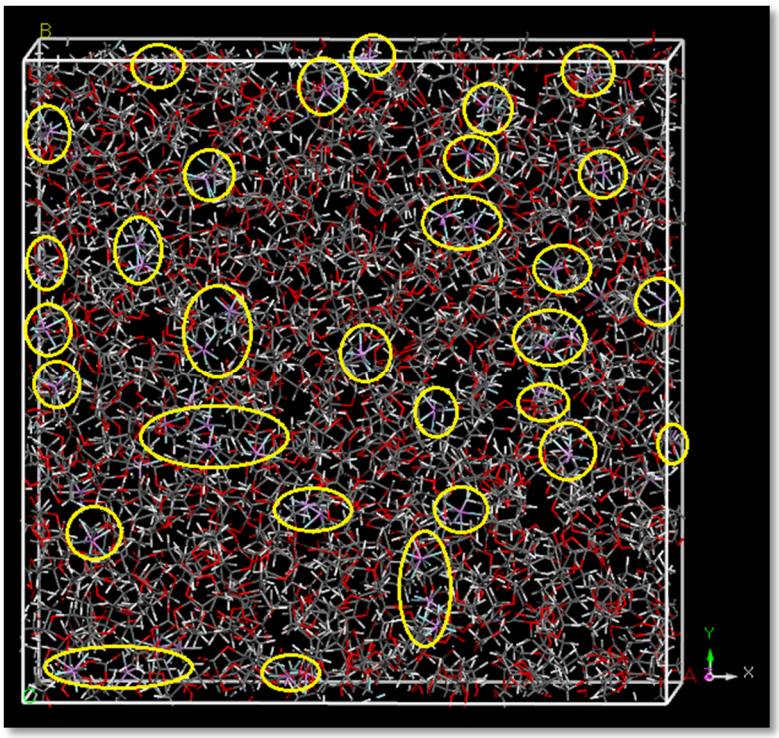

(c)

Fig. 5.12 Three solvent: 1 M $LiPF_6$ electrolytes with different solvent types: (a) DEC, (b) EMC, and (c) PC. PF_6^- ions were assigned by yellow circles.

DEC and EMC as the linear carbonates have dielectric constants of 2.805 and 2.96, respectively, while the ε value of PC is 64.92 due to its cyclic structure. According to the dielectric constants of these salts and the electrolytes depicted in Fig. 5.12, it is clear that PC as a solvent with higher dielectric constant is able to dissociate salt ions better and provide more charge carriers compared with DEC and EMC. Although the difference between the dielectric constants of employed linear solvents is low, more large associations of salt ions can be distinguished in DEC electrolyte with lower polarity. We quantified the above results through two approaches based on the coordination of all Li^+ and PF_6^- ions in each bulk electrolyte, and subsequently, the distance between the congruent ions.

The proportional coordination of salt ions is illustrated in Fig. 5.13 and 5.14 based on the projection of *x* values, i.e., A axis. The larger spheres represent the coordination of ions which their value of *x* is higher compared to *y* or *z*. Thus, uneven distribution of the size of the spheres reflects the clustering of the ions in relevant regions of the simulation box. Fig 5.12 depicts the coordination of Li^+ ions in three electrolytes while PF_6^- coordination is shown in Fig 5.13.

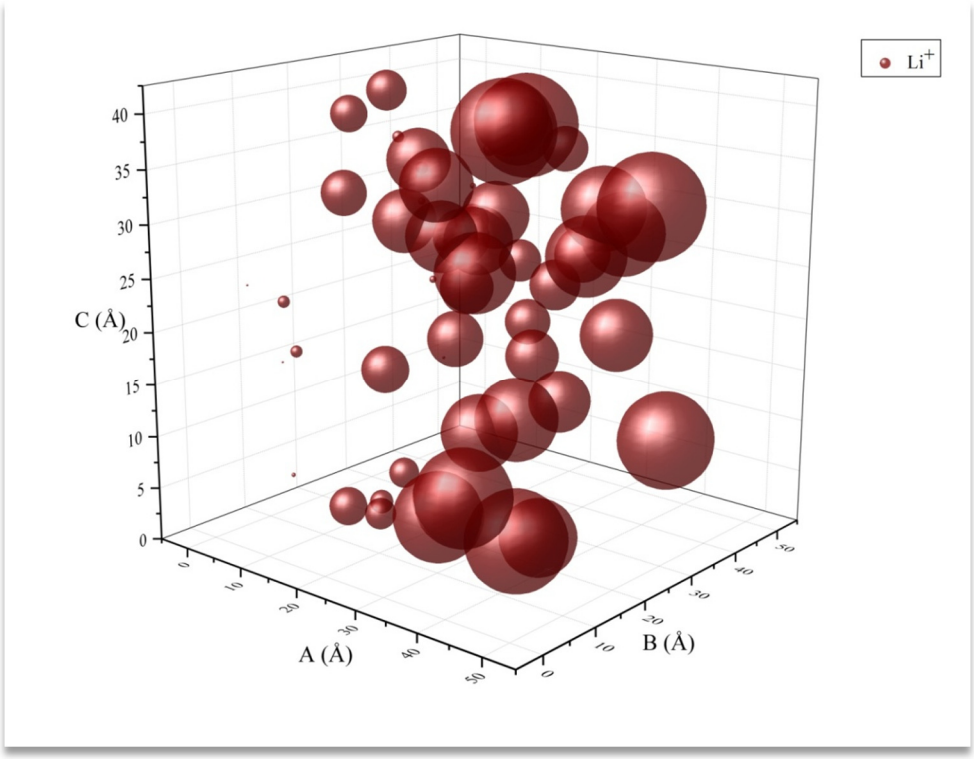

(a)

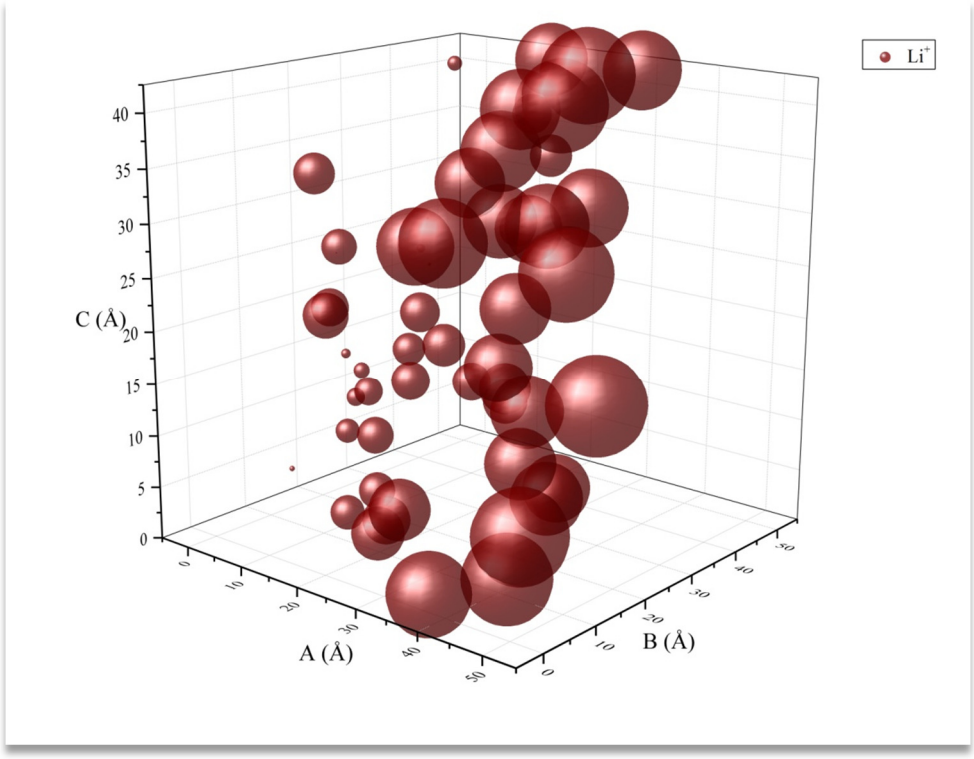

(b)

(c) 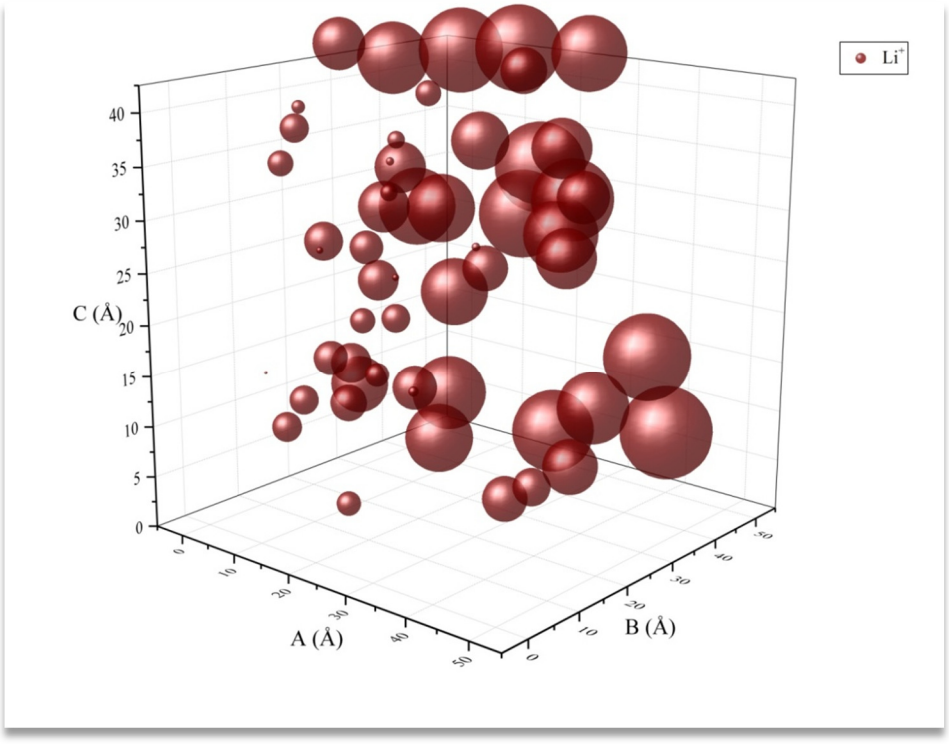

Fig. 5.13 Li^+ ions coordination in (a) DEC, (b) EMC, and (c) PC electrolytes.

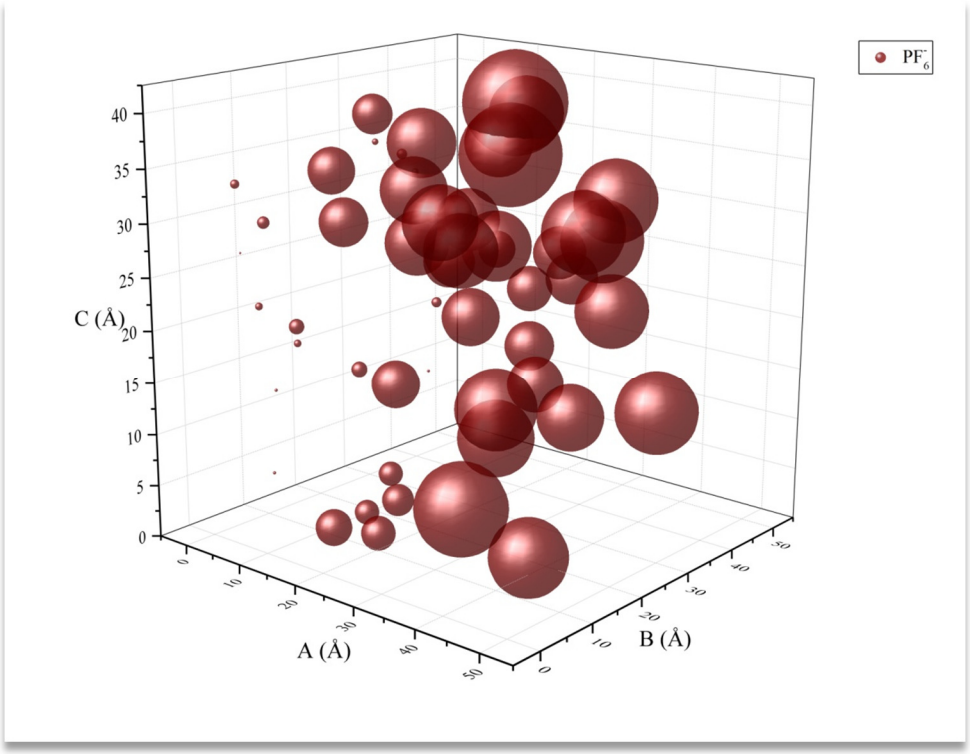

(a)

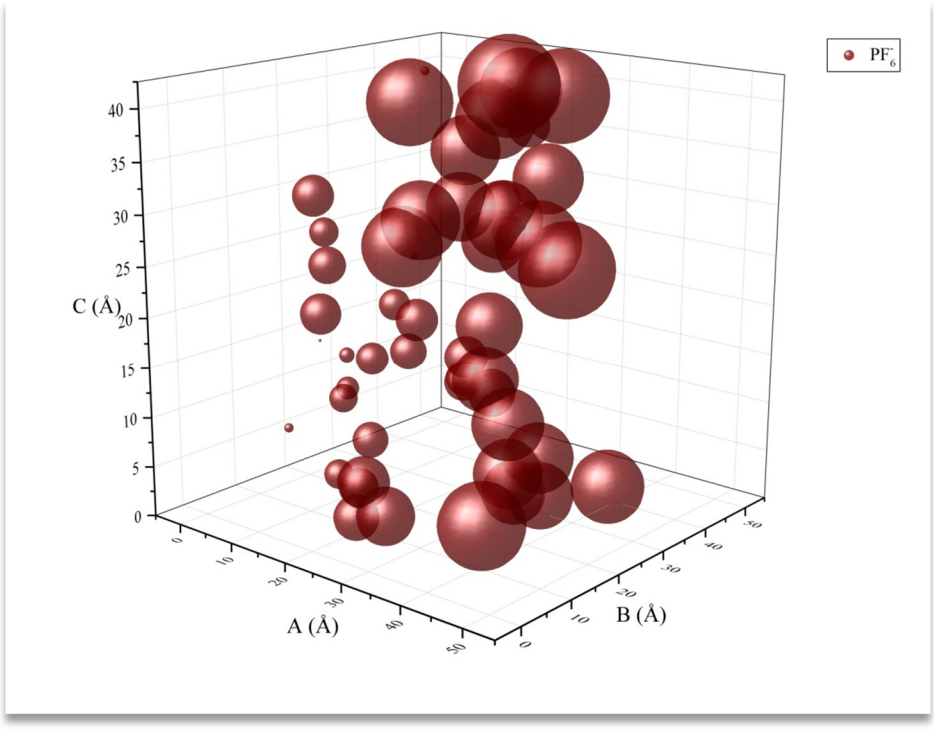

(b)

(c)

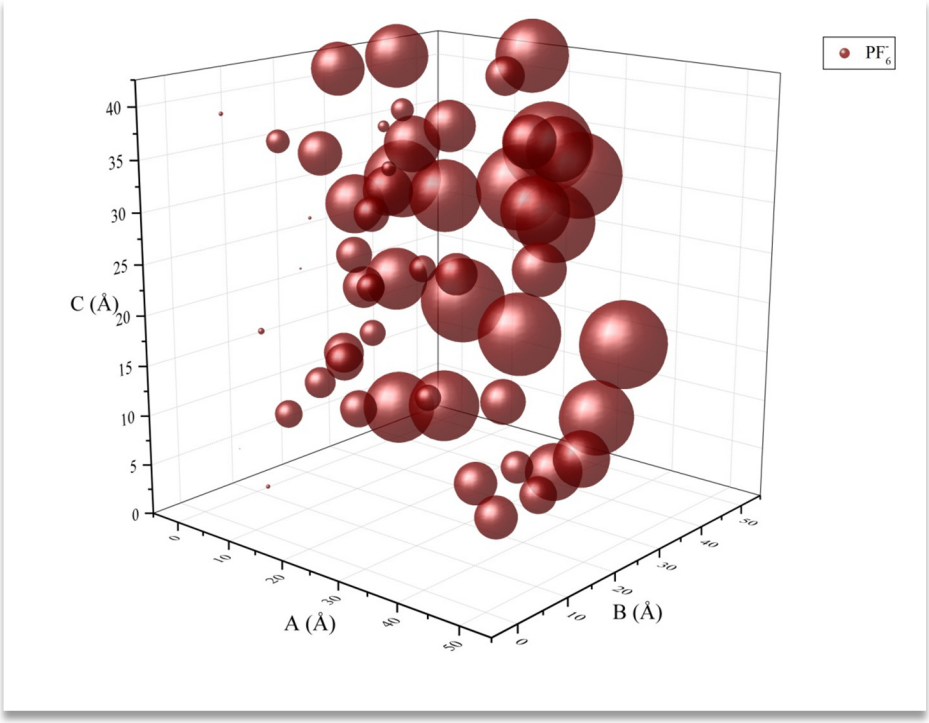

Fig. 5.14 PF_6^- ions coordination in (a) DEC, (b) EMC, and (c) PC electrolytes.

From the both sets of graphs, it can be figured out that the distribution balance of the coordination-dependent ion sizes is consistently related to the dielectric constant values of the solvents incorporated in different electrolytes which resulted in trend of DEC < EMC < PC; we have more uniform distribution of both Li^+ and PF_6^- ions in the PC electrolyte compared with EMC and DEC which is consistent with its higher ability to dissociate the salt ions and subsequently, its more tendency to participate in the ions solvation sheath as a cyclic carbonate solvent.

As the second procedure, we used ions coordination to calculate the relevant distances and determine the number of closest ions where the clustering phenomenon would be monitored according to the aggregation of more number of ions in the defined bins. By assigning the cell diagonal as the largest distance can be considered between two

ions, we divided its half-length into 20 bins and also the simulation cell into 9 smaller boxes. According to the total number of interactions between the ions based on the number of ions in the original cell, number of Li^+ or PF_6^- pairs were determined versus the bins as depicted in Fig. 5.15. As expected, the numbers of both Li^+ and PF_6^- ion pairs have more outspread distributions by increasing the number of bins in PC electrolyte since they are located in further distances. This behavior of ions affirms their better distribution in the PC bulk solution compared with DEC and EMC electrolytes. It should be noted that higher bin number corresponds to the longer molecular distances. Additionally, the distributions of Li^+ and PF_6^- ions in both DEC and EMC electrolytes are similar as they overlapped in many of the defined distances. These results are in good agreement with the close clustering rate of salt ions in mentioned electrolytes due to their similar values of dielectric constant.

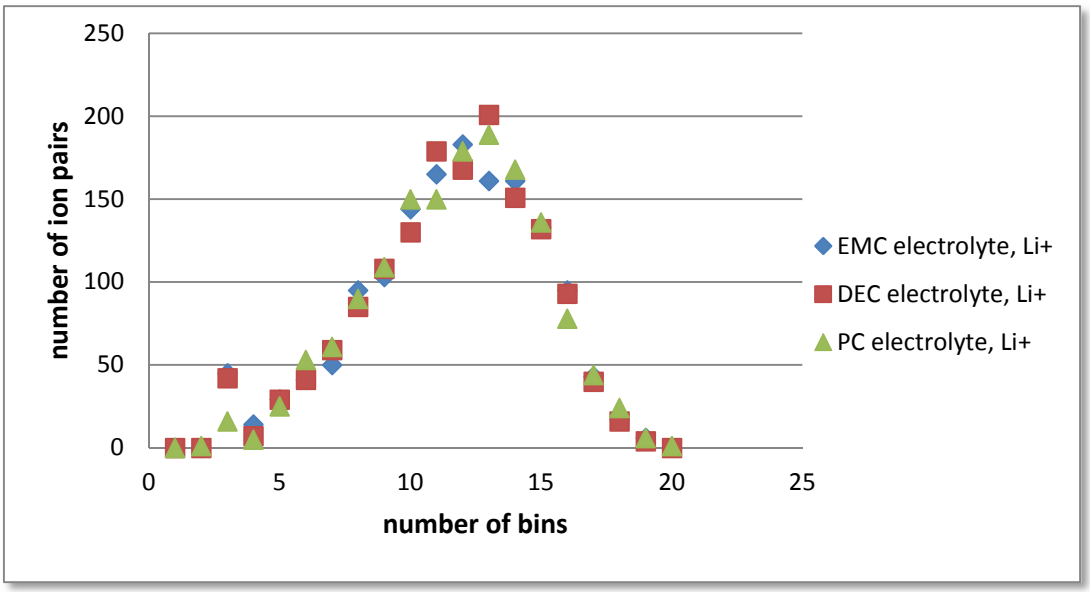

(a)

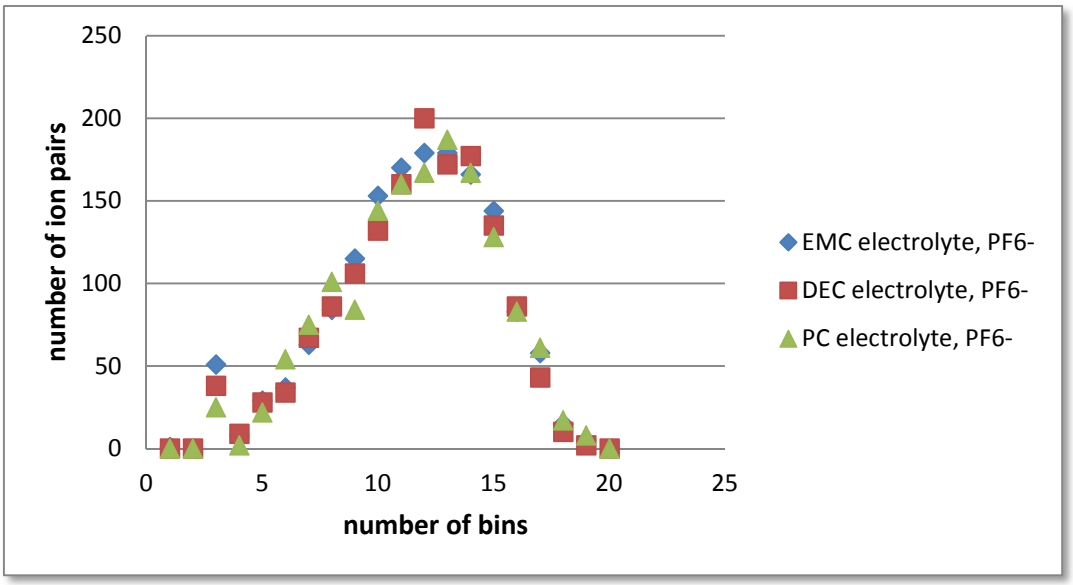

(b)

Fig. 5.15 (a) Li^+ and (b) PF_6^- ions distribution in the three studied electrolytes.

5.3. Electrolyte – PP/PE separators interfacial tension energies

In the current thesis, EMC and PC solvents were selected to calculate the interfacial tension energies of electrolyte with each of the PP and PE separators at T = 25 °C. The solution systems were the same as the electrolytes employed to investigate the wetting properties of electrolyte – graphite anode interfaces, therefore the same amounts of $\boldsymbol{\gamma_{ev}}$ were applied in the calculations. Additionally, the same simulation procedure was performed and five independent sets of simulations were carried out for each of the four combinations of electrolytes and separators. Fig. 5.16 illustrates the two structures required to calculate the separation energy of PC electrolyte and PP separator as the representative of other systems. It should be noted that the PP and PE chains employed in our simulations have the density of 0.843 and 0.855 g/cm^3, respectively.

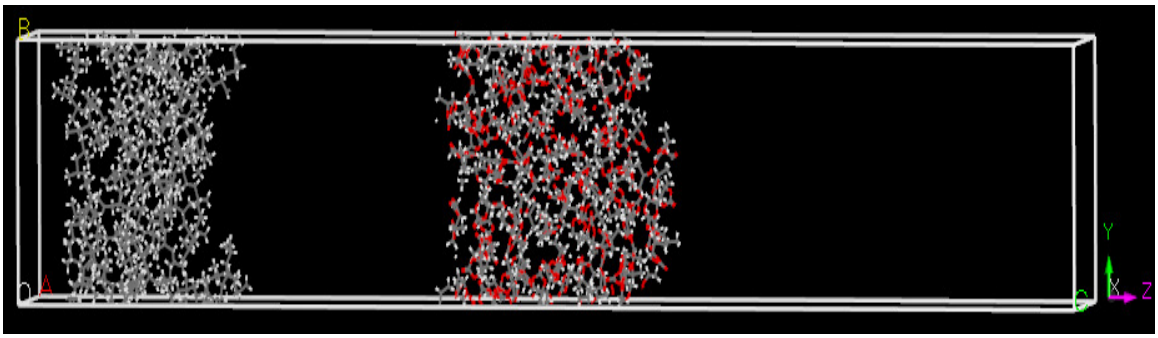

(a)

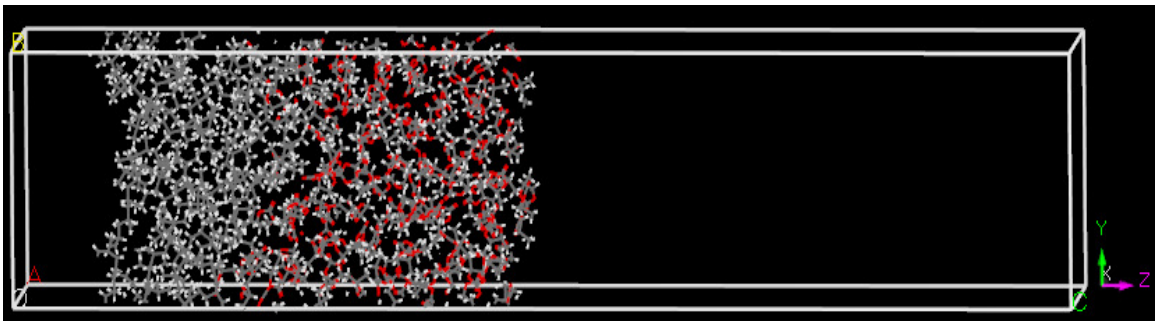

(b)

Fig. 5.16 (a) The electrolyte and PP molecules were kept separated for calculation of ΔU_{es}. (b) The electrolyte and PP molecules were placed in contact with each other for calculation of ΔU_{es}.

The interfacial energies calculated for the four systems are shown in Fig. 5.17 and Table 5.9.

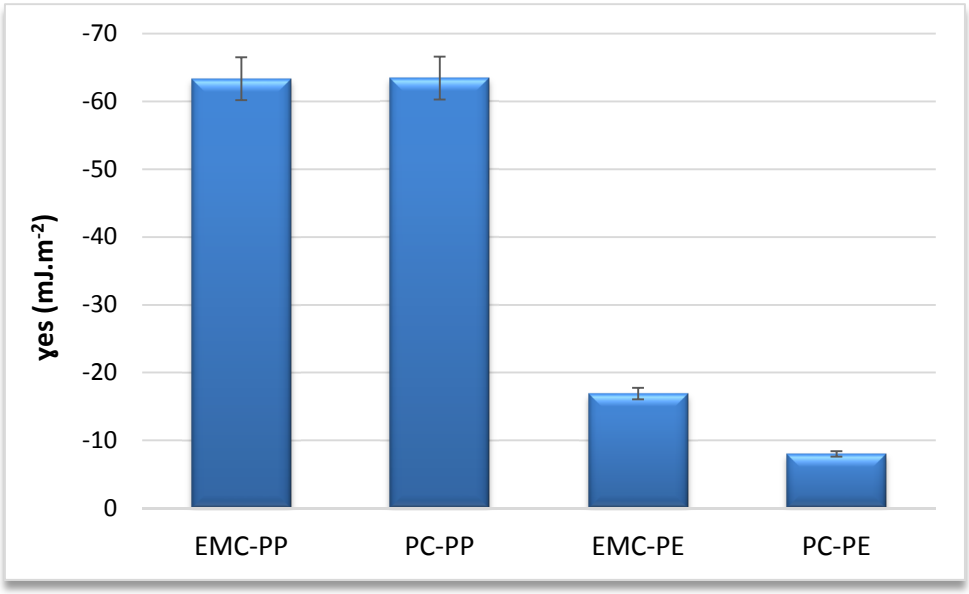

Fig. 5.17 γ_{es} values obtained for EMC and PC one-component electrolytes with each of the PP and PE separators.

Table 5.9 Surface tension and interfacial tension energies of the systems contain EMC and PC solvents in contact with PP and PE separators.

Solvent	γ_{ev} (mJ.m^{-2})	Separator	γ_{es} (mJ.m^{-2})
EMC	38.1	PP	-63.34
		PE	-16.91
PC	60.65	PP	-63.44
		PE	-8.03

We found all the calculated values of electrolyte – separator interfacial energies negative. Generally, the dominancy of adhesive forces compared to the strength of the cohesive forces reflects the high tendency of two phases to stay in contact with each other

where in the extreme cases the interfacial tension energies become negative. This phenomenon commonly happens between two liquid phases which implies release of a large amount of energy by maximizing the area of interface and mixture of two phases [132]. According to the limitation of MD computation technique in distinguishing the physical phase of the cell components, the electrolyte and the separator might be incorrectly considered as the miscible phases which caused negative values of the interfacial energies. Moreover, the computed results show higher affinity between PP and the electrolyte compared with the PE separator. In addition, as shown in Fig. 5.16(a), the polymer surfaces are not clearly defined (as compared with periodic graphite structures), and the relative surface areas are large. This is derived from the small computation size associated with the nature of MD computation. Therefore, a larger computational domain utilizing massively parallelized computing environment would generate a more reliable result especially for the simulations involving PE or PP surfaces, which still remains a future work beyond the current thesis.

6. Summary

In the present thesis, we address the carbonate-based electrolyte-anode/separator interfacial phenomena in LIB applications. An atomistic computational model has been developed employing the MD technique to investigate the impacts of i) solvent cyclicity, ii) temperature, and iii) salt concentration on the surface energies, interfacial tension energies, and clustering phenomena in one-component DEC, EMC, and PC carbonate solvents with $LiPF_6$ salt at T = 0 °C and T = 25 °C. Graphite and PE/PP separators were used in this work because they are considered as the most commonly used anode and separators in Li-ion cells, respectively.

By employing Clausius virial theorem, we calculated the surface energy in one-component electrolytes at temperatures 0 °C and 25 °C in addition to the systems of solvent: 1 M $LiPF_6$ at 25 °C. The results revealed that the viscosity and polarity strongly influence the γ_{ev}values in the systems. In the systems incorporating constant solvent type, the temperature changes inversely affect the surface energy in the absence of salt. The electrolyte viscosity can be monitored by the drag forces imposed on the electrolyte by the surrounding solvent molecules that participate in the solvation sheath of the migrating solvated salt ions. The higher γ_{ev} values in the solvent systems with 1 M $LiPF_6$ compared with the equivalent systems at the two different temperatures with no salt implies the dominancy of drag forces to express higher surface energies. By comparing the surface energies obtained for the studied systems with various solvents, the consistent relationship between the dielectric constants of solvents and their relevant surface tension values has

been found; the PC solvent system showed the highest surface energies due to the higher ε value, which is a common property of cyclic carbonate solvents.

The calculated surface energies were employed to obtain the electrolyte-anode/separator interfacial tension energies thermodynamically by considering the total change in Helmholtz free energies of the both liquid and solid phases. The results explicitly affirm their consistent relationship to the polarity of the electrolytes. In the systems containing EMC and DEC, the γ_{es} values do not change significantly with temperature. The dependency of dielectric constant on temperature is different for linear and cyclic carbonate solvents. The origin for the effect of molecular cyclicity on the dielectric constant has been attributed to the intramolecular strain of the cyclic structures that favors the conformation of better alignment of molecular dipoles, while the more flexible and open structure of linear carbonates results in the mutual cancellation of these dipoles. Therefore, the dielectric constants of DEC and EMC solvents are not changed significantly with temperature in general, whereas the consistent variation of dielectric constant versus temperature in the case of PC electrolytes results in the lower interfacial tension at 25 °C. The solvent systems with 1 M $LiPF_6$ displayed higher interfacial tensions compared to the systems with same type of solvents at different temperatures due to the additional effect of drag forces caused by the less mobile species in the solutions. The interfacial tension energies obtained for all three solvent categories reflect that the impact of solvent dielectric constant values for linear carbonate systems, where EMC systems display higher values of γ_{es} except EMC: 1 M $LiPF_6$ compared with the DEC systems. The PC: 1 M $LiPF_6$ system shows the highest interfacial tension value consistent with its highest polarity while the two other PC systems showed lower γ_{es}values despite its higher dielectric constant

compared with the equivalent DEC and EMC systems. Quantum chemistry studies ascribe this phenomenon to the special packing motif of the PC carbonate planes where the outer (O1) oxygen of one molecule snuggles into the positively charged propyl end of another PC neighbor. This arrangement of PC molecules results in the approximate antiparallel alignment of the neighboring molecular dipole moments. Therefore, these molecules have more tendencies to stay close to the graphite layers and the relevant interfacial tension energy would be decreased significantly.

The interfacial tension values for all the three solvent categories are generally lower than their relevant surface energies. This happens because the adhesive forces between electrolyte and graphite anode forming an interface are greater than the similar forces at the electrolyte-vacuum interface. The two systems containing DEC at temperature 25 °C behave inversely, which reflects the dominancy of cohesive forces in each of the liquid and solid phases.

The influence of salt concentration on the electrolyte-graphite anode interfacial tension energy was investigated by employing three different $LiPF_6$ salt concentrations as 0.752, 1, and 1.254 M in an EMC electrolyte at $T = 25$ °C. According to the constant solvent type through all the three systems, viscosity is the dominant factor to determine the interfacial tension values where the EMC: 0.752 M $LiPF_6$ system has the lowest γ_{es} and viscosity. However, it should be considered that this system may not supply adequate number of ionic charge carries which has detrimental effects on conductivity and capacity of LIB cell. Consequently, employing the EMC: 1 M $LiPF_6$ system with a slightly higher value of γ_{es} would be assigned as a more efficient choice.

According to the results obtained from simulating the electrolytes incorporated EMC solvent with different salt concentrations, probability of ion aggregation would be increased by increasing the salt concentration. In these systems, the low dielectric constant of the solvent serves as the limiting factor to determine its ability to dissociate the salt ions. Thus, the salt concentration and solvent dielectric constant are the two criteria that mainly influence the occurrence of clustering phenomena in the LIB electrolytes. Three systems of DEC, EMC, and PC one-component electrolytes were constructed which contained 1 M $LiPF_6$ salt to investigate the impact of solution polarity on clustering behavior of the salt ions. As a consequence of the two approaches employed to monitor the ions coordination and number of ion pairs, both Li^+ and PF_6^- ions have more outspread distributions in the bulk PC electrolyte which is in consistent agreement with its higher dielectric constant compared with DEC and EMC solutions. Accordingly, the relevant results of DEC electrolyte reveal the highest rate of salt ion clustering.

Additionally, the electrolyte-separator interfacial tension energies were calculated for one-component EMC and PC solutions with each of the PP and PE separators. The results implied more affinity of PP with the electrolytes while all the negative γ_{es} values reflected the high tendency of the electrolyte and the separator to be mixed regardless of considering their physical phases.

Although MD is powerful technique to predict the time evolution of a system incorporates interacting particles, it has some limitations which have been reflected in our study:

- Molecular dynamics is applicable for computer simulation of systems modelled at the atomic level. Although micro local investigations are very important to understand the fundamentals of interfacial phenomena, linking to meso/macro studies by considering the macro properties such as porosity of the electrodes/separators is not straightforward by employing MD method.
- During an MD simulation, atoms interact with each other where these interactions originate forces that act upon atoms and atoms move under the action of these instantaneous forces. As the atoms move, their relative positions and the forces will change. Since it is required to solve the equations of motion in each time step, there would be considerable fluctuations in quantities of the calculated interfacial energies. Thus, we need to run many simulations to eliminate this statistical inaccuracy which may not be cost-efficient. The results presented in the current thesis are mostly based on the five independent computations; the statistical accuracy of the results would be increased by performing more sets of simulations.
- One of the most important steps in our MD simulations is to equilibrate the system under the given conditions to obtain more realistic results. Generally, this goal can be achieved by increasing the size of the simulation box or the time of simulation. There is interplay between the size and time since by increasing size of the cell more demanding evaluation of the forces for large systems implies that each integration step takes longer time computationally while decreasing the time increases the probability of results inaccuracy. As expressed at the end of the Results Chapter, it would require a larger computation system to obtain more reliable results for systems including PE/PP polymeric materials.

The following is the future work that can be extended from the current study:

- Developing a larger computation model using parallelized MPI (message passing interface) protocols.
- Investigating the interfacial phenomena in multi-component carbonate-based electrolytes.
- Focusing on the microscopic structures of Li^+ ion solvation shell and investigating the impacts of solvation asymmetry on the viscosity and diffusivity of multi-component electrolytes by modifying the mixture composition.
- Comparative study of wetting properties in the electrolytes incorporate different types of lithium salts.
- Employing different conformations of linear carbonates to investigate the changes in the polarity of solvent molecules due to the different orientations of molecular dipole moments. Cis-cis conformer were used in this study while it has been supposed that the cis-trans solvent conformations display higher polarity.
- Investigating the wetting properties by employing polarizable force fields which can directly reduce ion pairing and correlated motions and indirectly increase diffusivity by reducing viscosity via reduced formation of clusters.

References

[1] Patil, A., Patil, V., Wook Shin, D., Choi, J. W., Paik, D. S., & Yoon, S. J. (2008). Issue and challenges facing rechargeable thin film lithium batteries. *Materials research bulletin*, *43*(8), 1913-1942.

[2] Yan, J., Zhang, J., Su, Y. C., Zhang, X. G., & Xia, B. J. (2010). A novel perspective on the formation of the solid electrolyte interphase on the graphite electrode for lithium-ion batteries. *Electrochimica Acta*, *55*(5), 1785-1794.

[3] Tarascon, J. M., & Armand, M. (2001). Issues and challenges facing rechargeable lithium batteries. *Nature*, *414*(6861), 359-367.

[4] Nazar, L. F., Goward, G., Leroux, F., Duncan, M., Huang, H., Kerr, T., & Gaubicher, J. (2001). Nanostructured materials for energy storage. *International Journal of Inorganic Materials*, *3*(3), 191-200.

[5] Hirscher, M. (2004). Nanoscale materials for energy storage. *Materials Science and Engineering: B*, *108*(1), 1.

[6] Santhanagopalan, S., Guo, Q., Ramadass, P., & White, R. E. (2006). Review of models for predicting the cycling performance of lithium ion batteries. *Journal of Power Sources*, *156*(2), 620-628.

[7] Moon, T., Kim, C., & Park, B. (2006). Electrochemical performance of amorphous-silicon thin films for lithium rechargeable batteries. *Journal of power sources*, *155*(2), 391-394.

[8] Schwenzel, J., Thangadurai, V., & Weppner, W. (2006). Developments of high-voltage all-solid-state thin-film lithium ion batteries. *Journal of power sources*, *154*(1), 232-238.

[9] Linden, D., & Reddy, T. B. (2002). Handbook of Batteries 3rd Edition. McGraw-Hill, New York. ISBN 0-07-135978-8.

[10] Aravindan, V., Gnanaraj, J., Madhavi, S., & Liu, H. K. (2011). Lithium-Ion Conducting Electrolyte Salts for Lithium Batteries. *Chemistry-A European Journal*, *17*(51), 14326-14346.

[11] Park, J. K. (Ed.). (2012). Principles and Applications of Lithium Secondary Batteries. Wiley-VCH, Germany. ISBN 978-3-527-33151-2.

[12] Ellis, B. L., Lee, K. T., & Nazar, L. F. (2010). Positive Electrode Materials for Li-Ion and Li-Batteries†. *Chemistry of Materials*, *22*(3), 691-714.

[13] Xu, B., Qian, D., Wang, Z., & Meng, Y. S. (2012). Recent progress in cathode materials research for advanced lithium ion batteries. *Materials Science and Engineering: R: Reports*, *73*(5), 51-65.

[14] Yabuuchi, N., & Ohzuku, T. (2003). Novel lithium insertion material of $LiCo_{1/3}Ni_{1/3}Mn_{1/3}O_2$ for advanced lithium-ion batteries. *Journal of Power Sources*, *119*, 171-174.

[15] Mizushima, K., Jones, P. C., Wiseman, P. J., & Goodenough, J. B. (1980). Li_xCoC_2 (0< x<-1): A new cathode material for batteries of high energy density. *Materials Research Bulletin*, *15*(6), 783-789.

[16] Ohzuku, T., Ueda, A., Nagayama, M., Iwakoshi, Y., & Komori, H. (1993). Comparative study of $LiCoO_2$, $LiNi_{1/2}Co_{1/2}$ and $LiNiO_2$ for 4 volt secondary lithium cells. *Electrochimica Acta*, *38*(9), 1159-1167..

[17] Meng, Y. S., Ceder, G., Grey, C. P., Yoon, W. S., & Shao-Horn, Y. (2004). Understanding the Crystal Structure of Layered $LiNi_{0.5}Mn_{0.5}O_2$ by Electron Diffraction and Powder Diffraction Simulation. *Electrochemical and Solid-State Letters*, *7*(6), A155-A158.

[18] Ohzuku, T., & Makimura, Y. (2001). Layered lithium insertion material of $LiCo_{1/3}Ni_{1/3}Mn_{1/3}O_2$ for lithium-ion batteries. *Chemistry Letters*, *30*(7), 642-643.

[19] Wang, Y. (2004). *Lithium-ion batteries*. P. B. Balbuena (Ed.). Imperial college press.

[20] Besenhard, J. O., Yang, J., & Winter, M. (1997). Will advanced lithium-alloy anodes have a chance in lithium-ion batteries? *Journal of Power Sources*, *68*(1), 87-90.

[21] Winter, M., Besenhard, J. O., Spahr, M. E., & Novak, P. (1998). Insertion electrode materials for rechargeable lithium batteries. *Advanced materials*, *10*(10), 725-763.

[22] Tekinalp, H. L., Cervo, E. G., Fathollahi, B., & Thies, M. C. (2013). The effect of molecular composition and structure on the development of porosity in pitch-based activated carbon fibers. *Carbon*, *52*, 267-277.

[23] Goodenough, J. B., & Kim, Y. (2011). Challenges for rechargeable batteries. *Journal of Power Sources*, *196*(16), 6688-6694.

[24] Wang, Y., Zaghib, K., Guerfi, A., Bazito, F. F., Torresi, R. M., & Dahn, J. R. (2007). Accelerating rate calorimetry studies of the reactions between ionic liquids and charged lithium ion battery electrode materials. *Electrochimica acta*, *52*(22), 6346-6352.

[25] Bates, J. B., Dudney, N. J., Neudecker, B., Ueda, A., & Evans, C. D. (2000). Thin-film lithium and lithium-ion batteries. *Solid State Ionics*, *135*(1), 33-45.

[26] Persi, L., Croce, F., & Scrosati, B. (2002). A $LiTi_2O_4$–$LiFePO_4$ novel lithium-ion polymer battery. *Electrochemistry communications*, *4*(1), 92-95.

[27] Ahmad, S. (2009). RETRACTED ARTICLE: Polymer electrolytes: characteristics and peculiarities. *Ionics*, *15*(3), 309-321.

[28] Achiha, T., Nakajima, T., Ohzawa, Y., Koh, M., Yamauchi, A., Kagawa, M., & Aoyama, H. (2010). Thermal stability and electrochemical properties of fluorine compounds as nonflammable solvents for lithium-ion batteries. *Journal of the Electrochemical Society*, *157*(6), A707-A712.

[29] Fry, A. J. (1989). *Synthetic organic electrochemistry*. John Wiley & Sons.

[30] Blomgren, G. E. (2003). Liquid electrolytes for lithium and lithium-ion batteries. *Journal of Power Sources*, *119*, 326-329.

[31] Ding, M. S., Xu, K., Zhang, S., & Jow, T. R. (2001). Liquid/solid phase diagrams of binary carbonates for lithium batteries part II. *Journal of the Electrochemical Society*, *148*(4), A299-A304.

[32] Tasaki, K., Goldberg, A., Lian, J. J., Walker, M., Timmons, A., & Harris, S. J. (2009). Solubility of lithium salts formed on the lithium-ion battery negative electrode surface in organic solvents. *Journal of the Electrochemical Society*, *156*(12), A1019-A1027.

[33] Aurbach, D., Talyosef, Y., Markovsky, B., Markevich, E., Zinigrad, E., Asraf, L, & Kim, H. J. (2004). Design of electrolyte solutions for Li and Li-ion batteries: a review. *Electrochimica Acta*, *50*(2), 247-254.

[34] Han, H. B., Zhou, S. S., Zhang, D. J., Feng, S. W., Li, L. F., Liu, K., ... & Zhou, Z. B. (2011). Lithium bis (fluorosulfonyl) imide (LiFSI) as conducting salt for nonaqueous liquid electrolytes for lithium-ion batteries: Physicochemical and electrochemical properties. *Journal of Power Sources*, *196*(7), 3623-3632.

[35] Xu, K. (2004). Nonaqueous liquid electrolytes for lithium-based rechargeable batteries. *Chemical reviews*, *104*(10), 4303-4418.

[36] Zeng, Z., Liang, W. I., Liao, H. G., Xin, H., Chu, Y. H., & Zheng, H. (2014). Visualization of Electrode-Electrolyte Interfaces in $LiPF_6$/EC/DEC Electrolyte for Lithium Ion Batteries via In-Situ TEM. *Nano letters*.

[37] Ue, M. (2009). Role-assigned electrolytes: additives. In *Lithium-Ion Batteries* (pp. 75-115). Springer New York.

[38] El Ouatani, L., Dedryvere, R., Siret, C., Biensan, P., Reynaud, S., Iratcabal, P., & Gonbeau, D. (2009). The effect of vinylene carbonate additive on surface film formation on both electrodes in Li-ion batteries. *Journal of the Electrochemical Society*, *156*(2), A103-A113.

[39] Zhong, Q., Sacken, U. V., Gao, Y., & Dahn, J. R. (1997). Method for preparing $Li_{1+x}Mn_{2-xy}M_yO_4$ for use in lithium batteries. U.S. Patent 5,650,245.

[40] Kim, K. J., Park, M. S., Yim, T., Yu, J. S., & Kim, Y. J. (2014). Electron-beam-irradiated polyethylene membrane with improved electrochemical and thermal properties for lithium-ion batteries. *Journal of Applied Electrochemistry*, *44*(3), 345-352.

[41] Woo, J. J., Zhang, Z., Rago, N. L. D., Lu, W., & Amine, K. (2013). A high performance separator with improved thermal stability for Li-ion batteries. *Journal of Materials Chemistry A*, *1*(30), 8538-8540.

[42] Arora, P., & Zhang, Z. (2004). Battery separators. *Chemical reviews*, *104*(10), 4419-4462.

[43] Winter, M., & Brodd, R. J. (2004). What are batteries, fuel cells, and supercapacitors? *Chemical reviews*, *104*(10), 4245-4270.

[44] Suo, L., Hu, Y. S., Li, H., Armand, M., & Chen, L. (2013). A new class of solvent-in-salt electrolyte for high-energy rechargeable metallic lithium batteries. *Nature communications*, *4*, 1481.

[45] Li, S. Y., Ma, P. H., Song, S. T., Ren, Q. D., & Li, F. Q. (2008). Conductivity of LiBOB in various ternary solvent blends and the electrochemical performance of LiBOB-PC/EMC/DMC used in Li/MCMB and $LiFePO_4$/Li cells. *Russian Journal of Electrochemistry*, *44*(10), 1144-1148.

[46] Ding, M. S., Xu, K., & Jow, T. R. (2005). Conductivity and Viscosity of PC-DEC and PC-EC Solutions of LiBOB. *Journal of the Electrochemical Society*, *152*(1), A132-A140.

[47] Ding, M. S., Xu, K., Zhang, S. S., Amine, K., Henriksen, G. L., & Jow, T. R. (2001). Change of conductivity with salt content, solvent composition, and temperature for electrolytes of $LiPF_6$ in ethylene carbonate-ethyl methyl carbonate. *Journal of the Electrochemical Society*, *148*(10), A1196-A1204.

[48] Ding, M. S., & Jow, T. R. (2009). Physicochemical Properties of Non-Aqueous Solvents and Electrolytes for Lithium Battery Applications. *ECS Transactions*, *16*(35), 183-214.

[49] Wilkinson, D. S. (2000). *Mass transport in solids and fluids*. Cambridge university press.

[50] Stewart, S. G., & Newman, J. (2008). The use of UV/vis absorption to measure diffusion coefficients in LiPF6 electrolytic solutions. *Journal of the Electrochemical Society*, *155*(1), F13-F16.

[51] Krachkovskiy, S. A., Pauric, A. D., Halalay, I. C., & Goward, G. R. (2013). Slice-Selective NMR Diffusion Measurements: A Robust and Reliable Tool for In Situ Characterization of Ion-Transport Properties in Lithium-Ion Battery Electrolytes. *The Journal of Physical Chemistry Letters*, *4*(22), 3940-3944.

[52] Nyman, A., Behm, M., & Lindbergh, G. (2008). Electrochemical characterisation and modelling of the mass transport phenomena in $LiPF_6$–EC–EMC electrolyte, *Electrochimica Acta*, *53*(22), 6356-6365.

[53] Zugmann, S., Moosbauer, D., Amereller, M., Schreiner, C., Wudy, F., Schmitz, R., ... & Gores, H. J. (2011). Electrochemical characterization of electrolytes for lithium-ion batteries based on lithium difluoromono (oxalato) borate. *Journal of Power Sources*, *196*(3), 1417-1424.

[54] Julien, C., & Nazri, G. (Eds.). (1994). *Solid state batteries: materials design and optimization* (Vol. 271). Springer.

[55] Ganesh, P., Jiang, D. E., & Kent, P. R. C. (2011). Accurate static and dynamic properties of liquid electrolytes for Li-ion batteries from ab initio molecular dynamics. *J. Phys. Chem. B*, *115*(12), 3085-3090.

[56] Yuan, Y., & Lee, T. R. (2013). Contact angle and wetting properties. In Surface Science Techniques (pp. 3-34). Springer Berlin Heidelberg.

[57] Żenkiewicz, M. (2007). Methods for the calculation of surface free energy of solids. *Journal of Achievements in Materials and Manufacturing Engineering*, *24*(1), 137-145.

[58] S. Vowell, Microfluidics: the effects of surface tension, (2009), http://www, phys. washington, edu/users/sharpe/486/vowell_f, pdf.

[59] Dahbi, M., Violleau, D., Ghamouss, F., Jacquemin, J., Tran-Van, F., Lemordant, D., & Anouti, M. (2012). Interfacial Properties of LiTFSI and LiPF6-Based Electrolytes in Binary and Ternary Mixtures of Alkylcarbonates on Graphite Electrodes and Celgard Separator. *Industrial & Engineering Chemistry Research*, *51*(14), 5240-5245.

[60] Bockris, J. O'M., Reddy, A. K. N. (2000). Modern Electrochemistry, 2nd ed. Plenum Press: New York.Vol. 2.

[61] Kameda, Y., Umebayashi, Y., Takeuchi, M., Wahab, M. A., Fukuda, S., Ishiguro, S. I., ... & Usuki, T. (2007). Solvation structure of Li^+ in concentrated $LiPF_6$-propylene carbonate solutions. *The Journal of Physical Chemistry B*, *111*(22), 6104-6109.

[62] Tasaki, K., & Harris, S. J. (2010). Computational study on the solubility of lithium salts formed on lithium ion battery negative electrode in organic solvents. *The Journal of Physical Chemistry C*, *114*(17), 8076-8083.

[63] Leung, K., & Budzien, J. L. (2010). Ab initio molecular dynamics simulations of the initial stages of solid–electrolyte interphase formation on lithium ion battery graphitic anodes. *Physical Chemistry Chemical Physics*, *12*(25), 6583-6586.

[64] http://accelrys.com/products/materials-studio.

[65] http://www.gromacs.org/.

[66] http://lammps.sandia.gov/.

[67] http://www.charmm.org/.

[68] http://www.charmm.org/.

[69] Kalugin, O. N., Volobuev, M. N., & Kolesnik, Y. V. (1999). *Kharkov University Bulletin, Chemistry Series .454 (58).*

[70] Lucretius, www.che.utah.edu/~gdsmith.

[71] Borodin, O., & Smith, G. D. (2009). Quantum chemistry and molecular dynamics simulation study of dimethyl carbonate: ethylene carbonate electrolytes doped with LiPF6. *The Journal of Physical Chemistry B*, *113*(6), 1763-1776.

[72] Tenney, C. M., & Cygan, R. T. (2013). Analysis of Molecular Clusters in Simulations of Lithium-Ion Battery Electrolytes. *The Journal of Physical Chemistry C*, *117*(47), 24673-24684.

[73] Ouyang, C., & Chen, L. (2013). Physics towards next generation Li secondary batteries materials: A short review from computational materials design perspective. *Science China Physics, Mechanics and Astronomy*, *56*(12), 2278-2292.

[74] Borodin, O., & Smith, G. D. (2006). LiTFSI structure and transport in ethylene carbonate from molecular dynamics simulations. *The Journal of Physical Chemistry B*, *110*(10), 4971-4977.

[75] Borodin, O., & Smith, G. D. (2007). Li^+ transport mechanism in oligo (ethylene oxide) s compared to carbonates. *Journal of solution chemistry*, *36*(6), 803-813.

[76] Borodin, O., & Smith, G. D. (2009). Quantum chemistry and molecular dynamics simulation study of dimethyl carbonate: ethylene carbonate electrolytes doped with LiPF6. *The Journal of Physical Chemistry B*, *113*(6), 1763-1776.

[77] Lee, S., & Park, S. S. (2013). Dielectric constants of binary mixtures of propylene carbonate with dimethyl carbonate and ethylene carbonate from molecular dynamics simulation: comparison between non-polarizable and polarizable force fields. Molecular Physics, 111(2), 277-285.

[78] Leontyev, I., & Stuchebrukhov, A. (2011). Accounting for electronic polarization in non-polarizable force fields. Phys. Chem. Chem. Phys., 13(7), 2613-2626.

[79] Kirkwood, J. G., & Buff, F. P. (2004). The statistical mechanical theory of surface tension. *The Journal of Chemical Physics*, *17*(3), 338-343.

[80] Lee, L. L. (1988). *Molecular thermodynamics of nonideal fluids* (Vol. 425). Boston: Butterworths.

[81] You, X., Chaudhari, M. I., Pratt, L. R., Pesika, N., Aritakula, K. M., & Rick, S. W. (2013). Interfaces of propylene carbonate. *The Journal of chemical physics*, *138*(11), 114708.

[82] Laird, B. B., & Davidchack, R. L. (2005). Direct calculation of the crystal-melt interfacial free energy via molecular dynamics computer simulation. *The Journal of Physical Chemistry B*, *109*(38), 17802-17812.

[83] Broughton, J. Q., & Gilmer, G. H. (1986). Molecular dynamics investigation of the crystal–fluid interface. VI. Excess surface free energies of crystal–liquid systems. *The Journal of chemical physics*, *84*(10), 5759-5768.

[84] Davidchack, R. L. (2010). Hard spheres revisited: Accurate calculation of the solid–liquid interfacial free energy. *The Journal of chemical physics*, *133*(23), 234701.

[85] Del Río, F., & Gil-Villegas, A. (1992). Collision frequencies and mean collision parameters in the Lennard-Jones system. *Molecular Physics*, *77*(2), 223-238.

[86] De Miguel, E., & Jackson, G. (2006). The nature of the calculation of the pressure in molecular simulations of continuous models from volume perturbations. *The Journal of chemical physics*, *125*(16), 164109.

[87] Nishida, S., Surblys, D., Yamaguchi, Y., Kuroda, K., Kagawa, M., Nakajima, T., & Fujimura, H. (2014). Molecular dynamics analysis of multiphase interfaces based on in situ extraction of the pressure distribution of a liquid droplet on a solid surface. *The Journal of chemical physics*, *140*(7), 074707.

[88] Hoyt, J. J., Asta, M., & Karma, A. (2001). Method for computing the anisotropy of the solid-liquid interfacial free energy. *Physical Review Letters*, *86*(24), 5530.

[89] Davidchack, R. L., Morris, J. R., & Laird, B. B. (2006). The anisotropic hard-sphere crystal-melt interfacial free energy from fluctuations. *The Journal of chemical physics*, *125*(9), 094710.

[90] Sergi, D., Scocchi, G., & Ortona, A. (2012). Molecular dynamics simulations of the contact angle between water droplets and graphite surfaces. *Fluid Phase Equilibria*, *332*, 173-177.

[91] Wang, F. C., & Zhao, Y. P. (2013). Contact angle hysteresis at the nanoscale: a molecular dynamics simulation study. *Colloid and Polymer Science*, *291*(2), 307-315.

[92] Vanzo, D., Bratko, D., & Luzar, A. (2012). Wettability of pristine and alkyl-functionalized graphane. *The Journal of chemical physics*, *137*(3), 034707.

[93] Dai, Z. W., Ling, J., Huang, X. J., Wan, L. S., & Xu, Z. K. (2011). Molecular simulation on the interactions of water with polypropylene surfaces. *The Journal of Physical Chemistry C*, *115*(21), 10702-10708.

[94] Yan, M., Yang, X., & Lu, Y. (2013). Wetting behavior of water droplet on solid surfaces in solvent environment: A molecular simulation study. *Colloids and Surfaces A: Physicochemical and Engineering Aspects*, *429*, 142-148.

[95] De Ruijter, M. J., Blake, T. D., & De Coninck, J. (1999). Dynamic wetting studied by molecular modeling simulations of droplet spreading. *Langmuir*, *15*(22), 7836-7847.

[96] Dykstra, C., Frenking, G., Kim, K., & Scuseria, G. (Eds.). (2011). *Theory and applications of computational chemistry: the first forty years*. Elsevier.

[97] Plimpton, S. (1995). Fast parallel algorithms for short-range molecular dynamics. *Journal of Computational Physics*, *117*(1), 1-19.

[98] Allen, M. P., & Tildesley, D. J. (Eds.). (1989). *Computer simulation of liquids*. Oxford university press.

[99] Yip, S. (Ed.). (2007). *Handbook of materials modeling*. Springer.

[100] Allen, M. P. (2004). Introduction to molecular dynamics simulation. *Computational Soft Matter: From Synthetic Polymers to Proteins*, *23*, 1-28.

[101] Xie, C., & Pallant, A. (2011). The molecular workbench software: an innovative dynamic modeling tool for nanoscience education. In *Models and Modeling* (pp. 121-139). Springer Netherlands.

[102] Li, J. (2005). Basic molecular dynamics. In *Handbook of Materials Modeling* (pp. 565-588). Springer Netherlands.

[103] Deem, M. W., Newsam, J. M., & Sinha, S. K. (1990). The h= 0 term in Coulomb sums by the Ewald transformation. *Journal of Physical Chemistry*, *94*(21), 8356-8359.

[104] Rapaport, D. C. (2004). *The art of molecular dynamics simulation*. Cambridge university press.

[105] Ewald, P. P. (1921). Ewald summation. *Ann. Phys.*, *369*, 253.

[106] Stenhammar, J., Trulsson, M., & Linse, P. (2011). Some comments and corrections regarding the calculation of electrostatic potential derivatives using the Ewald summation technique. *The Journal of chemical physics*, *134*(22), 224104.

[107] Sun, H. (1998). COMPASS: An ab initio force-field optimized for condensed-phase applications overview with details on alkane and benzene compounds. *The Journal of Physical Chemistry B*, *102*(38), 7338-7364.

[108] Bunte, S. W., & Sun, H. (2000). Molecular modeling of energetic materials: the parameterization and validation of nitrate esters in the COMPASS force field. *The Journal of Physical Chemistry B*, *104*(11), 2477-2489.

[109] Verlet, L. (1967). Computer" experiments" on classical fluids. I. Thermodynamical properties of Lennard-Jones molecules. *Physical review*, *159*(1), 98.

[110] Frenkel, D., & Smit, B. (2001). *Understanding molecular simulation: from algorithms to applications* (Vol. 1). Academic press.

[111] Brown, D., & Clarke, J. H. R. (1984). A comparison of constant energy, constant temperature and constant pressure ensembles in molecular dynamics simulations of atomic liquids. *Molecular Physics*, *51*(5), 1243-1252.

[112] Berendsen, H. J., Postma, J. P. M., van Gunsteren, W. F., DiNola, A. R. H. J., & Haak, J. R. (1984). Molecular dynamics with coupling to an external bath.*The Journal of chemical physics*, *81*(8), 3684-3690.

[113] Andersen, H. C. (2008). Molecular dynamics simulations at constant pressure and/or temperature. *The Journal of chemical physics*, *72*(4), 2384-2393.

[114] Nosé, S. (1984). A unified formulation of the constant temperature molecular dynamics methods. *The Journal of Chemical Physics*, *81*(1), 511-519.

[115] Martyna, G. J., Tobias, D. J., & Klein, M. L. (1994). Constant pressure molecular dynamics algorithms. *The Journal of Chemical Physics*, *101*(5), 4177-4189.

[116] Amereller, M., Schedlbauer, T., Moosbauer, D., Schreiner, C., Stock, C., Wudy, F. et al. (2014). Electrolytes for lithium and lithium ion batteries: From synthesis of novel

lithium borates and ionic liquids to development of novel measurement methods. *Progress in Solid State Chemistry*.

[117] Dahbi, M., Ghamouss, F., Tran-Van, F., Lemordant, D., & Anouti, M. (2011). Comparative study of EC/DMC LiTFSI and $LiPF_6$ electrolytes for electrochemical storage. *Journal of Power Sources*, *196*(22), 9743-9750.

[118] Von Sacken, U., & Zhong, Q. (1997). *U.S. Patent No. 5,650,245*. Washington, DC: U.S. Patent and Trademark Office.

[119] Saldivar-Guerra, E., & Vivaldo-Lima, E. (2013). *Handbook of Polymer Synthesis, Characterization, and Processing*. John Wiley & Sons.

[120] Fujikawa, S., Yano, T., & Watanabe, M. (2013). *Vapor-Liquid Interfaces, Bubbles and Droplets: Fundamentals and Applications*. Springer-Verlag Berlin An.

[121] Wu, M. S., Liao, T. L., Wang, Y. Y., & Wan, C. C. (2004). Assessment of the wettability of porous electrodes for lithium-ion batteries. *Journal of applied electrochemistry*, *34*(8), 797-805.

[122] Nairn, J. J., Forster, W. A., & van Leeuwen, R. M. (2011). Quantification of physical (roughness) and chemical (dielectric constant) leaf surface properties relevant to wettability and adhesion. *Pest management science*, *67*(12), 1562-1570.

[123] Aziz, S. B. (2013). Li^+ ion conduction mechanism in poly (ε-caprolactone)-based polymer electrolyte. *Iranian Polymer Journal*, *22*(12), 877-883.

[124] Kühnel, R. S., Obeidi, S., Lübke, M., Lex-Balducci, A., & Balducci, A. (2013). Evaluation of the wetting time of porous electrodes in electrolytic solutions containing ionic liquid. *Journal of Applied Electrochemistry*, *43*(7), 697-704.

[125] Naejus, R., Lemordant, D., Coudert, R., & Willmann, P. (1997). Excess thermodynamic properties of binary mixtures containing linear or cyclic carbonates as solvents at the temperatures 298.15 K and 315.15 K. *The Journal of Chemical Thermodynamics*, *29*(12), 1503-1515.

[126] Rulison, C. Effect of temperature on the surface energy of solids. *Kruss GmbH Newsletter11 (12/2005). http://www.kruss.de/en/home.html. Accessed 09 Sept2009.*

[127] Deng, J., Yang, Y., He, Y., Ouyang, G., & Huang, Z. (2006). Densities and surface tensions of trimethylbenzene + dimethyl carbonate or + diethyl carbonate at 298.15 K and 313.15 K. *Journal of Chemical & Engineering Data*, *51*(4), 1464-1468.

[128] Wang, F. K., Wu, J. T., & Liu, Z. G. (2004). Surface tension of dimethyl carbonate ($C_3H_6O_3$). *Fluid Phase Equilibria, 220*(1), 123-126.

[129] Zhao, G., Bi, S., Li, X., & Wu, J. (2010). Surface tension of diethyl carbonate, 1, 2-dimethoxyethane and diethyl adipate. *Fluid Phase Equilibria*, *295*(1), 46-49.

[130] Mosteiro, L., Casás, L. M., & Legido, J. L. (2009). Surface tension, density, and speed of sound for the ternary mixture {diethyl carbonate + p-xylene+ decane}. *The Journal of Chemical Thermodynamics*, *41*(5), 695-704.

[131] Nazri, G. A., & Pistoia, G. (Eds.). (2008). *Lithium batteries: science and technology*. Springer Science & Business.

[132] Lautrup, B. (2011). *Physics of continuous matter: Exotic and everyday phenomena in the macroscopic world*. CRC Press.